Master's thesis

NTNU
Norwegian University of Science and Technology
Faculty of Engineering
Department of Structural Engineering

Martin Fridheim Auestad

Radiation therapy and training effects on the mechanical performance of bone

Master's thesis in Mechanical Engineering
Supervisor: Bjørn Helge Skallerud
Co-supervisor: Astrid Kamilla Stunes
March 2021

NTNU
Norwegian University of
Science and Technology

Martin Fridheim Auestad

Radiation therapy and training effects on the mechanical performance of bone

Master's thesis in Mechanical Engineering
Supervisor: Bjørn Helge Skallerud
Co-supervisor: Astrid Kamilla Stunes
March 2021

Norwegian University of Science and Technology
Faculty of Engineering
Department of Structural Engineering

NTNU
Norwegian University of
Science and Technology

Abstract

As life expectancy steadily rises, new age-related challenges arise. Exposure to both osteoporotic fracture and cancer increases with age, and more cases are revealed as new technologies for medical examination are developed. Since bone loss has been related to cancer treatment, investigations on how this can be prevented are conducted. There is a general consensus that some forms of cancer therapy induce loss in bone mineral density and that physical training strengthens the skeleton. The question at hand is how cancer patients can perform exercises to attenuate the detrimental side effects of their treatment.

The aim of this three-part study has been to analyze some mechanical aspects of cortical bone physiology and how radiation and exercise affect certain bone qualities. Several studies have been conducted on skeletal response adaptation to loading. However, simultaneous introduction of ionizing radiation is little investigated. Further, finite element analysis as a tool for virtual testing of mechanical properties has been assessed.

In the first part, two separate experiments were conducted to measure rat femur response to radiation and training. An overall weaker mechanical performance was measured in radiated bone than in the control, but no significant differences were obtained. Radiated and trained femurs did also see some improvement over the radiated untrained specimens. However, the experiment results were inconclusive.

The second goal of the study was to virtually reproduce the physical bending tests conducted in the first part. Finite element models with specimen-specific geometry and density distribution were obtained by micro-CT imaging, and empirical relationships were employed to assign density-dependent intrinsic material properties. Correlation between experimental and virtual tests was assessed, and some critical challenges were unveiled. It was concluded that three-point bending test measurements are highly dependent on specimen aspect ratio, and that small elements are essential for accurate representation of inhomogeneous bone.

Finally, a scripted training/radiation model was presented. Muscle loads were defined from dynamics calculations and applied in static analyses. An adaptation model was employed to simulate bone evolution, and an expression for radiation damage was proposed. By comparison with the experimental setup in the first part, simulations yielded pleasing correlation, but further development is advised. The model can be considered as a preliminary proof of concept, which in future can help improve evaluations of patient-specific exercise treatment.

Sammendrag

Med stadig stigende forventet levealder oppstår nye aldersrelaterte utfordringer. Eksponering for både osteoporotiske brudd og kreft øker med alder, og flere tilfeller oppdages siden ny teknologi for medisinsk undersøkelse utvikles. Siden osteoporose har blitt relatert til kreftbehandling, utføres undersøkelser på hvordan dette kan bli forhindret. Det er generell enighet om at enkelte typer kreftbehandling forårsaker tap av beinmineral og at fysisk trening styrker skjelettet. Et spørsmål er hvordan kreftpasienter kan utføre fysisk trening for å lindre på skadelige bivirkninger fra deres behandling.

Målet for denne tredelte studien har vært å analysere noen mekaniske aspekter av kortikal bein og hvordan stråling og trening påvirker enkelte beinegenskaper. Flere studier har vært utført på skjelettets adaptasjon til belasting, men samtidig introduksjon av ioniserende stråling er lite forsket på. Videre har muligheten for mekanisk testing med elementmetode blitt undersøkt.

I første del ble to separate eksperimenter utført for å måle rottefemurs respons til stråling og trening. Det ble målt en generelt svakere mekanisk kvalitet i stålet bein enn i kontrollgruppen, men ingen signifikante forskjeller ble funnet. Stålet og trent bein så også noe forbedring fra stålet og ikke-trent bein. Likevel ble ingen konklusjon fastslått.

Det andre målet for studien var å virtuelt reprodusere de fysiske testene utført i første del. Elementmetodemodeller med spesifikk geometri og tetthetsfordeling ble hentet fra microCT-skanning, og empiriske modeller ble anvendt for å tilegne tetthetsavhengige materialegenskaper. Korrelasjon mellom eksperimentell og virtuell test ble evaluert, og enkelte kritiske utfordringer ble oppdaget. Det ble konkludert at målinger fra trepunkts bøyetesting er svært avhengig av størrelsesforholdet til prøven, og at elementer må være små nok til å presist representere inhomogent bein.

Til slutt ble en skriptet trening/stråling-modell presentert. Laster fra muskler ble definert fra dynamiske beregninger og påført i statiske analyser. En modell for adaptasjon ble anvendt, og et uttrykk for strålingsskade ble foreslått. Ved sammenligning med eksperimentell testprosedyre i første del viste simuleringene tilfredsstillende korrelasjon, men videre utvikling er anbefalt. Modellen kan ansees som en innledende konseptutprøving, som i fremtiden kan forbedre evaluering av pasientspesifikk treningsbehandling.

Acknowledgements

Although this thesis is being presented by a single author, a significant amount of people has played an important role to ensure its completion. I wish to express my gratitude to the contributors who have provided me with knowledge, insight, motivation and support. Without whom it would not have been possible for me to accomplish this study.

Special thanks to my supervisor Bjørn Skallerud at the Department of Structural Engineering, Faculty of Engineering, NTNU for presenting me with this intriguing field of study, that is biomechanics, and for the guidance and profound knowledge he has provided. His genuine interest in my project has provided me with crucial motivation whenever I have been in doubt, and his patience and willingness to discuss finite element theory with me on a Saturday evening is immensely appreciated.

I would also like to acknowledge my co-supervisor Astrid Kamilla Stunes at the Department of Clinical and Molecular Medicine and Comparative Medicine Core Facility, Faculty of Medicine and Health Sciences, NTNU for commencing her study on bone physiology in the first place. I have been introduced to a scientific subject far outside my general scope, and thanks to her I have learned so much more than I ever would have hoped for. Thank you for the many fruitful conversations, both academic and purely social, and for inviting me to partake in this spectacular research.

Thanks to Bernd Schmid, Tone Nilsen and Trond Auestad at the Department of Structural Engineering laboratories and to Ph.D. candidate Mohammad Javad Sadeghinia. I am grateful for their helpfulness and advising, ensuring high quality experimental testing and providing me with a solution to any question or need.

Finally, I wish to thank my family, my Ohana and my girlfriend whose encouragement and support throughout my studying proved indispensable. I would also like to express particular gratitude to my older brother Henrik Fridheim Auestad for providing me with a comfortable place to live and delicate meals and for putting up with me for the past one and a half years.

M.F.A

March 1, 2021

Preface

This thesis presents a Master's project within the study profile Computational Mechanics, course code TKT4915, at NTNU: Norwegian University of Science and Technology. The project was carried out during the fall semester of 2020.

My field of study is continuum mechanics and nonlinear materials. Thanks to the close relationship and collaboration between NTNU and the University Hospital of St. Olav, I have been given the opportunity to study the mechanical properties of bone. Computational mechanics is very much applicable to skeletal tissue, both because of its mechanical importance to body functions and because of its nonlinear material characteristics.

All the specimens used in this project are a part of a larger study addressing the possible link between exercise and reduced bone fracture risk caused by radiation therapy. Femurs and CT images were kindly provided by Kamilla Stunes.

The thesis at hand touches on several other topics of science, like anatomy, physiology, physics, dynamics, numerical methods and information technology. Although not strictly necessary, it is recommended for the reader to possess some knowledge of these topics, especially those related to medical science.

Despite my in-depth studying of skeletal tissue mechanics, it feels like I have barely scratched the surface of this immense matter. Truly, for everything new I have learned, I am realizing that there is still so much we do not know.

This fascinating and unforgettable study has offered immense insight to how structural engineering can be applied to the field of medical science and how an MSc in mechanical engineering can be used for the better of human health. I hope my work in some way can be beneficial to future studies.

Gløshaugen, Trondheim, Norway
March 1, 2021

Martin Fridheim Auestad

Table of contents

List of Figures

List of abbreviations

BMU basic multicellular unit
BMD bone mineral density
C3D10 10-node tetrahedron with quadratic interpolated displacement field
C3D4 4-node tetrahedron with linear interpolated displacement field
CTIBL cancer treatment-induced bone loss
CT computed tomography
DIC digital image correlation
DXA dual-energy X-ray absorptiometry
FE finite element
FEM finite element method
GV gray value
IDWI inverse distance weighting interpolation
µCT micro-computed tomography
PBS phosphate buffered saline
SED strain energy density
TPBT three-point bending test

1 | Introduction

1.1 Background and motivation

The skeleton facilitates movement and protection of soft organs. It transmits forces throughout the body and acts as a mechanical organ system. Bones are thus required to be strong and stiff to withstand the loads they are subjected to.

It is well known that physical exercises is a good way to build and maintain bone strength. Ever since the definition of Wolff's law was proposed, both presence and absence of physical stimulus has been shown to affect bone tissue over time through adaptation and remodeling (Frost 2004). On the other hand, cancer treatment-induced bone loss (CTIBL) can inflict detrimental damage to bone quality and remodeling efficiency, as described by D'Oronzo et al. (2015). With a stable rise in number of cancer and treatment cases every year (WHO 2020), and increasing chance of survival, it is in high interest of medical scientists to unveil exactly how cancer treatment affects bone adaptation and how this can be accounted for through patient specific treatment.

The development of micro-computed tomography (µCT) has allowed for detailed reconstruction of bone in 3D. Such digital models can further be transformed to a finite element (FE) mesh, where voxel density is accounted for. By mapping bone density values to intrinsic quantities, such as Young's modulus and yield stress, both the inhomogeneous material distribution and complex geometry of bone can be investigated from a purely mechanical point of view. Finite element method (FEM) can thereby facilitate non-intrusive, *in silico*, assessment of mechanical properties of tissue. Further, training stimulus and radiation deterioration can be simulated to investigate their respective and combined effects.

Some density-dependent material laws exist for healthy bone. Likewise, mathematical expressions for bone adaptation have been developed. The inclusion of a radiation damage model is however a little investigated field of study. When a new "variable" is introduced to a defined set of material laws, it is common practice to perform some form of experimental testing to validate the new model. Three-point bending test (TPBT) is often used to evaluate the aforementioned intrinsic material properties. Well-defined expressions for calculating such indices exist for isotropic materials with regular geometry. However, the complex material composition and irregular shape of femur present new challenges.

1.2 Problem description

The project at hand can be divided into multiple smaller problems. A brief description of what is investigated and the challenges met in the present study is presented below.

1.2.1 Experimental testing of cortical bone

Femurs from rats, which have undergone radiation, radiation and training or neither, are obtained. Each specimen is subjected to TPBT to measure various bone qualities. Global response properties are measured directly, and intrinsic indices are obtained through µCT image analysis. Results are compared between each group to investigate the impact of radiation and training. Further assessment is made to evaluate the feasibility of the mechanical testing method.

1.2.2 Virtual testing of cortical bone

Virtual representations of the femurs are obtained by µCT, where geometry and density properties are measured. These properties are mapped to intrinsic material properties with the use of statistically correlating expressions, established through empirical assessments. For implementation of virtual TPBT, specific loading conditions are defined to accurately represent real-life experimental bending tests. One corresponding model is made and virtually tested for every experimental specimen. Relevant simulation results are obtained and assessed to compare the virtual and experimental test results.

1.2.3 Simulation of training and radiation

A preliminary training/radiation simulation is created. Training is defined by generating a full FE femur model and a load case which resembles real-life anatomy. Muscle attachment points, load intensities and force directions must be defined as accurately as possible in for the training effects to apply with the right amount, and in the correct locations. Specimen-specific exercise schedules and intensities are recorded, and the training simulation can thus be tested with multiple load cases. Through the development of a well-fitting training simulation, an expression for bone adaptation can be developed. Additionally, radiation damage is simulated. A virtual representation of established knowledge on the behavior of radiated bone must be defined. This accounts for effects on both the soft, organic collagen and on the inorganic apatite mineral, which constitute the skeletal tissue. Different aspects of radiation-induced deterioration are examined, and the impact on bone adaptation effectiveness is discussed. An attempt is made to establish some fundamental knowledge on the combined simulation of training and radiation.

1.3 Research questions

The challenges described are confined to the following questions:

- **Question 1:** Can the effects of training and radiation on healthy bone be detected by TPBT? If so, what are the measurable changes?
- **Question 2:** By use of µCT and density to stiffness calculation, how can we recreate real-life bending test *in silico*?
- **Question 3:** How can exercise be simulated virtually, and is it possible to accurately apply an adaptation model to a µCT-obtained FE model?

1.4 Limitations

Trabecular bone structure will not be considered in this study. Although the trabecular region is more susceptible to radiation and training stimulus than the cortical region (Zhai et al. 2019; Westerlind et al. 1998), the mechanical testing method utilized does not facilitate accurate assessment of spongy bone. This poses some limitation to the overall experiment viability.

Some anisotropic bone properties are disregarded, namely those caused by specific organizing of material constituents at the histological level. For instance, Young's modulus, which is defined by an orthogonal manner, is considered to be isotropic. However, density distribution is considered as inhomogeneous, and tension/compression stiffness asymmetry is taken into account when defining density-dependent material laws.

When simulating training and radiation, the presence of mechanosensory cells, whose effect on FEM simulation of bone adaptation has been discussed by Weinans et al. (1992) and Ruimerman et al. (2003), is not considered. The absence of such cells might cause a checkerboard pattern (local stress shielding), where neighboring voxels obtain very different densities. This does not coincide with realistic remodeling of cortical bone. However, the resulting bone strength is tested in TPBT, where global qualities are assessed. Disregarding sensory cells is thus considered admissible.

1.5 Thesis outline

Chapter 2 – Theoretical background: Some relevant theory regarding rodent femur tissue anatomy and muscle anatomy is presented. This includes geometrical aspects, material composition, the physiology of remodeling and effects of radiation, and muscle attachments and activation during training. Additionally, preliminary knowledge on µCT scanning and reconstruction by use of FEM is presented.

Chapter 3 – Materials and methods: Procedures of both real and simulated experiments are described. This includes the *in vivo* comparative medicine animal study conducted by the Department of Clinical and Molecular Medicine and Comparative Medicine Core Facility, which dictates important simulation settings and result expectations. Voxel data acquirement procedure is also discussed, and some initial tests of convergence and error estimates are presented.

Chapter 4 – Results: Test results from the two experimental tests are presented. Global response values and intrinsic measurements are compared. Correlation of both global and intrinsic values between experimental and virtual bending tests are also put forward. Results are briefly discussed, and some questions concerning the outcomes are raised. Results from bone radiation/training simulation are presented.

Chapter 5 – Discussion: Implications of test results are discussed. Possible sources of error, regarding both the experimental and the virtual testing method, are analyzed more in depth. Testing quality and study validity is evaluated and suggested alterations and optimizations are presented.

Chapter 6 – Conclusion and further work: Some final thoughts regarding radiation therapy and training effects on the mechanical performance of bone, and a summary of the study. How can the findings in the present study be utilized to further investigate the subjects of interest? What can be done differently in future studies to ensure better test results and stronger correlations?

2 | Theoretical background

2.1 The femoral bone

Just like in humans, the rat femur connects the hip joint to the knee joint and transmits forces related to standing and gate. It consists of proximal and distal epiphyses, smooth and rounded surfaces which glide against articular cartilage; proximal and distal metaphyses, the rough regions where muscles and tendons are attached; and diaphysis, which is the long mid-section of the bone. There are some inherent differences between rodent and human femora due to the unlike two- and four-legged posture. These contrasts are expressed in muscular and geometrical characteristics, while material composition is considered to be similar in general. Although the femur is the bone mostly focused on throughout the respective thesis, much of the knowledge provided in the following sections applies to other bones as well.

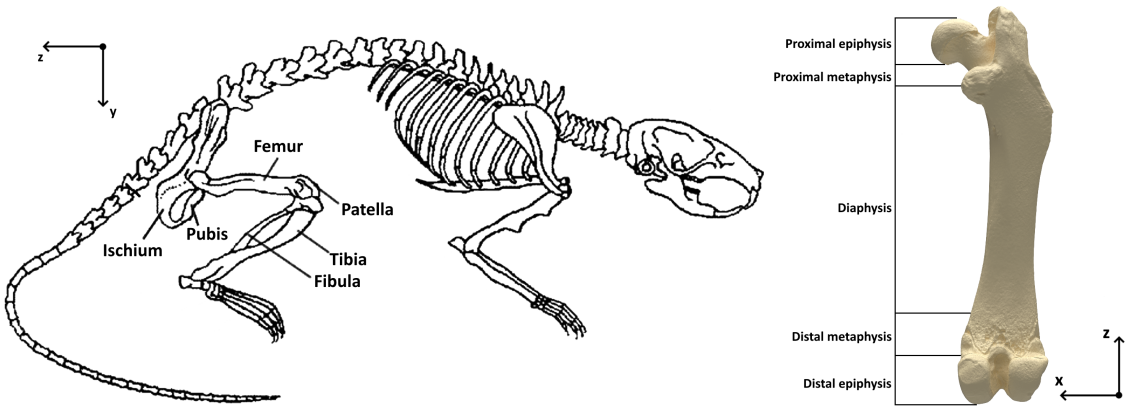

(a) (b)

Figure 2.1: Illustration of rat skeleton and femur: (a) anatomical location of right femur in rat. Axis cross is oriented with respect to local orientation of femur. Adapted from The Biology Corner (2021), (b) main sections of femur, seen in the coronal plane from the posterior towards the anterior region. The axis system depicted is the same system employed throughout the thesis: **z**-axis is longitudinal from distal towards proximal region of femur; **y**-axis is horizontal from anterior towards posterior; **x**-axis is horizontal from right towards left side (lateral towards medial region with respect to right femur).

2.1.1 Muscular anatomy

There are several muscles working together to perform leg extension and contraction. In addition, a full leg extension consists of both hip extension and knee extension. Due to the activation of several muscles, and their attachment points being located at different sites, the femur is consequently loaded in multiple directions during some form of movement. Figure 2.2 depicts the most important muscles related to hip and knee extension, and a list of muscles and their respective attachment points is presented in Table 2.1. Hip extensor muscles mainly originate at some region of the pelvis and insert onto either the proximal or the distal femoral metaphysis. Knee extensors, also known as the quadriceps group, originate at the proximal part of femur and inserts on the patella (kneecap).

In rodents and other four-legged mammals, ischium and pubis, the posteriormost parts of the pelvic bone, protrude further away from the hip joint than in humans (Fig. 2.1a). This causes a greater muscle moment arm of the hamstrings relative to the hip joint center coordinates. The hamstring muscle group (semimembranosus, semitendinosus and biceps femoris) perform both hip extension and knee flexion. However, due to the greater moment arms, these muscles play a larger role in hip extension in rodents than in humans, where the gluteus muscles are more predominant. Thus, during a jump, where the hip is extended, a rodent femur behaves more like a rod under compression than a cantilever, as in humans.

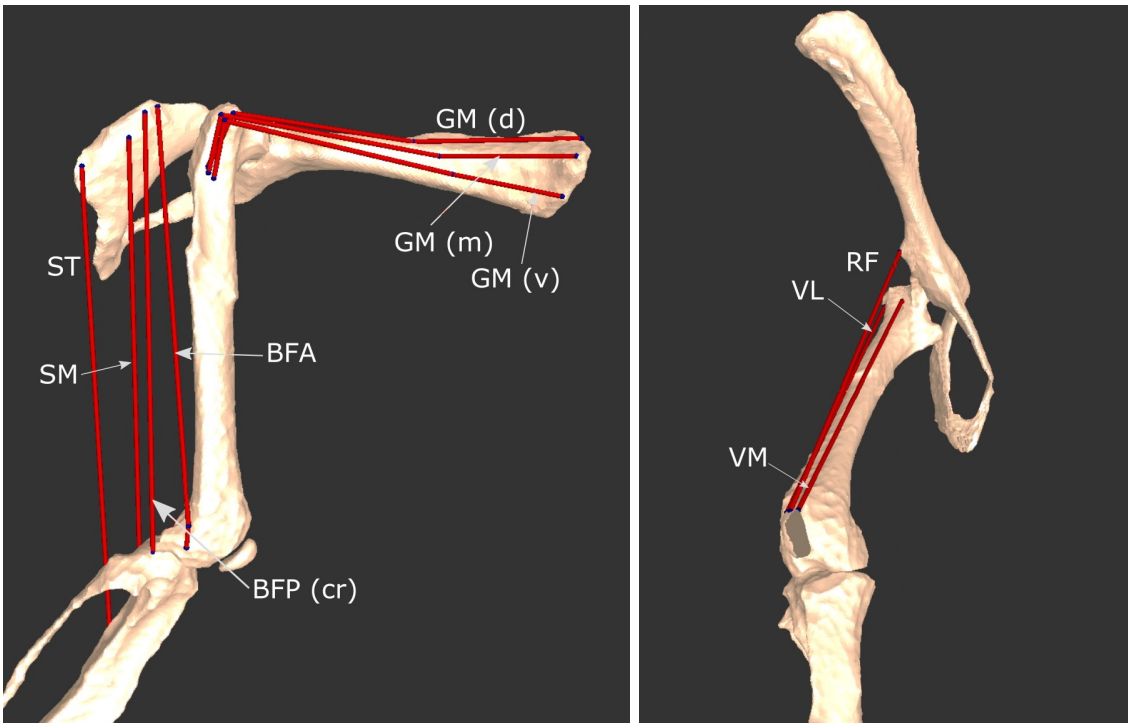

(a) Posterior **(b)** Anterior

Figure 2.2: Schematic illustration of right femoral muscle attachment points. Note that actual attachment points in general cover larger surfaces: (a) posterior muscles, mainly responsible for hip extension, (b) anterior muscles, mainly responsible for knee extension. Full muscle names are listed in Table 2.1. Adapted from Charles et al. (2016a).

Hip extensors	**Abbreviation**	**Origin point**	**Insertion point**
Gluteus maximus	GM (d,m,v)	Lateral aspect of iliac crest	Lateral aspect of proximal femur
Semimembranosus	SM	Mid facet of ischial tuberosity	Medial aspect of proximal tibia (proximal to gracilis)
Semitendinosus	ST	Caudal facet of ischial tuberosity	Medial aspect of proximal tibia (distal to gracilis)
Biceps femoris (anterior)	BFA	Cranial facet of ischial tuberosity (superficial to caudofemoralis)	Caudal-medial aspect of lateral femoral condyle
Biceps femoris (posterior)	BFP (cr)	Lower-mid facet of ischial tuberosity (superficial to semitendinosus)	Proximolateral aspect of the head of fibula and adjacent fascia
Caudofemoralis*	CA	Cranial facet of ischial tuberosity	Caudal-medial aspect of medial femoral condyle
Knee extensors	**Abbreviation**	**Origin**	**Insertion**
Rectus femoris	RF	Cranial inferior iliac spine of ilium	Base (proximal surface) of patella
Vastus medialis	VM	Medial aspect of proximal part of femur	Base (proximal surface) of patella
Vastus lateralis	VL	Lateral aspect of proximal part of femur	Base (proximal surface) of patella
Vastus intermedius*	VI	Cranial aspect of proximal part of femur	Base (proximal surface) of patella

Table 2.1: List of femoral muscles and their respective origin and insertion points. *Indicates no depiction in Figure 2.2. Adapted from Charles et al. (2016b).

A jumping sequence is a short and intensive action where both anterior and posterior leg muscles are tensed. Rats can initiate a jump from either a four- or two-legged stance, but in both cases, the quadriceps, hamstrings and glutes go from relaxed to contracted state. Figure 2.3 depicts a jump from two-legged standing. The height is 33 cm, and the jump itself lasts about one tenth of a second. If we assume maximum velocity at the moment when the hindlimbs leave the ground and zero velocity when landing at the top, we can approximate the acceleration during the jump:

(a) **(b)** **(c)**

Figure 2.3: Illustration of rat posture right before and during a jump: (a) standing before initiating the jump, (b) t_0, crouched position, right before performing the jump. Hip and knee joints are flexed and ready to extend, (c) t_1, jump is finished and hip and leg joints are fully extended. Slow motion video was captured with a OnePlus 5 mobile camera at 120 frames per second. The sequence from (b) to (c) was captured in 14 frames, resulting in a jump duration of 0.117 seconds.

$$a = \frac{\sqrt{2gh}}{t_1 - t_0} \tag{2.1}$$

Here, g is the gravitational acceleration, assumed to be 9.81 ms^{-2}, h is the jumping height, and $t_1 - t_0$ is the duration from jump initiation to the hindlimbs leaving the ground. The formula is a considerable simplification; a is assumed to be constant, the rat mass is considered as a singular point which travels the full jump height and the acceleration happens without the mass moving. Nevertheless, this calculation provides a good assumption of what forces are exerted on the femur. Further, if one assumes the jump to be perfectly vertical, all forces acting on the mass center to be expressed as one vertical force and the gravitational acceleration to be positive definite, the net force can be expressed:

$$\sum F = m(a + g) \tag{2.2}$$

where m is the rat mass expressed as a singular point. By combining Equations (2.1) and (2.2), one can express individual load cases for each rat femur with force intensities dependent on the rat weight and jump height. Additionally, forces must be divided to represent the respective muscle groups. This process is described in Section 3.4.

2.1.2 Femur geometry

Most forces related to a jump are directed axially through the femur, exerting compressive stress. However, due to its geometry and the position of muscle attachment points, the bone is also susceptible to other stresses, like bending, shear and torsion. Further, bending can occur about any axis parallel to the transverse plane, requiring the femur to be strong in multiple directions. Equations (2.3a) and (2.3b) describe the 2nd moment of area of a beam and the axial stress, $\sigma_{\mathbf{z}}$ in in that beam when subjected to a moment, $M_{\mathbf{x}'}$, respectively. In a case where the flexural axis varies in any direction orthogonal to the **z**-axis, Equation (2.3a) dictates that the optimal cross section of a beam bound by a maximum area is the portion bounded by two circles, which is a hollow cylinder.

$$I_{\mathbf{x}'} = \iint_A y'^2 dA \tag{2.3a}$$

$$\sigma_{\mathbf{z}} = \frac{M_{\mathbf{x}'}}{I_{\mathbf{x}'}} \cdot y' \tag{2.3b}$$

Here, the **x'y'**-plane denotes an arbitrary plane with normal vector parallel to the **z**-axis. Shear stress induced by torsion is calculated similarly as bending stress, only dependent on the second polar moment of area, J, instead of I:

$$J_{\mathbf{z}} = \iint_A r^2 dA \tag{2.4a}$$

$$\tau = \frac{T_{\mathbf{z}}}{J_{\mathbf{z}}} \cdot r \tag{2.4b}$$

Torsion shear stress occurs orthogonal to any radial axis, **r**, from the center of mass and increases outwards. If one considers the cross section of a beam under bending and torsion load to be that of a thick-walled hollow cylinder, Equations (2.3a) and (2.4a) are expressed by Equations (2.5a) and (2.6a), respectively, where R and r denote the outer and inner diameter. By further imposing a constant cross section area, A, one can express the maximum bending and torsion stresses (Eqs. (2.5b) and (2.6b)).

$$I_{\mathbf{x}'} = \frac{\pi}{4}(R^4 - r^4) \tag{2.5a}$$

$$\sigma_{\mathbf{z},max} = \frac{2M_{\mathbf{x}'}}{AR^2 - \frac{A^2}{2\pi}} \cdot R \tag{2.5b}$$

$$J_{\mathbf{z}} = \frac{\pi}{2}(R^4 - r^4) \tag{2.6a}$$

$$\tau_{max} = \frac{T_{\mathbf{z}}}{AR^2 - \frac{A^2}{2\pi}} \cdot R \tag{2.6b}$$

It can be deduced from Equations (2.5b) and (2.6b) that given a finite bending and torsion moment:

$$\lim_{R\to\infty} \sigma_{\mathbf{z},max}(R) = \lim_{R\to\infty} \tau_{max}(R) = 0$$

and thus, for a finite cylindrical area, the exerted stresses from bending and torsion are minimized by maximizing the wall radius. Likewise, if one still assumes the cross section to be cylindrical, Equation (2.7) describes the nominal shear stress. The function behaves in a similar manner as it goes to zero when R and r go towards infinity.

$$\tau_{max} = \frac{4V_{\mathbf{x}}'}{3\pi}\left(\frac{R^2 + Rr + r^2}{R^4 - r^4}\right) \tag{2.7}$$

Images of all rat femur cross sections are shown in Appendix A. They can to some degree resemble a thick-walled cylinder, and from a purely mechanical point of view, the femur is nearly optimally designed for the aforementioned types of load. It is a note of interest that rat femur is generally more oval-shaped than human. This might be caused by the inherent difference in stance and gate and overall movement. Another important property of the femur, which will affect the project procedure to a certain extent, is the aspect ratio of the shaft, or shaft length divided by the cross section diameter perpendicular to the flexural axis. while the aspect ratio of human femur is ∼13, the same ratio was measured to ∼8 for the rats utilized in this project. Although a low aspect ratio might be beneficial from an evolutionary perspective, it does introduce some challenges when conducting a three-point bending test.

2.1.3 Bone material

Skeletal tissue material comes in various forms and arrangements, depending on the bone and its duties. Long bones, like the femur, are structurally different at different regions. The proximal and distal epiphyses and metaphyses consist of an inhomogeneous, honeycomb-like network of small bones, called trabeculae. The porous trabecular bone provides multiaxial strength while maintaining a low apparent density. At the transition between the metaphyses and diaphysis, the bone congregates at the perimeter as dense, cortical bone (Fig. 2.4).

The material properties of cortical bone are inherently different from trabecular bone due to the unlike structure. However, this bone is also inhomogeneous because bone itself is a composite material. Its main constituents are organic matrix (∼30 % of weight, ∼35 % of volume), predominantly type I collagen, and inorganic apatite mineral (∼60 % of weight, ∼40 % of volume), and the remainder is water. The organic phase is soft and ductile. It contributes to the maximum strain before failure and to toughness, which governs energy absorption before rupture and resistance to crack propagation. The mineral phase is hard and rigid. It maintains the physical structure and is central to the Young's modulus of bone. However, apatite mineral

is also brittle, much like concrete, meaning it will fail more easily under tension than compression. The interaction between organic and inorganic phases causes a tension/compression asymmetry, where compressive yield stress is nearly double that of tensile (Morgan et al. 2013, p. 1–17). Consequently, the force-displacement curve from a TPBT will have nonlinear characteristics.

At the histological level, or the microscale, of cortical bone, mineralized collagen fibrils (fibers of alternating collagen molecules and mineral crystals) are organized in lamellar sheets. The fibre orientation is uniform within each lamella but varies between each sheet. This dense plywood structure is strongest in the average direction of all fibrils, which is close to the longitudinal axis for any long bone. The lamellar pattern is mostly concentric, either about vascular channels or about the entire diaphysis, presenting an orthogonal material behavior (Jee 2001, p. 1–5). This makes the femur much weaker in transverse compression than in axial compression.

Despite the very anisotropic material behavior of bone, some intrinsic properties have been deducted through multiple experiments. The data listed in Table 2.2, collected by Karim, Hussein, et al. (2013), are the most relevant properties for the work presented in this thesis. These properties vary greatly between different animal species, individual subjects, different bones and locations within each bone. Thus, the presented measurements cannot be considered as absolute values, but rather as adequate indicators which can be compared to when evaluating test results. The following subsections describe how some intrinsic material properties of bone are affected by external factors as well.

(a) Proximal region **(b)** Distal region

Figure 2.4: µCT pictures of rat femur, cut along the coronal plane, illustrating the trabecular and cortical sections.

Mechanical property		Range	Description
Young's modulus, E	GPa	10.7–14.8	Bending
		18.2	Compression, longitudinal
		11.7	Compression, transverse
		17.9	Tension, longitudinal
		10.1	Tension, transverse
Yield strain, ε_y	%	0.73	Tension (no further description)
Yield stress, σ_y	MPa	191–227	Bending
		182	Compression, longitudinal
		121	Compression, transverse
		107.9–115	Tension (no further description)
Ultimate strain, ε_u	%	2.20	Compression, longitudinal
		4.62	Compression, transverse
		2.93–3.1	Tension, longitudinal
		3.24	Tension, transverse
Ultimate stress, σ_u	MPa	208.6–281	Bending
		195–205	Compression, longitudinal
		131–133	Compression, transverse
		133–135	Tension, longitudinal
		51–53	Tension, transverse
Fracture toughness, K	$\mathrm{MPa}\sqrt{\mathrm{m}}$	4.28–5.09	

Table 2.2: Mechanical properties of cortical bone measured in human femur. Adapted from Karim, Hussein, et al. (2013).

2.1.4 Remodeling and adaptation

After fully developing to its adult length and shape, bone still reshapes and changes continuously to maintain a healthy skeleton. This episodic, repetitive process of microscopic damage repair and fatigue prevention is called remodeling, in which basic multicellular units (BMUs) perform resorption (removal) and absorption (adding) of tissue. It begins with osteoclasts removing both organic and mineral phases from a site, followed by osteoblasts which form osteoid. Osteoid functions as a scaffold for apatite mineral to crystallize in. When a BMU cycle is completed, a new vascular channel (osteon) is formed in cortical bone. Since the BMU diameter of ∼200 µm is larger than an individual trabecula, which is 100–150 µm, only hemi-osteons are formed in the spongy regions. A complete remodeling sequence in humans takes between four and six months (much shorter time in rodents), and formation takes considerably longer time than resorption. Age-related imbalance in the remodeling procedure, such that it leans heavier towards resorption, is thought to be the cause of some osteoporotic fractures (Martin et al. 2015, p. 49, 97–107).

Adaptation is a subdivision of remodeling which is thought to facilitate an optimization of bone's mechanical efficiency. After the formation of osteoid and initiation of mineralization, some osteoblasts transform into osteocytes within the secreted matrix. These are mechanosensory cells which regulate further absorption and resorption at their specific location. By transducing mechanical stress and strain signals into biochemical signals, they interpret whether a higher or lower bone mineral den-

sity (BMD) is needed to withstand the local loading. The Mechanostat is a collective term which describes the physiological reaction to mechanical stimuli. According to this term, adaptation works in a control loop, which maintains equilibrium state between bone material strength and the mechanical loads exerted on it. Bone adaptation is generally considered as a mechanism which increases mineral accumulation due to training. For instance, heavy weightlifting leads to stronger bones. However, since a high BMD at a location subjected to little load is an inefficient distribution of mass and energy, adaptation also promotes tissue removal where needed. This was demonstrated by Vico et al. (2000), who research the effects of microgravity on BMD loss in cosmonauts. Likewise, bedridden patients and elderly people are susceptible to negative adaptation due to reduced mobility (Eimori et al. 2016).

From a literature study by Auestad (2020), it was found that bone adaptation is highly sensitive to loading continuity. Although it may take months for a human bone to initialize adaptive formation, resorption occurs more promptly. This correlates to, and might in part be because of, the different duration of formation and resorption in the BMU cycle. Further, after a long time of stimulus through exercising, the degree of formation seems to lessen, suggesting that training intensity might not be as important to formation as simply training at all. It was further found that weighted resistance training is more effective than aerobic. However, since weightlifting movements tend to be isometric and unidirectional, optimal formation might be inhibited. As the femur is shaped to withstand loading in different directions, it also needs to be loaded in different directions to fully develop. An example of this was shown by Nilsson et al. (2013), who discovered greater femoral and tibial bone qualities in soccer players than in resistance training subjects.

It must be noted the difference in time aspects of physiological events between human beings and rats. A rat's lifespan is two to four years, and the duration of different physiological events are much shorter. Thus, adaptive bone formation can be observed in laboratory rats in just a few weeks. When Mosti et al. (2016) studied the musculoskeletal effects of exercise in ovariectomized rats, increased BMD was observed after eight weeks of plyometric jumping exercise.

2.1.5 Radiation

Although radiation therapy is much used in cancer treatment, it has been shown to have detrimental consequences on muscular and musculoskeletal quality. High energy irradiation can alter the cell DNA, causing cell death and cancer treatment-induced bone loss (CTIBL). The most adverse effects occur early after subjection to radiation, as the collagen phase is diminishing. This leads to porous and brittle bone which is more susceptible to fracture. In the long run, irradiation can result in loss in trabecular number and thinning of both trabecular and cortical bone due to reduced osteoblast proliferation. This causes an imbalance to the remodeling homeostasis so that the rate of resorption is higher than that of formation. Exposure to ionizing radiation also affects adaptation efficiency. In addition to causing osteocyte apoptosis, since osteocytes descend from osteoblasts, reduced osteoblast proliferation might lead to a reduction of these mechanosensory cells.

2.2 µCT to FEM

2.2.1 Scanning

What differentiates computed tomography (CT) from conventional X-ray and dual-energy X-ray absorptiometry (DXA) is the ability to render a three-dimensional visualization of the scanned body. This provides invaluable information during medical assessments; disease diagnosis and planning of surgical procedures becomes easier and more accurate. CT works by rotating either the X-ray source and detector around the body or the body itself. After a half-circle rotation is completed, the source and detector system is moved incrementally along the longitudinal body axis and the rotation sequence is repeated. The different setup of conventional X-ray and CT scanning is illustrated in Figure 2.5. An algorithm is applied to the set of CT-images to output views in different planes or a full 3D-rendering.

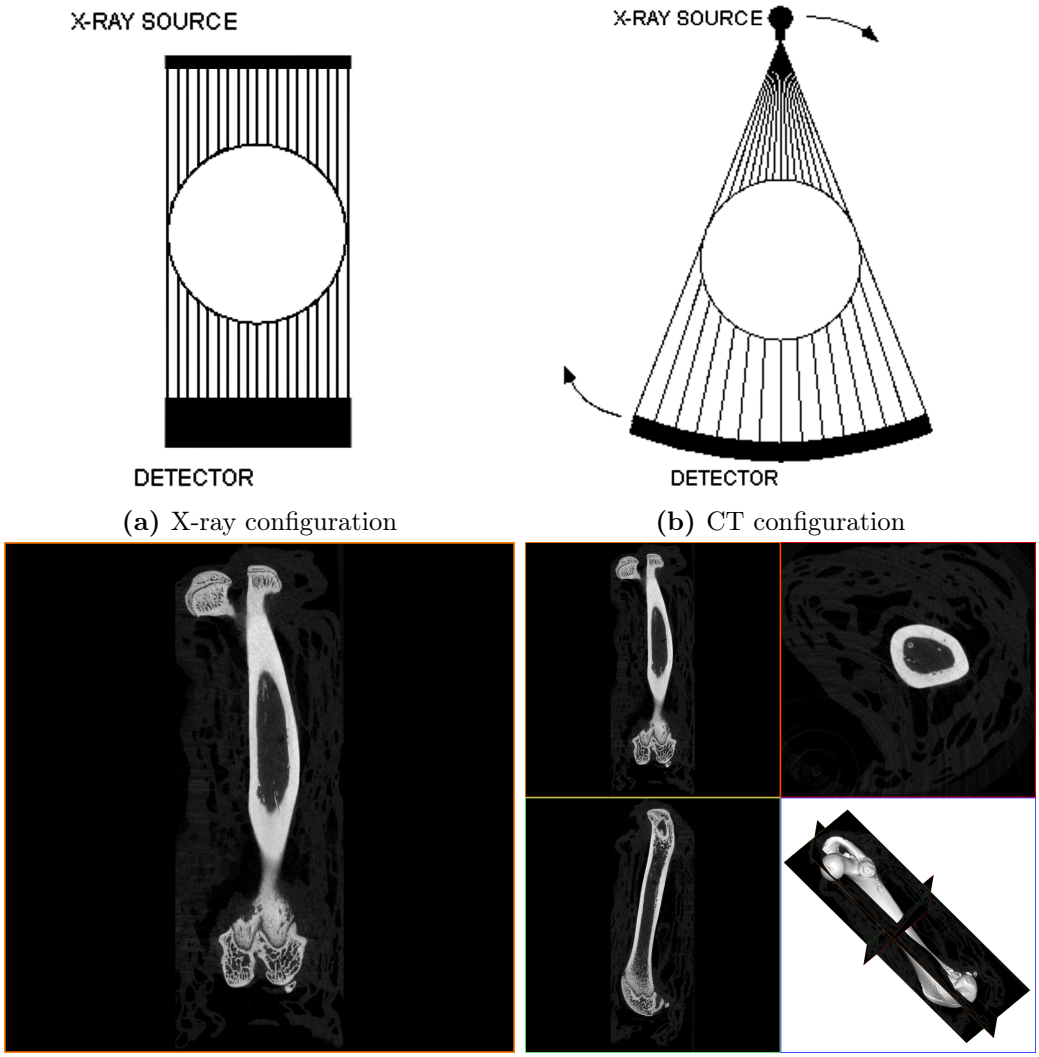

(a) X-ray configuration

(b) CT configuration

(c) X-ray output

(d) CT output

Figure 2.5: Illustrations of X-ray and CT setups and resulting outputs. (a) and (b) are adapted from University of Texas (2020). X-ray path is downwards along the straight lines.

Due to the different density and water content, and thereby the mass attenuation coefficient, of different organs, it is possible to distinguish them from one another. For instance, in a negative 12-bit grayscale image, ranging from 0 (black) to 4095 gray value (GV) (white), bony tissue, which has a low attenuation coefficient, is presented with light intensity from ∼1300 GV and up. Soft organs are displayed as much darker since more of the electromagnetic radiation passes through. If, however, the scan resolution is high enough, like in µCT, even individual trabeculae and voids in the cortical bone can be observed (Fig. 2.4). Consequently, µCT allows for detailed investigation of apparent bone density distribution.

While the high irradiation exposure from µCT makes it inapplicable to clinical procedures, it can be used in *ex vivo* and rodent studies. In some cases, µCT is even used to simulate radiation therapy treatment (Mustafy et al. 2018).

2.2.2 Meshing

3D-rendering of body organs is most commonly used for visualization and not for assessment of material properties. Therefore, many software utilities, both professional and freeware, provide the ability to render a surface mesh which can be exported for 3D printing. However, creating a volumetric mesh is algorithmically a much more demanding task for which a solution is not commonly offered. Additionally, in order to obtain voxel-specific densities, the CT-image grayscale values must be related to each respective voxel. This requires the entire transformation from image sequence to mesh file to be performed in one sequential job.

When deciding on volume mesh type and size, accuracy and compute cost needs to be taken into account. While it is desired to precisely represent the small details of osteons and trabecula (see subsection 2.1.4), a uniform mesh with maximum edge length of only a few µm will cost an overwhelming amount of computing power to work with. It is therefore necessary to determine a meshing solution with feasible accuracy which is still manageable with the computing power available.

In general, a quadratic or higher order cubic mesh element is considered to better handle large displacements than a triangular element in FE analysis. If the same accuracy is desired for tetrahedrons, the element edge length and volume need to be reduced, thus increasing the number of elements. On the other hand, tetrahedrons are preferable when modeling complex geometries. Additionally, a smaller element volume means that each bone voxel density is better represented, suggesting that tetrahedral elements might be preferable over hexahedral elements when modeling bone. A visualization of the argument made is seen in Figure 2.6. It is shown that if a hexahedral and a tetrahedral mesh were set to represent the same amount µCT pixels per finite element, the hexahedral element edge length would have to be smaller than the tetrahedral element edge length.

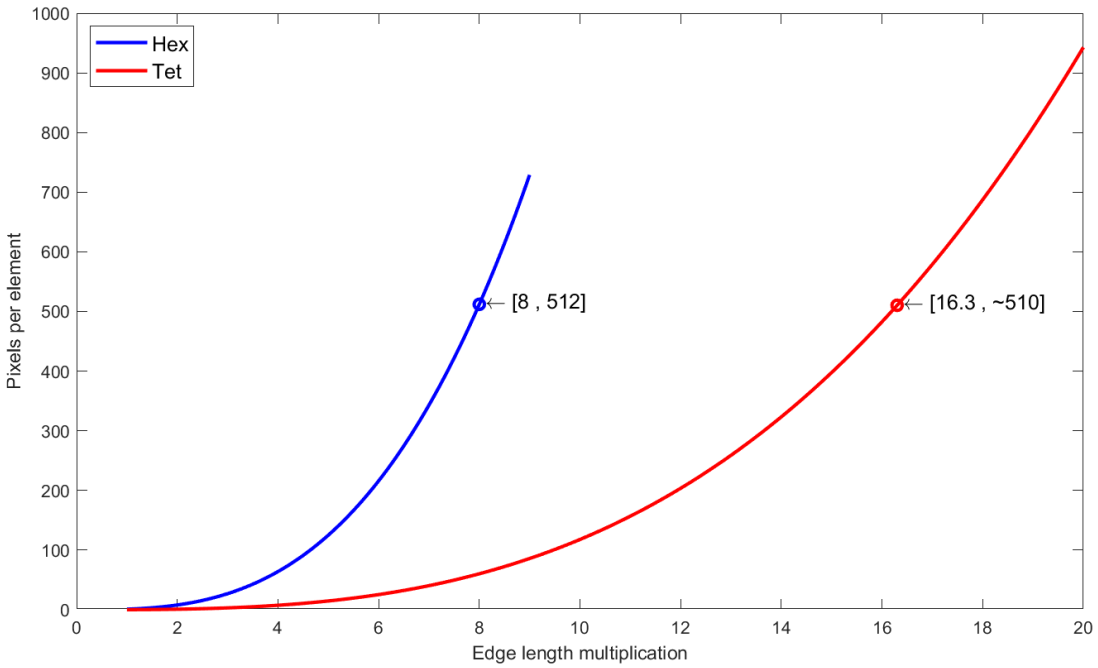

Figure 2.6: An equal edge length of a tetrahedral and hexahedral element results in smaller tetrahedral element volume and, thereby, higher accuracy. The illustration considers an equilateral pixel volume from CT scan and equilateral hexahedral and tetrahedral elements.

3 | Materials and methods

3.1 Rat radiation and training

Two individual *in vivo* animal studies were conducted at St. Olav's Hospital (Trondheim, Norway) by the Department of Clinical and Molecular Medicine and Comparative Medicine Core Facility (NTNU). In the first study, 24 female Sprague Dawley rats (12 weeks of age, 282 ± 11 g) were housed in wire-top cages with woodchip bedding, 4 animals per cage. The rats followed a 12-hour day-night cycle, in room temperature at 24 ± 1°C and relative humidity at 40–50 %. After approximately one week of acclimatization, 12 rats (Rad-1) were subjected to one single dose of 6 Gy whole body radiation under anesthesia, using a linear accelerator which creates high energy photon radiation (high energy X-rays). The other group (Ctrl) was not radiated. Euthanasia was conducted 2, and 4 and 9 weeks after radiation, 4 radiated rats and 4 controls at each point of time.

In the second study, 24 rats of same species, (12 weeks of age, 300 ± 15 g) were housed under same conditions. All rats were radiated approximately one week after acclimatization, as described above. Two weeks after radiation, 12 rats in the exercise group (RadEx) started high intensity jump training, following the same program as described by Mosti et al. (2016). The program lasted for 6 weeks, with 3 sessions each week, except 2 sessions the third week and one session the final week, for a total of 15 training sessions. Each session consisted of 3 sets of 6 jumps, with 2–3 minutes of rest between each set, for a total of 18 jumps per session. Jumping height was set to 20 cm for the first session, 24 cm for the two following session and 28 cm at the fourth session, unless the rat was unable to jump this high. For the following sessions, the jumping height was individually adjusted to each rat's capacity to emphasize progressive jumping height throughout the training period. The maximum successive height during a session was logged for each rat. Rat weight was logged each week. Euthanasia was conducted on all animals 8 weeks after radiation, 48 hours after the last exercise session for the animals in the exercise group.

The rats from the first and second studies were labeled with number 1–24 and 25–48, respectively. µCT scanning procedure is described in the following section.

3.2 Voxel data acquirement

3.2.1 µCT scanning

For both the studies conducted at NTNU and St. Olav's Hospital, right femur was obtained from all rats after euthanasia for µCT scan. Femurs were snap frozen in liquid nitrogen and stored at -80 °C until analysis. Before µCT scanning, the femurs were thawed in room temperature and wrapped in paper with phosphate buffered saline (PBS) solution to avoid dehydration and placed in a plastic tube. Femurs were scanned at 18 µm isotropic resolution with a SkyScan1172 µCT imaging system (Skyscan, Kontich, Belgium). Source voltage and current were set to 65 kV and 385 µA, respectively, and a 0.5 mm aluminum filter was used to optimize contrast. X-ray source was rotated in steps of 0.5°, and raw images were reconstructed to 3D cross-sectional data using NRecon software (SkyScan). For reconstruction, beam hardening, smoothing and ring artifact reduction were set to 31 %, 3 and 4, respectively. The reconstructed images were exported as 16-bit TIFF images for finest possible GV level increments. After scanning, the femurs were stored at -80°C until they were transported to the bending test facility. Here, the samples were stored in a household freezer for a maximum of 4 days before testing.

3.2.2 Mimics

All reconstructed µCT image sequences were processed and converted into FE models using Mimics 23.0 (Materialise NV, Leuven, Belgium). Although the actual scanned voxel size was 17.66348 µm per pixel, restrictions to decimal places in Mimics required a rounding to 0.0177 mm. A 0.2 % size increase was however considered acceptable. The color depth was mapped from 16-bit to 12-bit to reduce the amount of data. Additionally, this allowed for utilization of the predefined density threshold values in Mimics when masking the segments of interest. 12-bit GV levels of bone is described in subsection 2.2.1.

Segmentation of the femur was conducted by applying a global mask with minimum GV threshold of 1300 with automatic filling of all small voids. A second mask was applied to fill the entire femoral cavity. Open holes, due to the presence of some vessels passing into the femur, were marked and sealed to make the segment watertight. A new mask with maximum GV threshold of 1249 was then created and adjusted to mark the diaphyseal inside. This mask was bounded by the proximal and distal metaphyseal sections so that only the medullary cavity volume was covered. By performing a Boolean operation, in which the cavity mask is subtracted from the femoral mask, one is left with a hollow femur with a smooth inside surface. This reduces the total number of elements and computation time. It also reduces the amount of cavity surface irregularities caused by trabecular bone. This minimizes the possibility for ill-defined elements when creating a uniform volumetric mesh. The porous bone regions at the endosteum were considered to be insignificant to the bone strength.

The segmented models intended for virtual TPBT were cut so that the proximal and distal heads were removed, which further reduced the number of elements. Images of each specimen, taken during experimental TPBT, were utilized to decide where the model should be cut. Cutting planes were set at 1 mm distance from where the femur was contacting the bending test supports (see section 3.3), resulting in a total model length of 14 mm.

A standard tessellation language part file was created and smoothed to remove some remaining irregularities in Mimics. The part was then copied to 3-matic (Materialise NV) to perform FE meshing. The decision made on element size is described in subsection 3.2.4. A uniform meshing algorithm was applied, and potential noisy or overlapping shells were removed. Before creating a volumetric mesh, node- and element sets were defined for where different boundary conditions should be applied in the virtual TPBT (see subsection 3.3.3). This was done manually, by positioning the model along an inbuilt ruler and marking out the respective surface elements (Fig. 3.1). The marked distal and proximal posterior surface elements are where the femur is supported, and the anterior surface elements are where the plunger comes in contact with the specimen. By this method, only periosteum nodes, and no nodes inside the mesh, would be selected for boundary conditions. It was ensured that the contact surface regions were uniformly one element wide to replicate the sharp-edged contact points on the bending test machine. After creating a volumetric mesh, an Abaqus input file with quadratic elements and specific node sets was exported from 3-matic, and the FE mesh was copied back to Mimics.

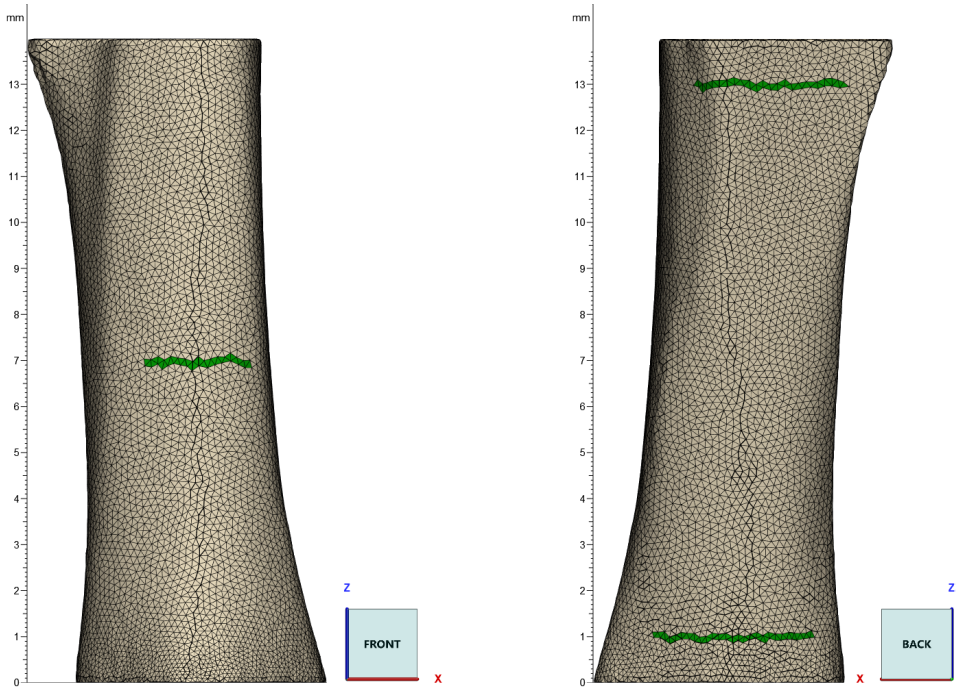

(a) **(b)**

Figure 3.1: Example of boundary surfaces in 3-matic: (a) anterior (front) surface, where the plunger is applied, (b) posterior (back) surface, where the specimen lies on two support. Note that the model is 14 mm long, support surfaces are 12 mm apart and the plunger surface is in the middle of the model. All boundary surfaces were made short enough to only cover a flat anteriormost and posteriormost region.

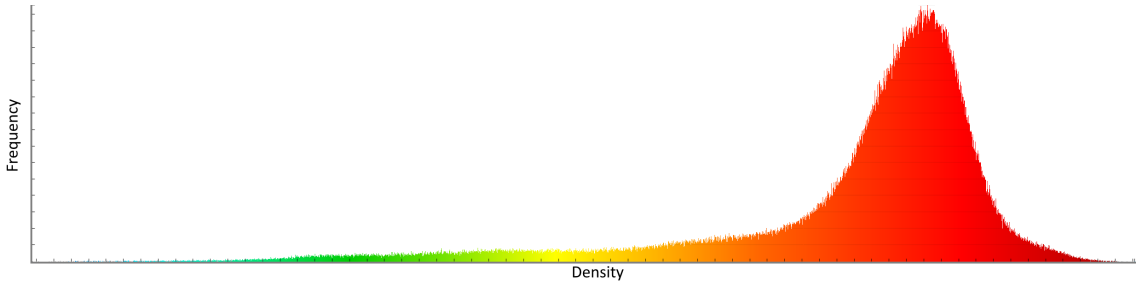

Figure 3.2: Example density distribution plot from Mimics after assigning linear GV and apparent density relationship.

Back in Mimics, a gray value and apparent density relationship was defined. A linear relationship was considered (Ramezanzadehkoldeh and Skallerud 2017a), adjusted for 12-bit depth GV levels, deriving the expression $\rho = 4.395 \times 10^{-4}$ GV (g/cm^3). To maintain a low level of granularity in density levels, the scale from zero to maximum density was divided into 1000 steps. Figure 3.2 depicts the density distribution of femur 1. Since only a section of cortical bone was modeled, very few elements with density below typical apparent density of cortical bone are represented.

Two Ansys Preprocessor files containing element densities and element to node relationships were exported from Mimics. Since Abaqus, the simulation software utilized in this study (see subsection 3.3.3), assigns field variables to nodes, and not to elements, a conversion script was created in MATLAB (MathWorks, Natick, Massachusetts, USA), to assign the element densities to nearby nodes instead. The script would also sort out the elements related to the boundary surfaces (see Appendix G).

3.2.3 Inverse distance weighting interpolation

In order to retain an as accurate density distribution as possible during conversion, is was considered infeasible to calculate the node density since the average of its related elements, as local information would be lost. Instead, an inverse distance weighting interpolation (IDWI) formula was employed (Eq. (3.1)). This formula works by weighting the average density of all element connected to a node with the inverse of the distance between each element and the node:

$$\rho_n = \frac{\sum_{i=1}^{NoE} \left(\frac{\rho_i}{d_i^p} \right)}{\sum_{i=1}^{NoE} \left(\frac{1}{d_i^p} \right)} \tag{3.1}$$

Here, NoE is the number of elements related to a node and ρ_n is the calculated node density. ρ_i^p is the apparent density of each element raised to the power of a weighting number, p. If p is set to 0, the formula expresses the mean of all element densities, and as p increases, the weights for distant elements decrease. Figure 3.3 depicts the IDWI nodal density distribution of femur 1, calculated with $p = 1$ and $p = 2$ versus Mimics element densities.

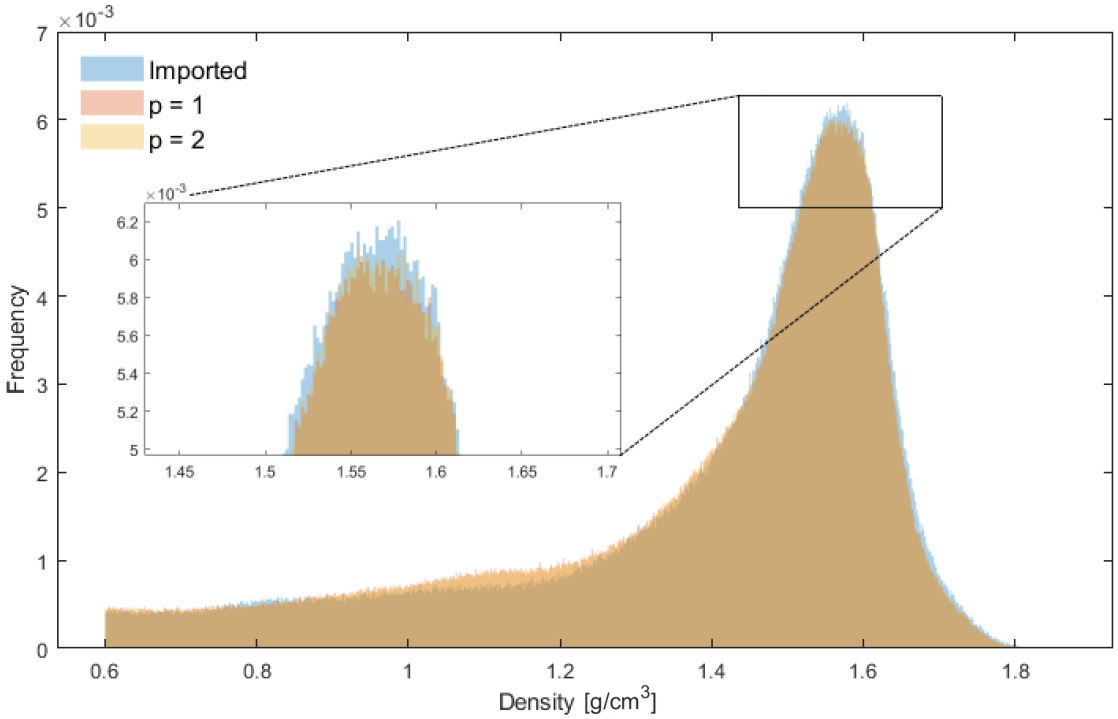

Figure 3.3: Mimics element densities (Imported) versus IDWI with $p = 1$ and $p = 2$. Frequency is the percentage share of all elements. Element type: C3D10.

Although $p = 2$ seems to yield better correlation with Mimics than $p = 1$, there is still some information lost. Figure 3.4 shows a distribution plot with $p = 40$.

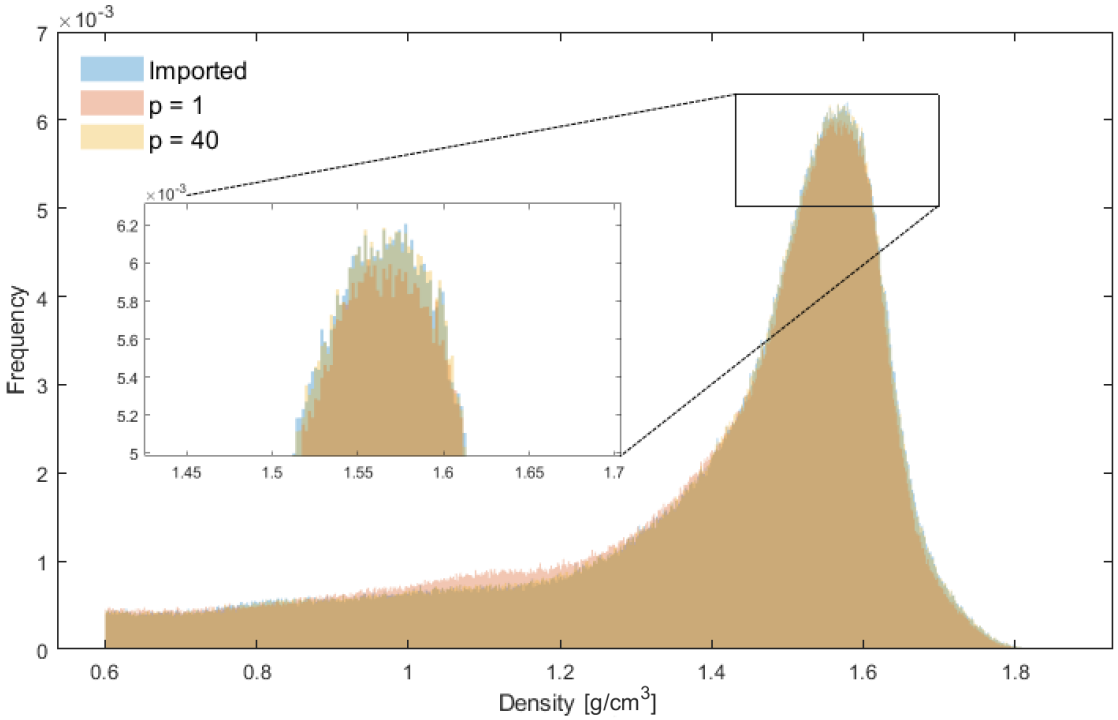

Figure 3.4: Mimics element densities (Imported) versus IDWI with $p = 1$ and $p = 40$.

When the p value is this high, generally only the immediate surrounding elements will influence the predicted density. Yet, the predicted nodal density is not equal to the single nearest element, which would have caused all nodes related to one small element to be of equal density. Because of how IDWI works, it was nevertheless necessary for the mesh elements to be as uniform in size as possible for the nodal density prediction to work optimally.

3.2.4 Defining element properties

Since Materialise 3-matic is only able to produce tetrahedral volume elements, this method was employed. In general, hexahedra are preferred over tetrahedra since they are more economic, with respect number of elements for an equal number of nodes, and because of their higher per-element accuracy. On the other hand, tetrahedra are better for fitting complex geometries.

Another important note, which originates from the Mimics element-to-node density conversion explained in the previous subsection, is the amount of elements which are connected to each node when performing IDWI. A higher number of elements related to each node will increase the likelihood for each local density to be accurately represented. If one considers a group of non-surface quadratic elements, a tetrahedral midpoint node will be connected to at least five elements, while a corner node is connected to twenty elements or more. Due to the geometric nature of a tetrahedron, a completely uniform mesh of equilateral elements is unobtainable, and nodes might therefore be connected to even more elements (the largest number obtained from 3-matic was 42 elements). For an equivalently defined hexahedron, corner and midpoint nodes are connected to exactly eight and four elements, respectively.

In order to keep a feasible number of element, a voxel reduction, which means increasing the element edge length to a value higher than the initial pixel size of 0.0177 mm, was applied. Ramezanzadehkoldeh and Skallerud (2017a) found an $8 \times 8 \times 8$ reduction of hexahedral elements, resulting in about 6×10^5 elements with 40 µm edge length, to be acceptable. There are however two important differences between their study and this one; mice have much smaller femurs than rats. The same element edge length in a rat femur would consequently generate a model with several million elements. Second, since the volume of a hexahedron is $6\sqrt{2}$ times larger than a tetrahedron with the same edge length, an equivalent model of the latter element type would consist of $\sim$8.5 as many elements.

Figure 2.6 shows how many voxels that are represented by hexahedral and tetrahedral elements for an arbitrary voxel volume as reduction magnitude is increased. It suggests that for an $8 \times 8 \times 8$ reduction of hexahedral elements, an additional $\times 2$ reduction would yield the same representation for tetrahedral elements. Additionally, a conversion from cubic voxels to tetrahedral elements restricts the minimum element edge length. In order not to falsely manufacture non-existent information, the element volume cannot be lower than the voxel volume. Tetrahedral edge length must thus be at least $\sqrt[3]{6\sqrt{2}}$, or $\sim$2, times larger than the voxel edge length.

An initial convergence test was performed to check the sensitivity to element size. Eight FE models of femur 1, with linear (C3D4) and quadratic (C3D10) elements and maximum edge lengths of 0.080, 0.160, 0.320 and 0.640 mm, were created. Homogeneous elastic material, with a Young's modulus of 3 GPa, was assigned. Boundary conditions were defined so that all translations and rotations were denied for the distal cutting plane. A second boundary condition was applied to the proximal cutting plane, forcing a 2 mm displacement towards the posterior. This was done instead of simulating three-point bending because the larger elements would not have complied well with the boundary conditions required for the latter option. Large deformations were accounted for, and resultant reaction force was logged. Convergence plot is presented in Figure 3.5, and Table 3.1 lists simulation results.

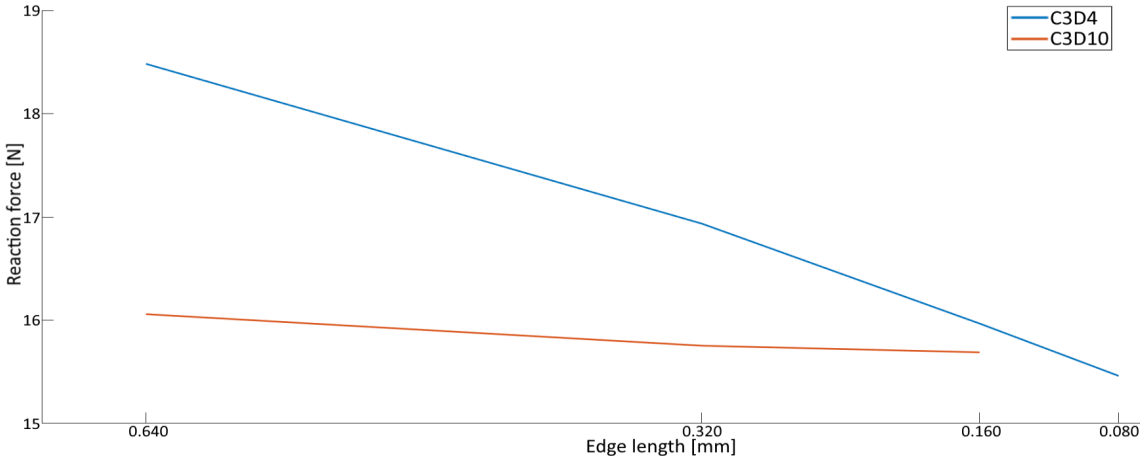

Figure 3.5: Reaction force convergence by p-refinement (linear C3D4 versus quadratic C3D10 element) and h-refinement.

Element type	C3D4				C3D10			
Max Edge length (mm)	0.080	0.160	0.320	0.640	0.080	0.160	0.320	0.640
Number of elements	1.1e7	1.3e6	1.5e5	1.3e4	1.1e7	1.3e6	1.5e5	1.3e4
Number of nodes	1.8e6	2.2e5	2.6e4	2.7e3	1.5e7	1.8e6	2.1e5	2.0e4
Reaction force (N)	15.46	15.97	16.94	18.48	DNF	15.69	15.75	16.06
System memory used (MB):								
Minimum required	7 856	1 037	103	23	48 198	6 276	868	66
Total data transferred	134 489	8 298	565	54	2.0e6	132 122	7 510	375

Table 3.1: Model size, convergence test reaction force and system memory requirement of initial test if different FE models with isotropic Young's modulus. Total data transferred is the minimum system memory plus storage space required to run the simulation.

Higher resultant forces for larger elements conforms with the theory presented in subsection 2.2.2, that tetrahedral elements must be small to accurately represent large deformations. The 0.080 mm quadratic element model did not finish due to excessive data requirement. However, the test indicates that the simulation is more sensitive to the polynomial degree of the element than the size. A quadratic element model with edge length of 0.160 mm was thus chosen for the following simulations. This corresponds to an edge length multiplication of ∼9 times the original voxel.

Since a quadratic tetrahedral element consists of six more nodes than a linear element, this also benefits the efficiency of the IDWI algorithm. Figure 3.6 shows the predicted density distribution for the same femur as Figure 3.4, but using linear C3D4 elements instead. A direct comparison indicates that using quadratic elements yields much more accurate density prediction.

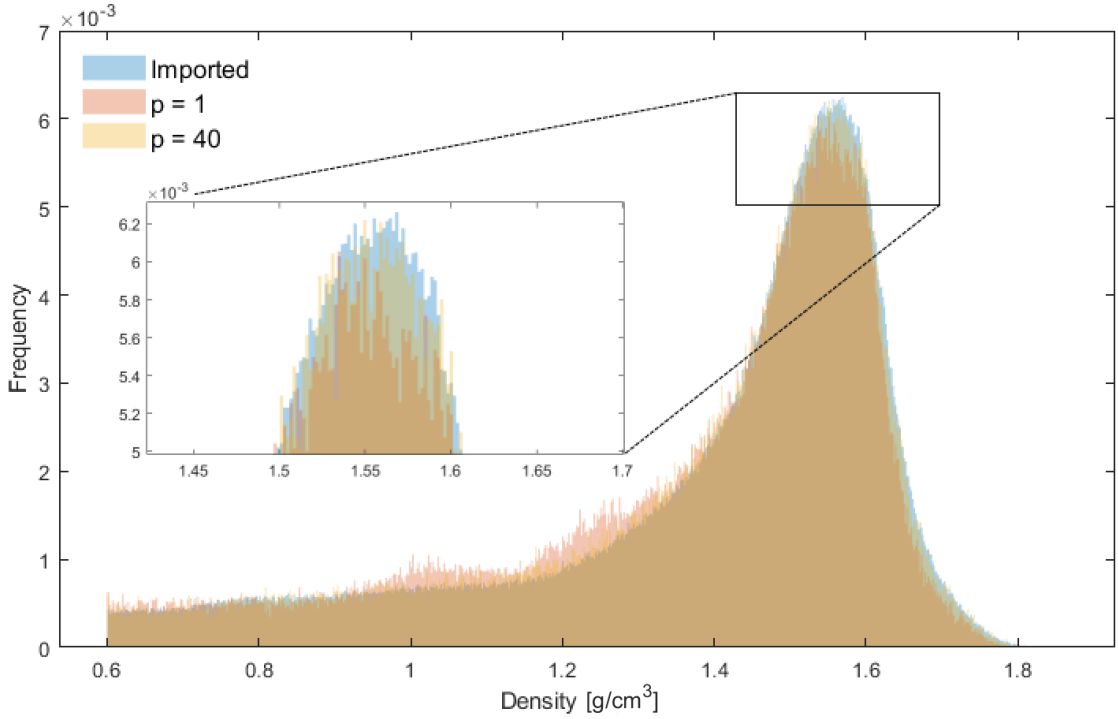

Figure 3.6: Mimics element densities (Imported) versus IDWI with $p = 1$ and $p = 2$. Element type: C3D4.

An additional test was run with the same eight FE models and same boundary conditions, but applying an expression for density-dependent Young's modulus. Resulting reaction forces are presented in Figure 3.7.

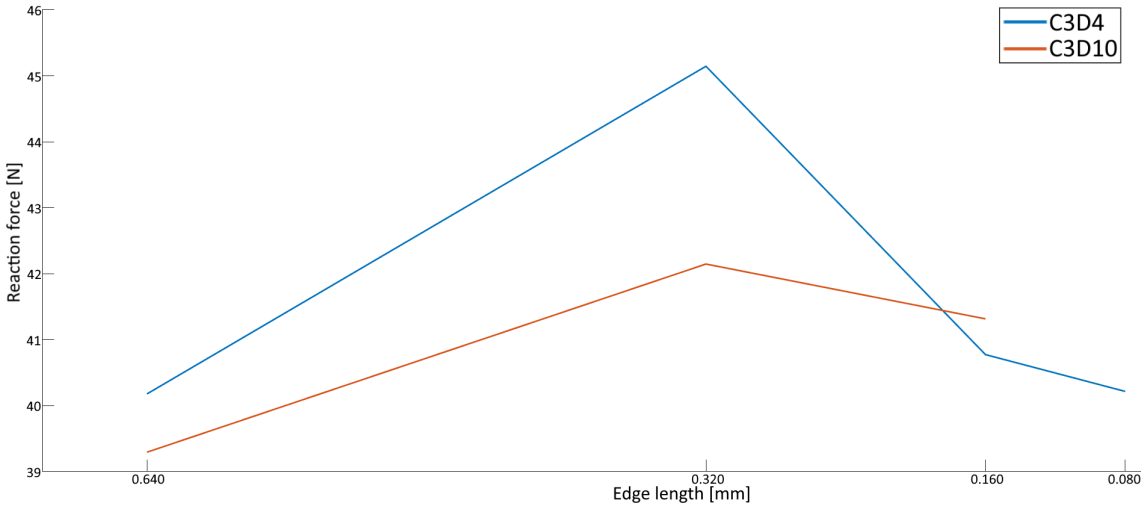

Figure 3.7: Reaction force, density-dependent Young's modulus.

When employing a Young's modulus and density relationship (see subsection 3.2.5), the test did not converge satisfactorily. This is due to a combination of information being lost in Mimics and the IDWI algorithm not working properly for FE models with very large elements. The increased force from 0.640 mm to 0.320 mm edge length corresponds with the increased mean density (Table 3.2). For edge lengths of 0.320 mm and less, the test converges similarly as the one presented in Figure 3.5. It was thus assumed that the 0.160 mm C3D10 was adequately refined for accurate simulations.

It is noted that although Abaqus assigns field variables (density) to nodes, material properties are assigned to the elements. An inbuilt conversion algorithm, using a Gaussian quadrature rule is therefore run by Abaqus to calculate the element densities. Resulting density distributions after this algorithm is applied are presented in Figures 3.8 and 3.9. Maximum, minimum and mean apparent densities for Mimics elements, IDWI nodes and Abaqus elements are listed in Table 3.2 along with reaction forces from the second convergence test.

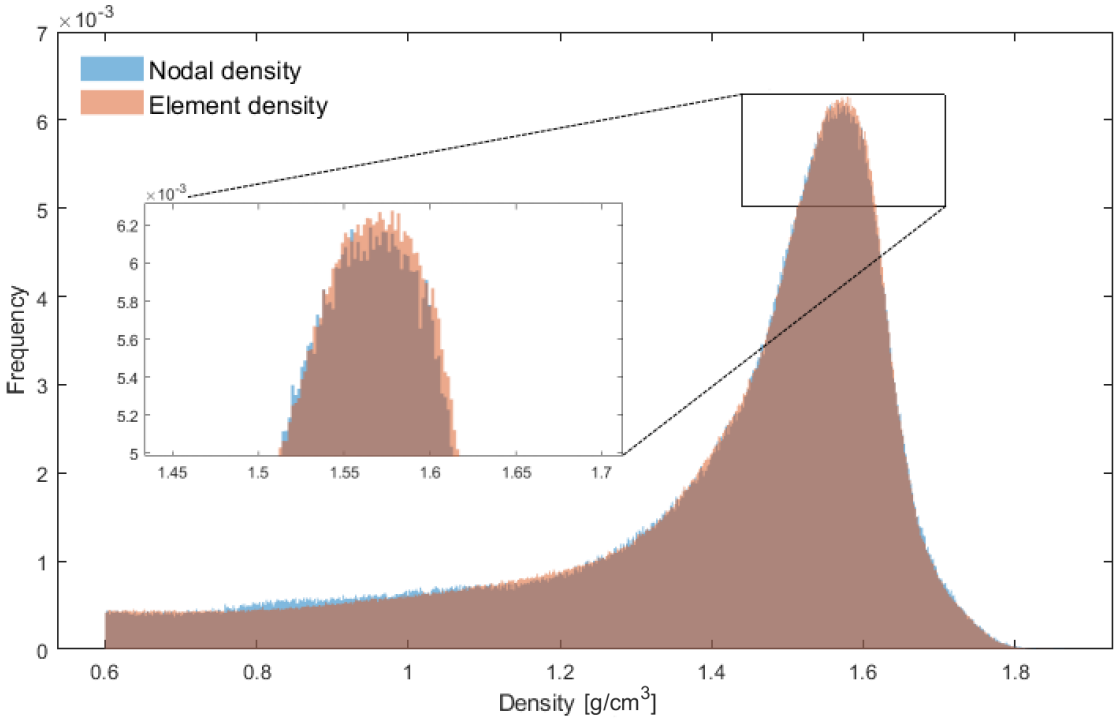

Figure 3.8: IDWI ($p = 40$) (Nodal) versus Abaqus (Element) density distributions. Element type: 0.160 mm C3D10. A small amount of information is lost in the Gauss integration conversion.

Due to the Gauss integration method, the highest apparent density of C3D10 elements can become slightly higher than the highest nodal density. Likewise, lowest element density can be less than the lowest nodal density. Densities below 0.01 g/cm^3 were however considered as empty voids and disregarded in the simulations. For the 0.160 mm C3D10 element, average density increases by 0.3 % from Mimics to Abaqus, which was considered acceptable.

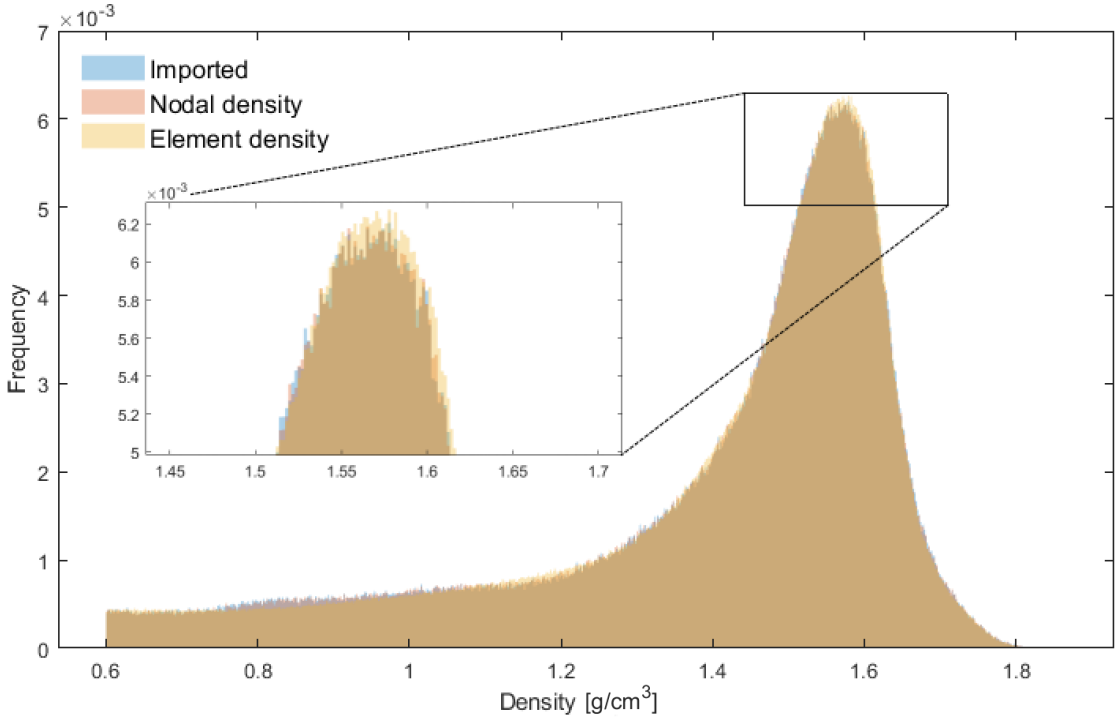

Figure 3.9: Mimics (Imported) versus IDWI (Nodal) versus Abaqus (Element) density distributions, representing the total density deviation between µCT voxels and simulation elements.

Element type	C3D4				C3D10			
Max Edge length (mm)	0.080	0.160	0.320	0.640	0.080	0.160	0.320	0.640
Reaction force (N)	40.22	40.77	45.14	40.18	DNF	41.32	42.15	39.30
Apparent densities: (g/mm^3)								
Mimics elements:								
Maximum	1.877	1.865	1.804	1.756	1.877	1.866	1.804	1.756
Minimum	4.9e-3	9.3e-4	0.107	0.164	4.9e-3	0.055	0.107	0.164
Mean	1.246	1.223	1.210	1.104	1.246	1.243	1.210	1.104
IDWI nodes:								
Maximum	1.865	1.856	1.802	1.731	1.877	1.866	1.804	1.756
Minimum	6.9e-3	0.019	0.119	0.210	5.5e-3	0.057	0.107	0.165
Mean	1.243	1.229	1.229	1.147	1.246	1.246	1.220	1.121
Abaqus element:								
Maximum	1.842	1.805	1.780	1.712	1.894	1.866	1.814	1.839
Minimum	0.063	0.041	0.159	0.224	< 0	0.057	0.119	0.098
Mean	1.248	1.230	1.221	1.099	1.250	1.250	1.220	1.097

Table 3.2: Reaction forces from second test, density-dependent Young's modulus. Maximum, minimum and mean apparent densities for the Mimics elements, IDWI nodes and Abaqus elements.

3.2.5 Defining material properties

In the second initial element test, described in the previous subsection, Young's modulus was calculated from apparent density by a relationship expression. E-ρ relationship formulas have been studied for several years and numerous expressions can be obtained from literature. A nonlinear expression often used is:

$$E = \alpha\rho^{\beta} \tag{3.2}$$

where E is Young's modulus (GPa), ρ is apparent density (g/cm^3) and α and β are empirical values. In order to find a well-fitting material law, a series of tests were conducted, simulating TPBT of femur 4 in a similar manner as described in subsection 3.3.3. Some values for isotropic Young's modulus were evaluated, including the calculated value ($E = 3.6$ GPa) from the experimental bend test (see subsection 3.3.2). Elastic perfectly plastic materials were also defined, using the experimentally measured yield stress ($\sigma_y = 82.45$ MPa). Poisson's ratio was set to 0.3 for all simulations (Wirtz et al. 2000).

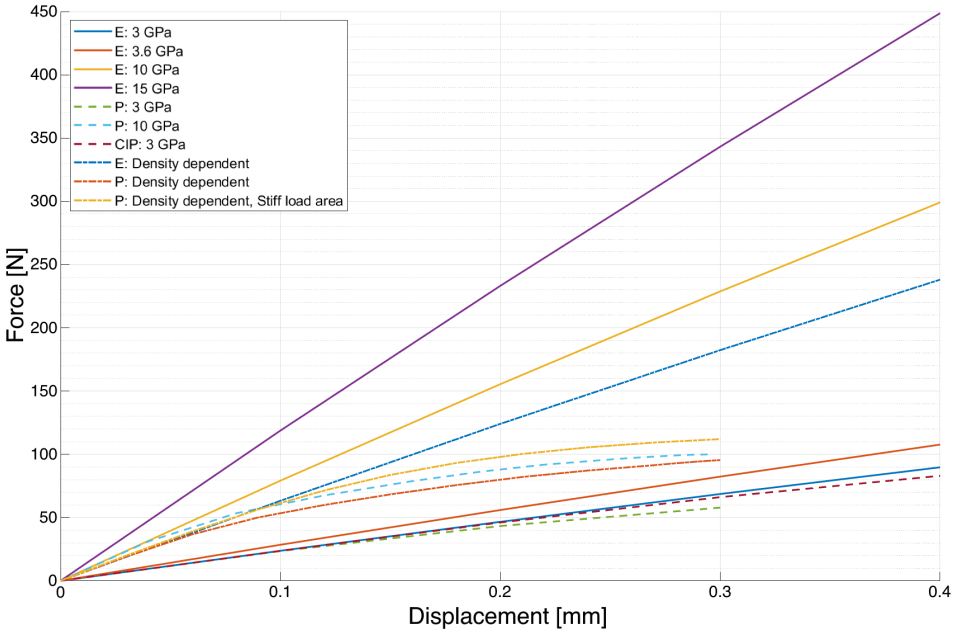

Figure 3.10: Force-displacement curves for simulated TPBT with various materials: E: perfectly elastic; P: elastic perfectly plastic; *CIP*: cast iron plasticity; *Density dependent*: Young's modulus expressed as $E = 2.998\rho^3$ ((GPa), density in g/cm^3).

Figure 3.10 presents the resulting force-displacement plots from the first test. An isotropic Young's modulus between 15 and 10 GPa, which was considered from literature on material stiffness of cortical bone, yielded very high reaction forces. An in-depth discussion on this behavior is presented in section 5.2. Utilizing the same value as measured from experiment, caused the stiffness to be too low, suggesting that some action was needed to refine the simulation procedure. The curves for density-dependent material yielded satisfying results. However, the material law

expression utilized, $E = 2.998\rho^3$ (Gupta and Dan 2004), predicts a much higher Young's modulus than what recent studies suggest. In addition, plasticity occurs earlier than expecting, further suggesting that the material is too stiff. Cast iron plasticity was suggested to reproduce the tension/compression asymmetry described in subsection 2.1.3. Results varied however little from perfectly plastic material and simulations were unlikely to complete. This method was therefore discarded. The curve labeled *P: Density dependent, stiff load area* incorporates stiff elements under the plunger to simulate a full contact analysis. This is further described on page 29.

To overcome some of the challenges related to comparing experimental and virtual TPBT, a second test was conducted to see if the logged displacement at different locations yielded significantly different results (Fig. 3.11). Same material law expression was utilized. The displacement differences between the curves indicate that a combination of ring-type deformation and local indentation is present in the simulation. The curve labeled *Loaded area* is the average displacement of an algorithmically deduced node set which surrounds the loaded nodes but considers none of the loaded nodes themselves.

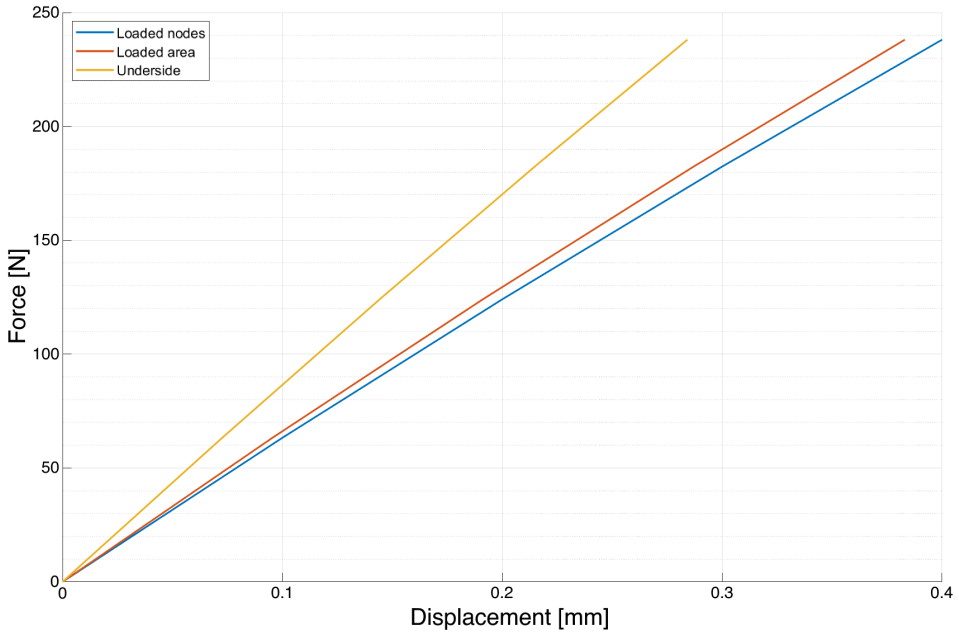

Figure 3.11: Force-displacement curves for simulated TPBT with displacement logged as average displacement at various locations. Density-dependent Young's modulus expressed as $E = 2.998\rho^3$.

Although some local indentation was observed during the experimental TPBT (see section 5.2), it was not as extreme as the indentation in virtual testing. It was therefore decided to log the displacement of the nodes surrounding the loaded surface.

A new test of different material properties was conducted (Fig. 3.12) to assess the inclusion of plasticity. Although plastic behavior was observed in the experimental tests, a well-fitting expression for this behavior was not derived for the virtual testing. In general, yielding occurred at a much lower displacement than expected

when applying the same σ_y as measured experimentally. Expressions for density-dependent yield stress (Ramezanzadehkoldeh and Skallerud 2017a) was suggested, and this might have yielded more accurate results. However, after some initial tests, it was decided to discard this implementation due to excessive computation time. Density-dependent yielding is further discussed in subsection 5.3.3.

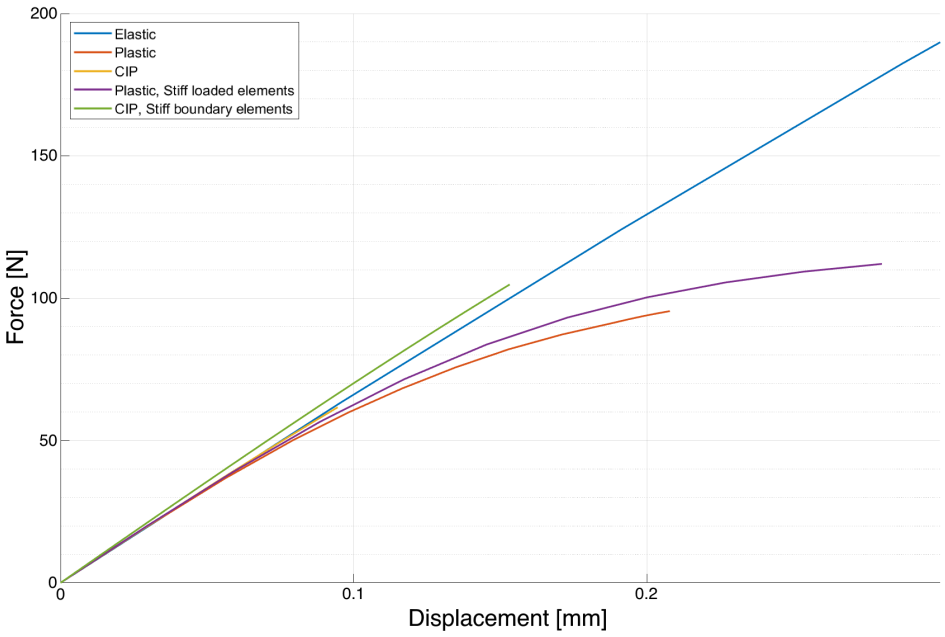

Figure 3.12: Force-displacement curves for simulated TPBT with displacement logged as average displacement of the loaded nodes. Density-dependent Young's modulus expressed as $E = 2.998\rho^3$. Plastic: $\sigma_y = 82.45$ MPa. *Stiff boundary elements* incorporates stiff elements both under the plunger and at the supports. Cast iron plasticity analysis was not able to complete.

Figure 3.12 does indicate that the implementation of stiff boundary elements helps overcome some of the local indentation at contact points. The stiff element algorithm works by finding and listing all elements related to the boundary nodes during the same conversion script as described in subsection 3.2.2 (see Appendix G). These are only the very same surface elements as depicted in Figure 3.1. It is noted that assigning a very high Young's modulus to some elements might cause a stiffer model. However, since the algorithm extracts only the boundary elements, and the number of affected elements is very low, this was not assumed to affect global stiffness significantly. From the three aforementioned tests, it was decided: to use perfectly elastic elements with density-dependent Young's modulus, expressed by Equation (3.2); to log the displacement as the average displacement of a region surrounding the loaded nodes; and to implement stiff elements and boundary surfaces.

The final material property needed to be defined was the expression for the Young's modulus apparent density relationship. Ramezanzadehkoldeh and Skallerud (2017a) achieved a good fit for their simulations by employing $E = 2.065\rho^{3.09}$ (Wirtz et al. 2000). E-ρ plot of this expression, along with other expressions are presented in Figure 3.13.

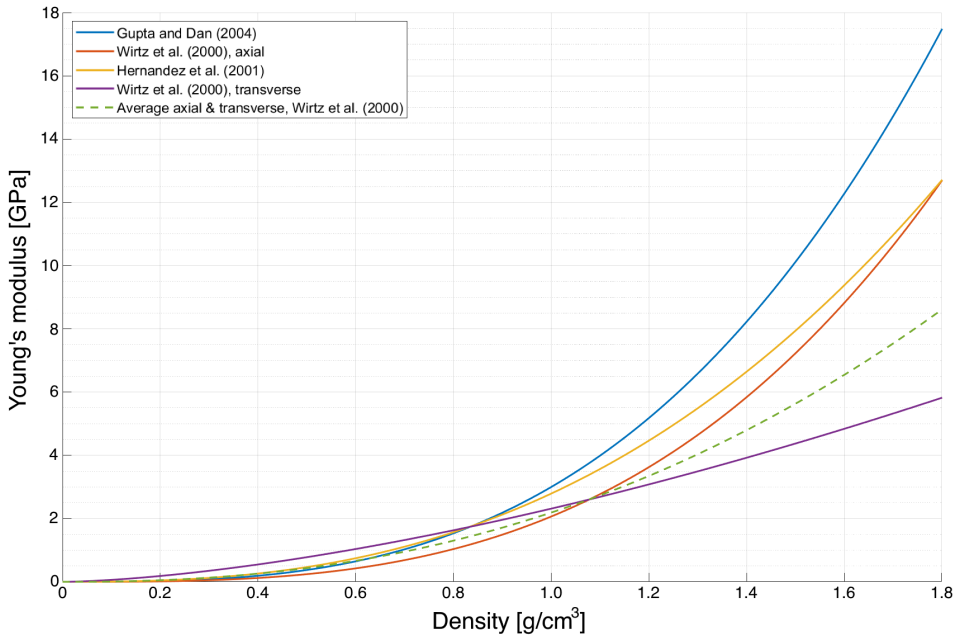

Figure 3.13: Various expressions for Young's modulus apparent density relationship. Gupta and Dan (2004): $E = 2.998\rho^3$; Wirtz et al. (2000), axial: $E = 2.065\rho^{3.09}$; Hernandez et al. (2001): $E = 2.79\rho^{2.58}$; Wirtz et al. (2000), transverse: $E = 2.314\rho^{1.57}$; Average axial & transverse, derived from Wirtz et al. (2000): $E = 2.19\rho^{2.33}$ ((GPa), density in g/cm^3).

It was discussed whether the TPBT setup in this study yielded an aspect ratio, L/d, too low to accurately calculate Young's modulus from bending stiffness (see subsection 3.3.2). In addition to bending and shearing, it might be that the bone was being compressed transversely. Long bones are known for having lower material stiffness in the transverse direction than the longitudinal direction (Table 2.2, subsection 2.1.3), and the sensitivity to this difference was discussed. A sensitivity test, similar to the previous ones, was conducted for the different material laws expressed in Figure 3.13. An additional expression was defined by calculating α and β in Equation (3.2) as the average of the α and β values from the axial and transverse expressions by Wirtz et al. (2000). Resulting force-displacement curves are presented in Figure 3.14.

The averaged axial and transverse material stiffness expression yielded a displacement curve which correlated very well with the experimental curve. Is was therefore considered to employ this expression for the simulations. However, due to a significant number of other possible sources of error, it was also considered a good measure to utilize an already well-established relationship. Which material law to utilize was not decided until simulations of all bones were run with both the averaged expression and the one presented by Wirtz et al. (2000) for axial loading. Consequently, $E = 2.19\rho^{2.33}$ yielded the best fit overall, and was thus defined as the Young's modulus apparent density relationship expression for all following simulations.

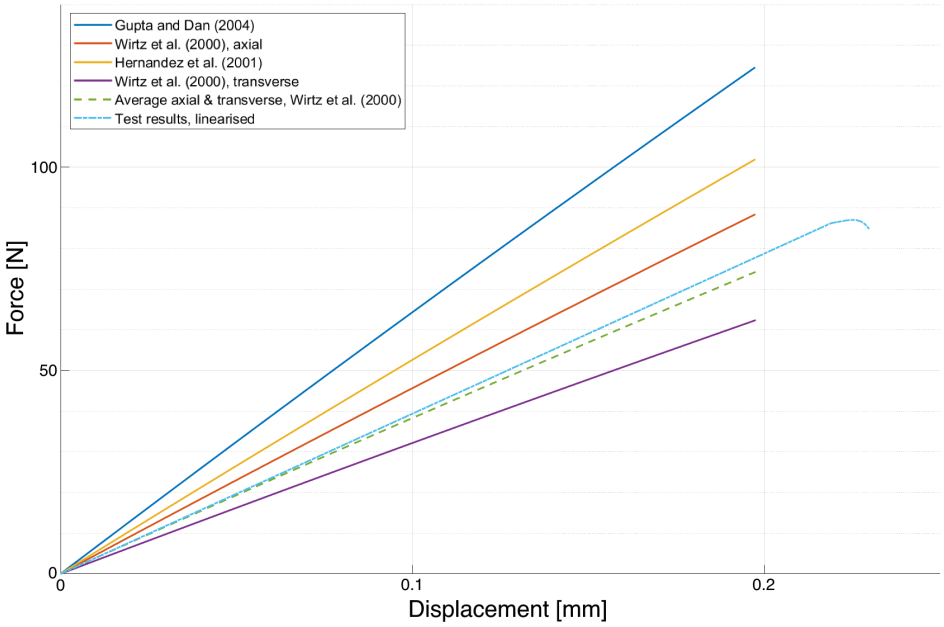

Figure 3.14: Force-displacement curves for simulated TPBT with expressions for Young's modulus as described in Figure 3.13. *Test results, linearized* is the experimental force-displacement of femur 4, which the simulated model is based on.

3.3 Three-point bending test

3.3.1 Experimental testing

Prior to experimental testing, specimens were placed in plastic tubes with fridge-tempered PBS solution and thawed in fridge for one hour. Following, the specimens were moved into room-tempered solution, and thawing was continued for at least two hours in room temperature. It was discussed whether the bones were thawed in much wetter conditions than in similar studies, and whether this might have caused a lower measured Young's modulus. Bonfield and Datta (1974) discovered no significant correlation between wetness and elastic properties when testing this hypothesis, although some changes to non-elastic behavior was observed. In a more recent study, where quasistatic nanoindentation test was employed (Lee et al. 2012), dry test conditions yielded nearly double the Young's modulus and significantly higher hardness than wet conditions. These differences might have affected the measured indices in the present study. Excess PBS solution was removed from each specimen before seating in the testing machine.

Three-point bending tests were conducted with a material-testing machine (Model 5944, 2kN single column machine, Instron Corp., Illinois, USA). Femurs were seated with the posterior surface facing downwards on triangular supports which were positioned 12 mm apart. A triangular plunger was positioned over the mid-span. In order to ensure proper seating, the plunger was moved manually down towards the anterior surface until a preload of 0.5 N was established. Following, the plunger was moved at a constant speed of 0.5 mm/min until fracture. Femur 24 was already broken before the testing and was thus excluded from the study.

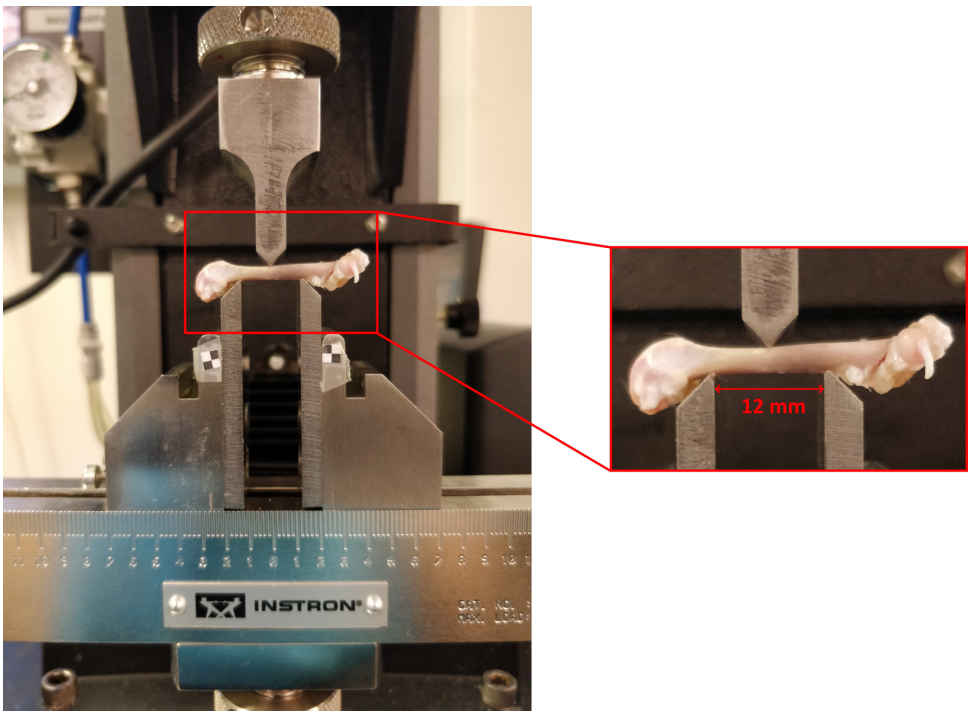

Figure 3.15: Experimental test setup

3.3.2 Data acquisition from experimental test

Force and displacement data from the material testing machine was logged at 10 Hz frequency, providing force-displacement graphs. The raw test results and all measured values are shown in Appendix B:E. Global stiffness, yield force, ultimate force and total work was calculated from these graphs. Femur 9 and 10 were excluded from the study due to dissatisfying bending behavior.

Global stiffness was calculated as the steepest average slope of the force-displacement curve where 11 successive data points, corresponding to approximately 0.01 mm plunger movement, varied by a minimum amount. The acceptable variation was incrementally increased until such a region was found, resulting in 2–8 % variance for every specimen. For easier comparison of results with the FE analyses, the initial non-linear region of the curves and the data after first yield was disregarded.

Nominal Young's modulus was derived from global stiffness. If the aspect ratio, L/d, of a bending beam is high enough, and shear stresses are negligible, Euler-Bernoulli beam theory can be applied (Eq. (3.3)). Two important assumptions are that plane sections remain plane and that deformation angles are small. This is applicable to long beams with small displacements, and an aspect ratio of >10 is preferred. However, due to the aspect ratio of the respective test setup being less than approximately 4, transverse shearing is assumed to be present. Nominal Young's modulus was thus derived by use of Timoshenko beam theory (Eq. (3.4)) , which instead assumes that cross sections remain plane (Ramezanzadehkoldeh and Skallerud 2017a).

$$E = \frac{F}{D}\frac{L^3}{48I_x} \tag{3.3}$$

$$E = \frac{F}{D}\frac{L^3}{48I_x}\left(1 + 12\left(\frac{E}{G}\right)k\frac{I_x/A}{L^2}\right) \tag{3.4}$$

Here, F is applied force, D is displacement of plunger, L is beam length, or length between the supports, and k is a constant equal to 1.2 (Spatz et al. 1996). In their study, Ramezanzadehkoldeh and Skallerud (2017a) assumed a constant shear modulus, G, equal to 6 GPa for all specimens, which was obtained by Kohles et al. (1997). However, due to low resulting Young's modulus measurements, G was here calculated from the Young's modulus of an isotropic material:

$$G = \frac{E}{2\,(1+\nu)} \tag{3.5}$$

where the Poisson's ratio, ν, is given a value of 0.3. This solution might pose limitation since bone is known to be anisotropic (see subsection 2.1.3). By combining Equations (3.4) and (3.5), the resulting expression for Young's modulus becomes:

$$E = \frac{F}{D}\frac{L^3}{48 I_x}\left(1 + 24\,(1+\nu)\,k\frac{I_x/A}{L^2}\right) \tag{3.6}$$

A is the specimen-specific cross section area underneath plunger. It was calculated with disregard to voxel density by image processing of the CT images. I_x is the respective 2nd moment of area, calculated using the parallel axis theorem (Ramezanzadehkoldeh and Skallerud 2017a):

$$I_x = \sum_{voxels}\left(y_i^2 A_{i,voxel} + \int_{voxel\ area,i} y_{local,i}^2 dA\right) \tag{3.7}$$

Nominal yield and ultimate stresses were calculated with the same formula used by Schriefer et al. (2005), which is derived from Euler-Bernoulli beam theory:

$$\sigma_y = F_y\left(\frac{Lc}{4I_x}\right), \quad \sigma_U = F_U\left(\frac{Lc}{4I_x}\right) \tag{3.8}$$

F_y and F_U are the forces at the onset of yielding and maximum force and c is the distance from the neutral axis to the fiber which is farthest away in **y**-direction. This is where the largest bending stress occurs. Due to the non-linear initial regions of the force-displacement curves, it is impractical to define the yielding force by using conventional methods. Therefore, yielding was assumed when the mean slope of 11 successive force-displacement data points dropped to 50 % below global stiffness.

3.3.3 Virtual testing

All volumetric femur models, with boundary nodes were created and finalized in 3-matic (Materialise NV) (see section 3.2). Simulations were performed using Abaqus FEA (Dassault Systèmes Simulia Corp., Johnston, Rhode Island, USA). Translation in all directions was denied for the distal contact surface nodes, while translation in **y**-direction was denied for the proximal contact surface nodes (Fig. 3.16). Since the number of nodes representing contact with the plunger varied between models, a forced displacement boundary condition was chosen instead of an applied force.

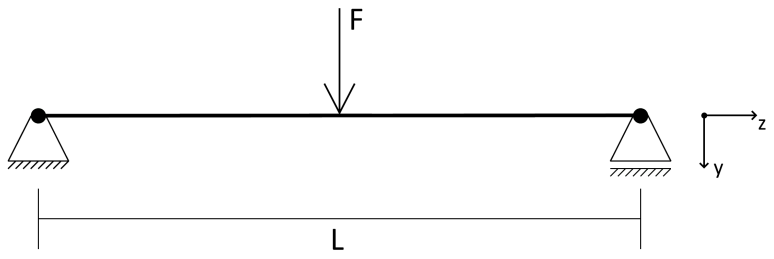

Figure 3.16: Schematic representation of the virtual TPBT setup.

In a static analysis simulation, accounting for large deformations, the surface nodes under the plunger were given a constant displacement from 0 to 0.2 mm in 0.01 mm increments. Field output was recorded every increment, 20 increments in total.

Following the FE modeling method by Ramezanzadehkoldeh and Skallerud (2017a), a full contact analysis simulation would possibly have yielded better fitting results. In contrast, the simulation method used for this study, with applied boundary conditions, is likely to pose significant limitations. In order to overcome some of the related weaknesses, every element related to a surface in contact with either support or plunger were given a very high Young's modulus to replicate the contact material of the testing machine. Displacement was logged as the average displacement of the nodes surrounding the loaded surface, as described in subsection 3.2.5. Resultant reaction force was measured as the sum of all reaction forces in **y**-direction acting on the nodes subjected to a displacement.

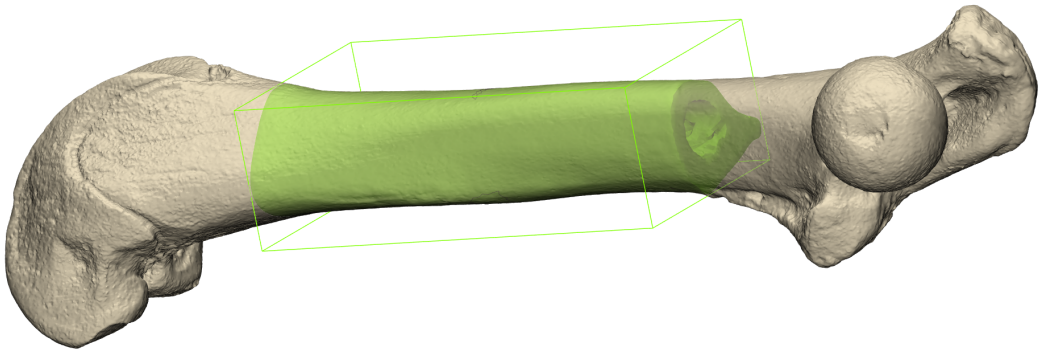

Figure 3.17: Cortical section (green) retrieved from femur model.

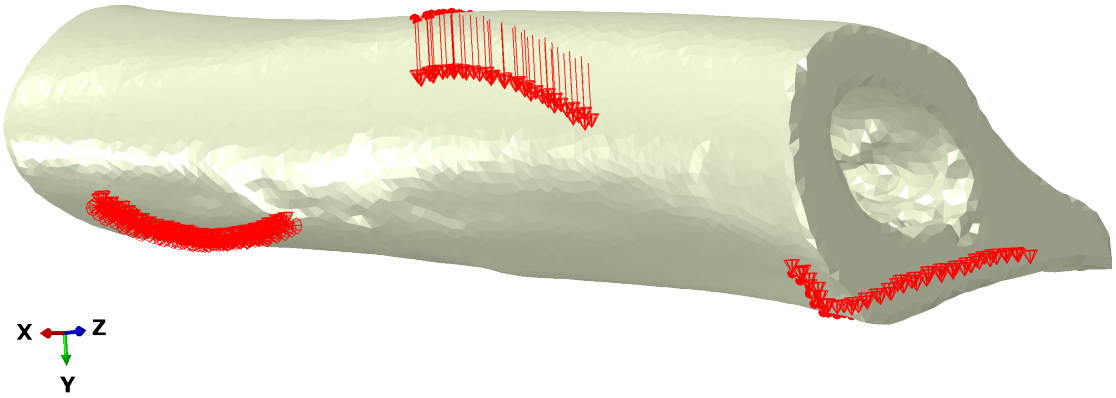

Figure 3.18: Example illustration of virtual TPBT performed in Abaqus. Distal boundary nodes (left in picture) are denied all translations, proximal boundary nodes (right) are denied translation in **y**-direction, loaded nodes (middle) are subjected to a forced displacement downwards.

3.3.4 Data comparison and statistical analysis

For the two experimental TPBTs, mean ± standard deviation values of global response values (stiffness, yield force, ultimate force) were measured. Additionally, intrinsic properties (Young's modulus, yield stress and ultimate stress) were calculated and compared. Results from the first test were analyzed with respect to time of euthanasia due to the important physiological properties of rats (see subsection 2.1.4). An independent two-tailed t-test, with a P-value <0.05 considered to be significant, was also employed for comparison between the two groups in each bending test.

For comparison between experimental and simulated TPBT of femur 1–24, regression analysis was used for global stiffness and Young's modulus. Global Young's moduli of the FE models were calculated by the Timoshenko formula (Eq. (3.4)) in the same manner as for the experimental tests. Additionally, yield forces from the FE models was deduced by logging maximum principal stress at the underside of the femur. Yielding was assumed when the principal stress reached the same magnitude as the measured yield stress of the respective experimental test. Yield force correlation was assessed by regression analysis as well.

3.4 Simulation script

It must be noted that the simulation of training and radiation presented in this section is to be considered as a preliminary proof of concept. Some simplifications were employed, and assumptions were made on occasions where literature did not present practical solutions. Nevertheless, the work presented here could lay a foundation for future studies.

One femur model was chosen to virtual training and radiation. By applying the different exercise recordings of different rats to a single model, resulting density distributions and bending stiffness from each simulation could be compared with the respective experimental test results. A full model (including both epiphyses) of femur 15 was created. Rat 15 was in the control group and was thus neither radiated nor trained. The full femur model was meshed in the same manner as the TPBT models, but the elements forming the epiphyseal regions were given a maximum edge length of 0.64 mm (Fig. 3.19). This was done to reduce the number of elements, and since these regions would be excluded from the following bending test, the large elements would not affect the resulting model stiffness.

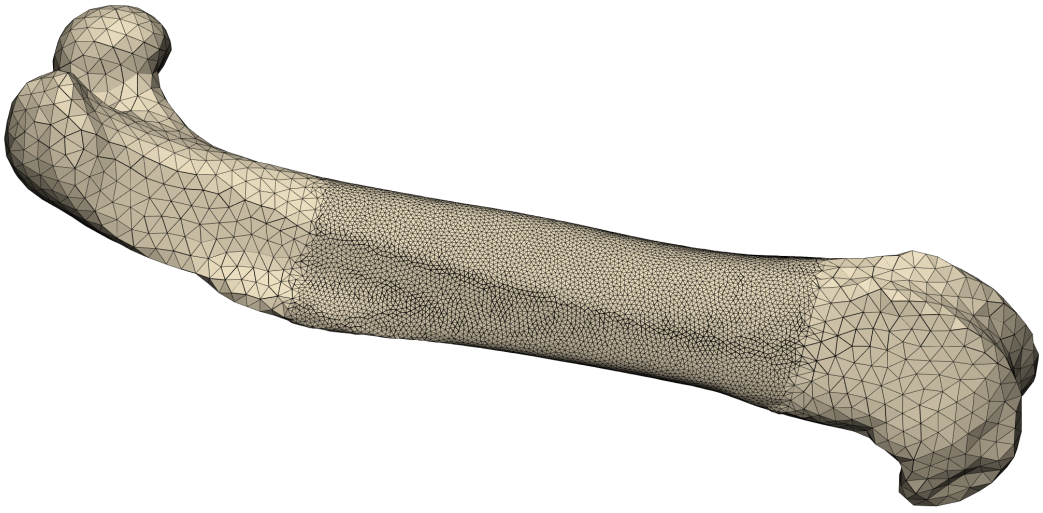

Figure 3.19: Meshed model of training/radiation-simulated femur.

The training and radiation simulation script was written in MATLAB. Full code is found in Appendix H. A loop was repeated for every day of either training or radiation. If training was conducted, the actions described in subsections 3.4.1 and 3.4.2 were applied and new densities were calculated. The procedure for days with radiation is described in subsection 3.4.3. After completing the loop, completing the rat's training/radiation program, the final model with new nodal densities was cut to match the length of the other TPBT models and prepared for bending test. The bending test was performed in the same manner as described in subsection 3.3.3, with the same data being recorded.

3.4.1 Training

The dynamic action of a jump was simplified into static load cases for execution in Abaqus. Instead of contact with other bones in each joint, a combination of boundary conditions and applied forces were defined to represent the joints and active muscles (Fig. 3.20). The distal epiphyseal surface was denied translation, and forces were applied to the proximal epiphysis and metaphysis. Quadriceps muscle attachment points were approximated by following descriptions by Johnson et al. (2008) and Charles et al. (2016a). The hamstring muscles were represented by applying additional force on the femoral head, while the glutes were excluded because of assumed little contribution to the total load on the femur.

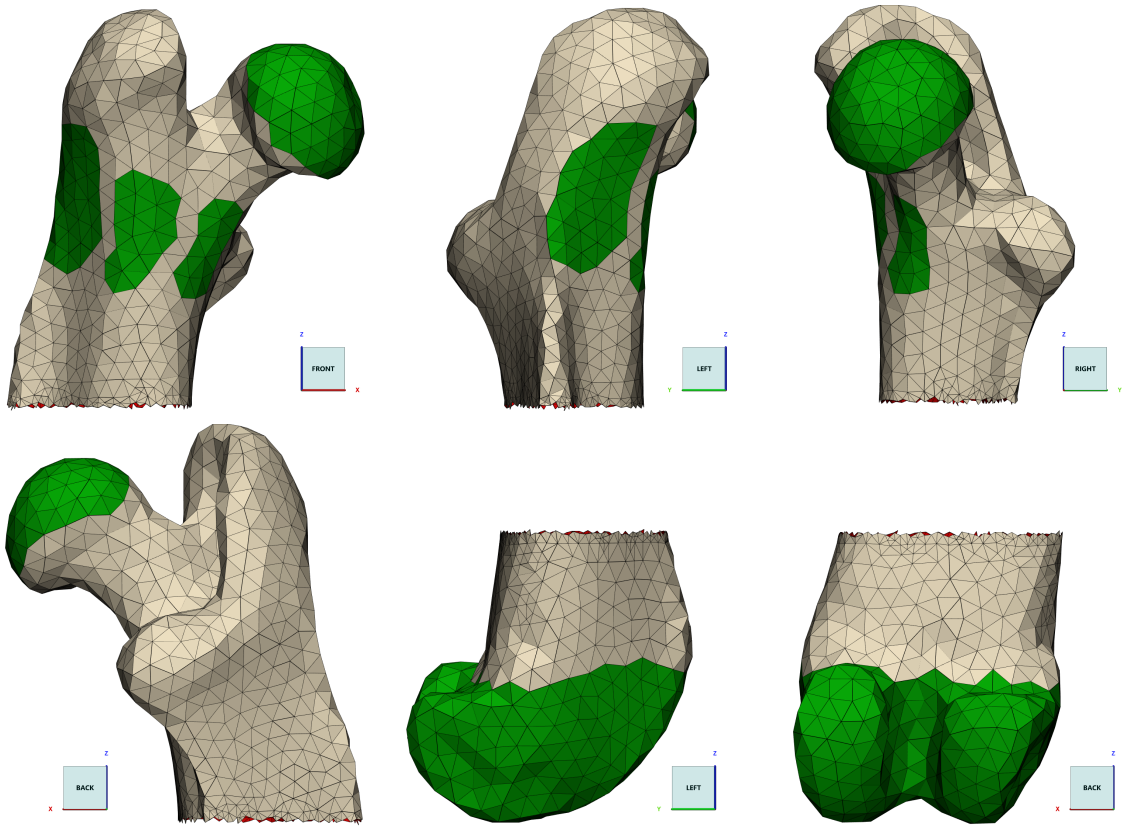

Figure 3.20: Muscle attachment points.

Loading for each jumping simulation was initially calculated from the formulas for total force presented in section 2.1. A constant $F_{body} = \frac{1}{2}\sum F$ (Eq. (2.2)) was applied to the femoral head to represent the mass of the rat being lifted. Since the femur orientation during a jump goes from slightly tilted downwards to steeply tilted upwards (Fig. 2.3), the loading direction was changed during the simulation. This was done by presenting two perpendicular forces, one axially (negative **z**-direction) and one transversely (positive **y**-direction). By gradually increasing and decreasing the amplitudes of the two load vectors, the net force from lifting the body remained even. The loading direction of the quadriceps muscles was calculated approximately with respect to the position of the patella (Fig. 3.21). The load vector $\mathbf{F}_{quad} = F_{quad}[\ x\ ,\ y\ ,\ z\ ] = F_{quad}[\ 0\ ,\ -0.105\ ,\ -0.995\ ]$ was estimated. The hamstring force, F_{ham}, was defined with a constant negative **z**-direction.

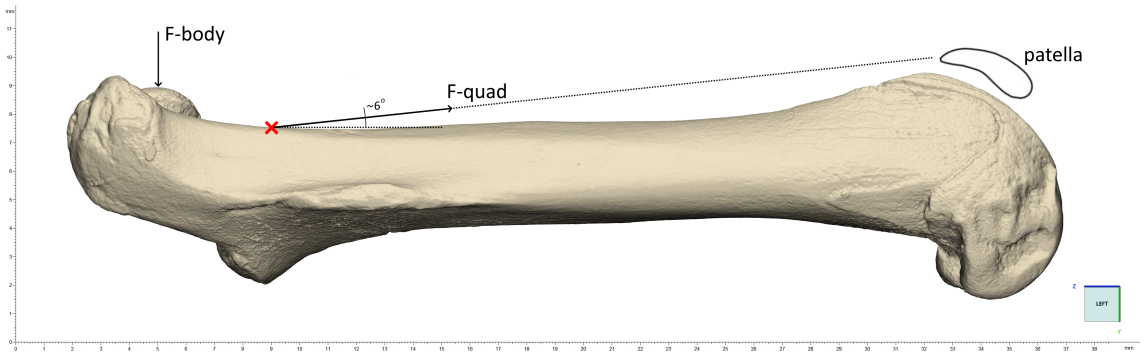

Figure 3.21: Muscle force directions. ✖ indicates roughly the quadriceps muscles' attachment point.

A load amplitude ranging between 0 and 1 was defined for each muscle load. This way, the force directions remained constant throughout the jump simulation, while their magnitude varied with respect to femur orientation and muscle activation time. A total of 4 amplitudes were defined: one for the quadriceps, A_Q; one for the hamstrings, A_H; and one each for the axial and transverse loads of the body mass, A_{HA}, A_{HT} (Fig. 3.22). The amplitudes were inspired by various musculoskeletal studies by Johnson et al. (2008), Yeo et al. (2011), and Charles et al. (2016a).

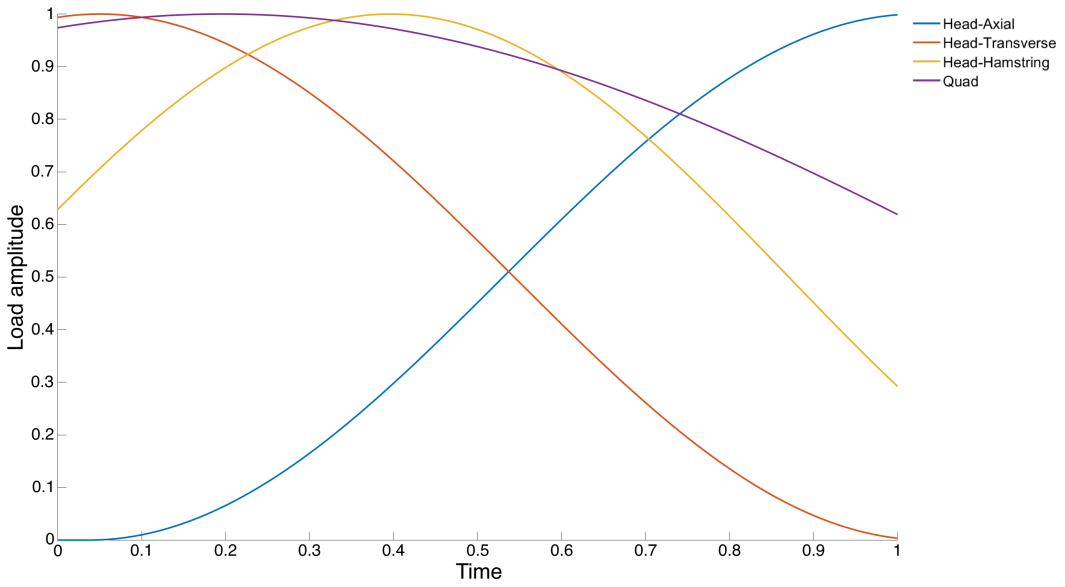

Figure 3.22: Muscle load amplitudes. Calculated reference forces were multiplied with their respective amplitudes. *Head-Axial*: $A_{HA} = \frac{1}{2}\cos\frac{10(t+0.95)}{\pi} + 0.5$; *Head-Transverse*: $A_{HT} = \frac{1}{2}\cos\frac{10(t-0.05)}{\pi} + 0.5$; *Head-Hamstring*: $A_H = \frac{1}{2}\cos\frac{10.4(t+3.4)}{\pi} + 0.5$; *Quad*: $A_Q = \frac{1}{2}\cos\frac{5.2(t+3.6)}{\pi} + 0.5$.

Since the simulation time (running from 0 to 1 s) is analogous to the joint angles, the load amplitudes are naturally expressed by trigonometric functions. Following the time in Figure 3.22, the femur goes from tilted downwards to horizontal at 0.05 s. This is when the quadriceps exert the highest force. Prior to this moment, the axial body load is 0. The hamstring force is greatest just before the bone angle is 45° (0.55 s). After this, all muscle forces decrease while the axial body force increases.

Quadriceps muscle reference force was defined as $F_{quad} = \frac{28}{24\sin(6°)}F_{body} \approx 11F_{body}$ (Fig. 3.21). The hamstring reference force expression, F_{ham}, was however more speculative. Since this muscle group is responsible for hip extension, it is unlikely to exert as much force during a jump as the quadriceps. In addition, due to the way the hamstring load was configured in this setup, its contribution would be nearly indistinguishable from that by F_{body}. It was thus initially suggested to let $F_{ham} = \frac{1}{2}F_{body}$, with the possibility for later optimization.

Reference force	Direction	Load amplitude	Abaqus load case
$F_{body} = \frac{1}{2}m(a+g)$	$[0, 0, -1]$	$A_{HA} = \frac{1}{2}\cos\frac{10(t+0.95)}{\pi} + 0.5$	$F_1 = A_{HA}F_{body}$
	$[0, 1, 0]$	$A_{HT} = \frac{1}{2}\cos\frac{10(t-0.05)}{\pi} + 0.5$	$F_2 = A_{HT}F_{body}$
$F_{ham} = \frac{1}{2}F_{body}$	$[0, 0, -1]$	$A_H = \frac{1}{2}\cos\frac{10.4(t+3.4)}{\pi} + 0.5$	$F_3 = A_H F_{ham}$
$F_{quad} = 11F_{body}$	$[0, -0.105, -0.995]$	$A_Q = \frac{1}{2}\cos\frac{5.2(t+3.6)}{\pi} + 0.5$	$F_4 = A_Q F_{quad}$

Table 3.3: Abaqus load cases

In order to obtain the loading contribution from every jump, an equation which accumulates multiple individual loading events with various magnitudes was employed. This equation was initially proposed by Carter and colleagues (Beaupré et al. 1990; Carter et al. 1987; Whalen et al. 1988) with the means to estimate a daily stress stimulus, ψ, resulting in either formation, resorption or maintenance of apparent density:

$$\psi = \left[\sum_{day} n_i \left(\sigma_i\right)^M\right]^{\frac{1}{M}} \tag{3.9}$$

where n_i is the number of times per day each effective stress magnitude, σ_i, is applied. The exponent, $M > 1$, is a constant which defines the weighting of higher magnitude loads. With increasing values of M, Equation (3.9) emphasizes high magnitude loads, such as jumping, more than regular loads, like standing and walking. This daily stress stimulus theory has since been used in many computational studies. For this study, however, it was proposed to employ the same formula for predicting an accumulated jump height. This way, all the jumps performed by each rat during an exercise session could be condensed into one single simulation:

$$h = \left[\sum_{day} n_i \left(h_i\right)^M\right]^{\frac{1}{M}} \tag{3.10}$$

Since the jumping height, h, together with body mass predicts the loading magnitudes, applied loads were calculated after using this formula. It was considered that a single load case derived from the average height would yield insufficient load, while a standard summation of all jump heights would cause too much load.

3.4.2 Adaptation

After each completed jumping simulation, the nodal densities were updated in accordance with bone adaptation. For this job, a formulation of Huiskes's model was employed (Huiskes et al. 1987):

$$\frac{d\rho}{dt} = \begin{cases} B\left(\frac{U}{\rho} - (1-s)\cdot k\right), & \text{if } \frac{U}{\rho} < (1-s)\cdot k \\ 0, & \text{otherwise} \\ B\left(\frac{U}{\rho} - (1+s)\cdot k\right), & \text{if } \frac{U}{\rho} > (1+s)\cdot k \end{cases} \tag{3.11}$$

This formula considers the strain energy density (SED), U, at every location, which for linear isotropic materials undergoing small strains is calculated as:

$$U = \frac{1}{2}\sigma_{ij}\varepsilon_{ij} \tag{3.12}$$

where σ_{ij} and ε_{ij} are resulting stresses and strains, respectively, and i, j denotes each direction in the Cartesian coordinate system. B is a remodeling rate coefficient, regulating the adaptation intensity. k is a reference stimulus which represents the homeostatic balance point between formation and absorption, and s is a homeostatic plateau length. Applying a forward Euler scheme to Eq. (3.11) yields:

$$\rho_{t+\Delta t} = \begin{cases} \rho_t + \Delta t \times B\left(\frac{U_t}{\rho_t} - (1-s)\cdot k\right), & \text{if } \frac{U_t}{\rho_t} < (1-s)\cdot k \\ \rho_t, & \text{otherwise} \\ \rho_t + \Delta t \times B\left(\frac{U_t}{\rho_t} - (1+s)\cdot k\right), & \text{if } \frac{U_t}{\rho_t} > (1+s)\cdot k \end{cases} \tag{3.13}$$

which can be schematically visualized:

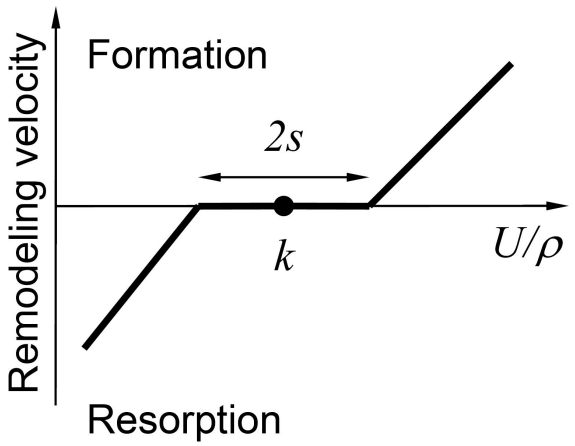

Figure 3.23: Huiskes's model for bone adaptation rate. The plateau depicts the equilibrium state between formation and resorption.

Huiskes's model was originally proposed for predicting the density distribution in a trabecular bone region for a model with an initially uniform density distribution. Applying this model to a cortical region with already defined densities is however not well documented in literature. This model might thus pose a potential limitation to the respective adaptation simulation. Nevertheless, the model was employed due to its well-defined variables and easy inclusion of radiation damage. Some values of B, k and s were proposed by Weinans et al. (1992). However, these values were derived for human bone models, and new values were thus considered for the rodent bone model in this study.

3.4.3 Radiation

Three different stages of radiation damage were considered for the simulation (see subsection 2.1.5): immediate damage which causes collagen phase diminishing and BMD loss; lasting damage, where bone formation becomes unbalanced and leans heavier towards resorption; and damage to adaptation efficiency.

The immediate adverse impact on bone density was simulated by direct reduction of each nodal density. A damage rate coefficient expression, where increased radiation dose yields a greater damage, up to a certain point, was proposed:

$$\rho_{t+\Delta t} = \rho_t \times \big(1 - f(r_t)\big), \quad 1 - f(r_t) = 1 - \frac{1}{10\alpha} \times \min\big(\, \ln(r_t + 1) \;,\; \alpha \,\big) \tag{3.14}$$

Here, r_t is the radiation dose (Gy) and α is the value regulating the damage intensity. By employing a logarithmic relationship between radiation dose and resulting density reduction, the maximum inflicted damage was controlled. This would hinder very high radiations from completely removing all bone. The divisor, 10α, predicts a maximum density reduction of 10 %, regardless of radiation dose. This value was based on the average percentile quality reduction from different doses, measured by Bartlow et al. (2018) and Mustafy et al. (2018). With a radiation dose of 2×8 Gy, Chandra et al. (2014) did obtain a 51 % reduction of trabecular bone stiffness by using FE analysis. Their FE method was however not described, and radiation has been shown to impact trabecular bone more adversely than cortical bone (Mustafy et al. 2018). Such a high damage rate coefficient was thus considered improbable for this simulation.

It is noted that various physiological events take much shorter time in rats than in humans. Additionally, their growth plate does not close and bone growth does not cease at skeletal maturity (Chandra et al. 2014). Rats are therefore able to recover from radiation damage to some extent (Karim and Judex 2014; Mustafy et al. 2018; Bartlow et al. 2018). The value of α, which controls both the curve slope and the maximum of the damage rate coefficient, was adjusted to account for these factors. Curve plots of Equation (3.14) with different values of α are presented in Figure 3.24. In a future study, depending on the simulation setup, different values of the divisor, 10α, should be assessed (Fig. 3.25).

For the same reasons as described above, prediction of later radiation damage would be highly uncertain and possibly not observable the present simulation study. The long-term impact of radiation was thus not considered in the script.

The same damage formula was also applied to the variables in Huiskes's model (Eq. (3.11)), to represent radiation impact on adaptation. The remodeling rate coefficient, B, was decreased by $\times\big(1 - f(r_t)\big)$, representing decreased adaptation efficiency, while the reference stimulus, k, was increased by $\times\big(1 + f(r_t)\big)$ to imply a higher SED needed to activate formation. Since B is equal for formation and resorption, the radiation damage would also reduce the resorption rate, which might inaccurately represent the true physiological response to radiation. For future studies, separate variables, $B_{formation}$ and $B_{resorption}$, should perhaps be considered.

Note that the assumption of radiation-induced BMD loss, and thus reduced Young's modulus, in cortical bone does not fully conform with literature. This may have posed a limitation to the simulation method. A further discussion is made in section 5.4.

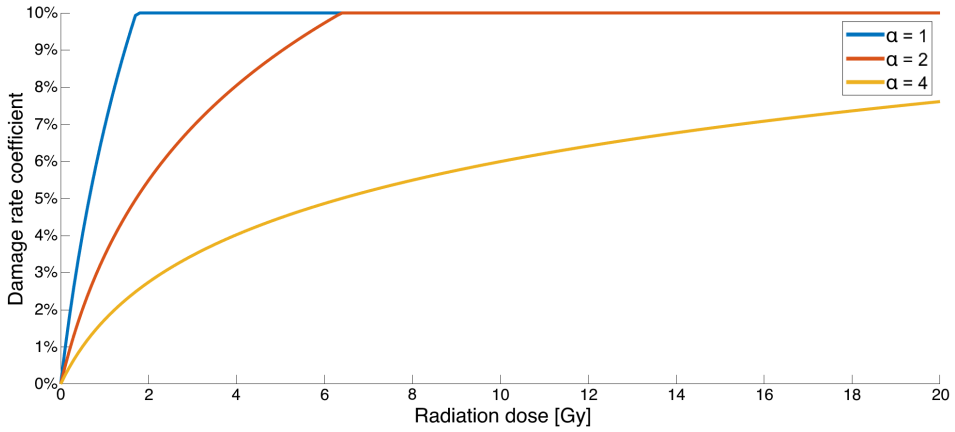

Figure 3.24: Radiation damage rate coefficient. $f(r_t) = 1 - \frac{1}{10\alpha} \times \min\big(\ \ln(r_t + 1)\ ,\ \alpha\ \big)$.

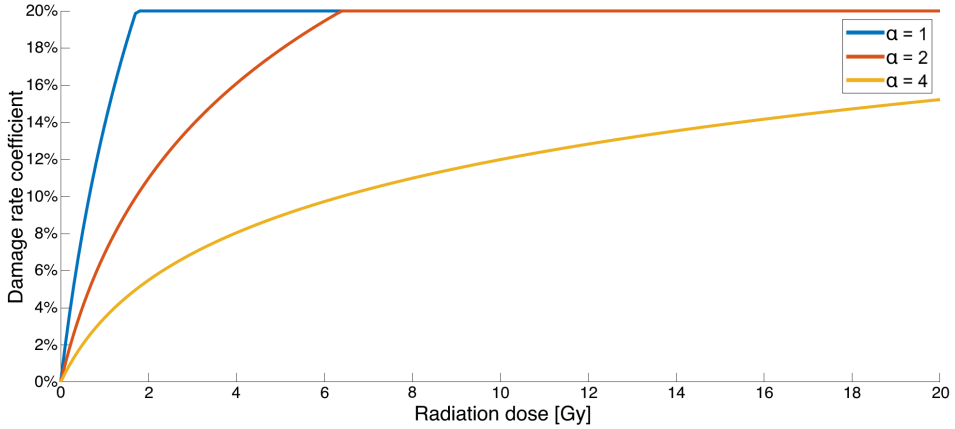

Figure 3.25: Radiation damage rate coefficient. $f(r_t) = 1 - \frac{1}{5\alpha} \times \min\big(\ \ln(r_t + 1)\ ,\ \alpha\ \big)$.

4 | Results

4.1 Experimental bending test of femur 1–23

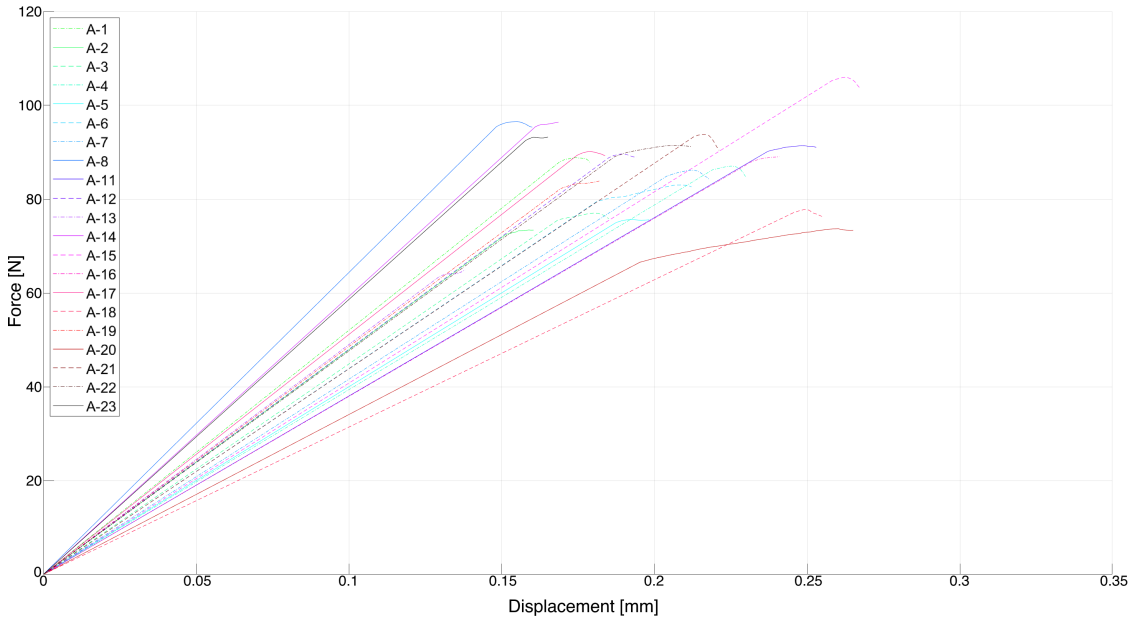

Figure 4.1: Linearized force-displacement plot of first test. Rat 9, 10 and 24 are excluded. Color code corresponds with the full plot in Appendix C.

Figure 4.1 shows a cleaned and linearized representation of the force-displacement curves from the first experimental TPBT of radiated (Rad-1) and non-radiated (Ctrl) rat femurs. The linear region is the same slope as the measured global stiffness, meaning that the relationship between yielding and displacement is not accurately represented in the respective figure. The curves are cut off right after the first onset of yielding. Due to the continuous growing of rat femurs throughout their life, measurements are plotted at their respective weeks of euthanasia in Figure 4.2. There are some indications of radiation causing reduced bone quality improvement through growth reduction. At week 9 after radiation, the control group saw a higher increase in global stiffness and yield force, compared to the radiated group. An overall increase in Young's modulus in the control group, compared to a decrease in the radiated group, was also observed. Ultimate force, yield stress and ultimate stress decreased steadily in the radiated group while the control group saw no significant changes in these parameters during the time span. These findings are indicative of radiation negatively impacting some material properties of cortical bone when

accounting for the time aspect. However, the comparisons of each result, presented in Table 4.1, denotes a level of significance too low for the test to confirm this suggestion.

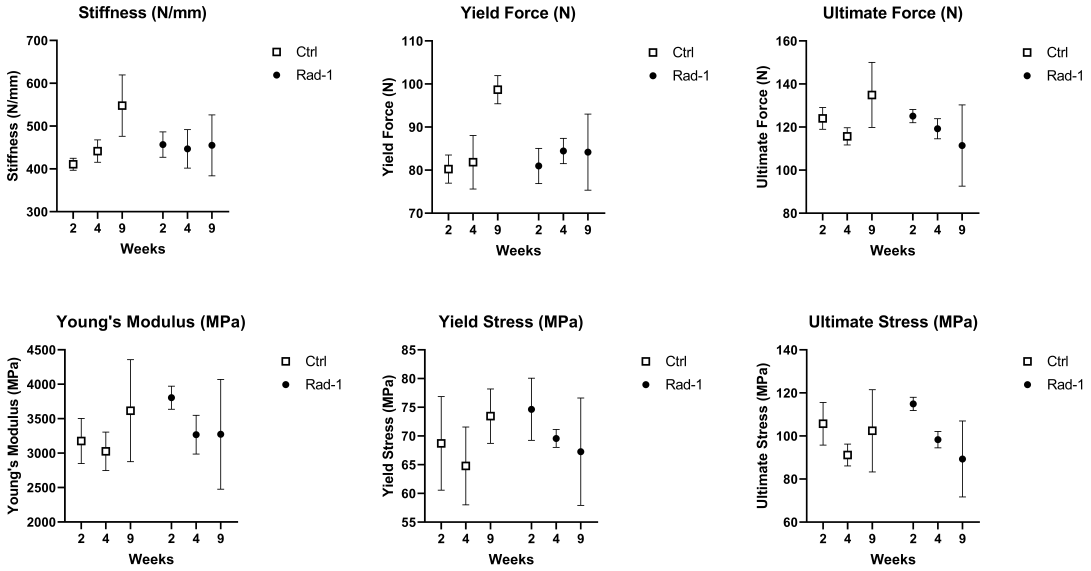

Figure 4.2: Global stiffness, yield force, ultimate force, Young's modulus, yield stress and ultimate stress of radiated (Rad-1) and non-radiated (Ctrl) femurs, plotted over time. Values are presented as mean and standard error of the mean.

	2 weeks		4 weeks		9 weeks	
	Ctrl	Rad-1	Ctrl	Rad-1	Ctrl	Rad-1
Stiffness (N/mm)	410.90 ± 24.40	456.79 ± 59.36	441.56 ± 52.30	446.85 ± 89.77	547.95 ± 124.04	455.01 ± 123.46
Yield force (N)	80.25 ± 5.67	80.97 ± 8.17	81.84 ± 12.44	84.46 ± 5.87	98.69 ± 5.66	84.18 ± 15.29
Ultimate force (N)	124.02 ± 8.80	125.08 ± 6.15	115.70 ± 7.99	119.24 ± 9.29	134.92 ± 26.17	111.42 ± 32.70
Young's modulus (MPa)	3176.29 ± 566.17	3804.44 ± 335.58	3026.80 ± 558.42	3267.79 ± 564.21	3616.42 ± 1282.79	3273.04 ± 1379.14
Yield stress (MPa)	68.72 ± 14.10	74.65 ± 10.81	64.79 ± 13.53	69.57 ± 3.13	73.45 ± 8.22	67.27 ± 16.20
Ultimate stress (MPa)	105.67 ± 17.15	114.88 ± 6.16	91.18 ± 10.16	98.30 ± 7.54	102.42 ± 33.07	89.33 ± 30.49

Table 4.1: Test results, values are presented as mean ± standard deviation. No significant differences were found between the groups or between the times of euthanasia.

If the time aspect of the test is disregarded and all measurements of each group are gathered, the differences become much less distinct. Lumped comparisons of the measurements are presented in Figure 4.3 and Table 4.2. There were no significant differences measured between the two groups by this assessment due to high deviations. The lowest and second lowest P-values are related to yield force and

ultimate force, respectively, where the radiated group is somewhat weaker. This can to a lesser extent indicate a difference in some material properties of radiated and non-radiated bone. Although the slightly higher global stiffness in the control group conforms with the time-dependent results, high uncertainty prevents any conclusion. It is evident that the time aspect must be accounted for in the respective assessment due to certain physiological properties of rat femur. Despite some tendencies of reduced bone quality from radiation, high standard deviations and insignificant differences render the bending test inconclusive.

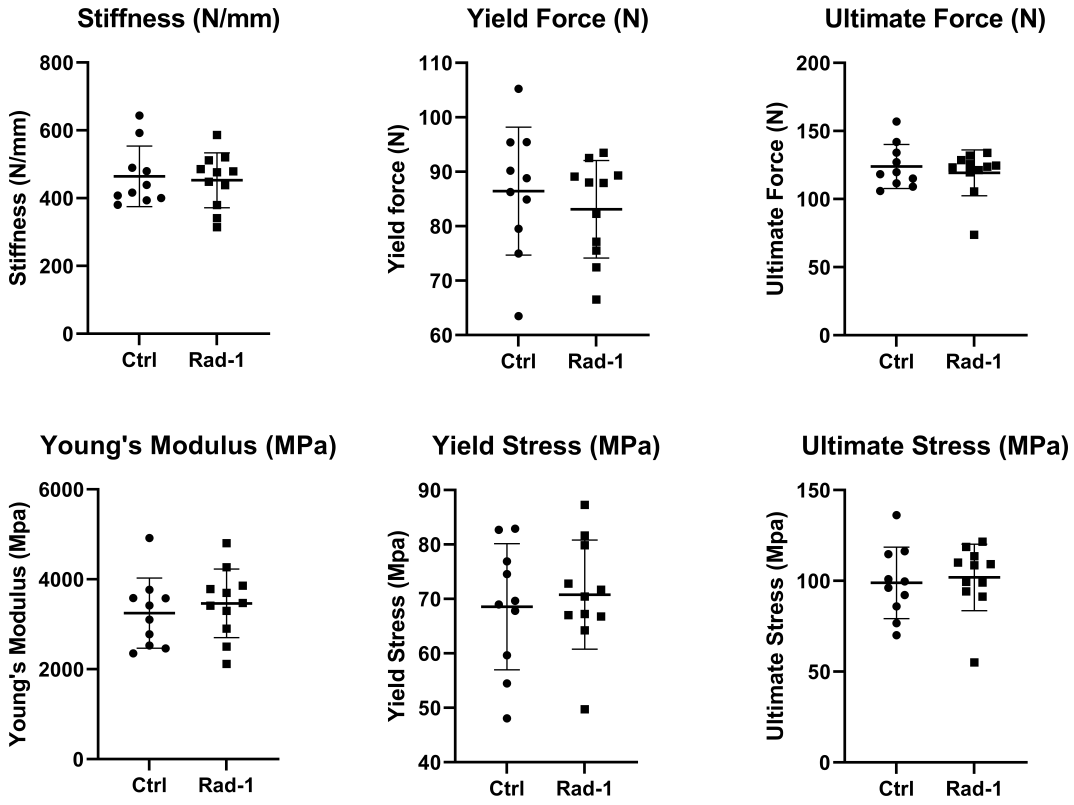

Figure 4.3: Global stiffness, yield force, ultimate force, Young's modulus, yield stress and ultimate stress of radiated (Rad-1) and non-radiated (Ctrl) femurs, plotted with all specimens in each group gathered. Values are presented as mean ± standard deviation.

	Ctrl	Rad-1	P-value
Global stiffness (N/m)	464.28 ± 89.31	452.69 ± 80.90	0.759
Yield force (N)	86.42 ± 11.75	83.11 ± 8.95	0.474
Ultimate force (N)	123.96 ± 16.15	119.23 ± 16.83	0.520
Young's modulus (MPa)	3248.53 ± 780.74	3464.37 ± 763.15	0.530
Yield stress (MPa)	68.57 ± 11.60	70.79 ± 10.04	0.643
Ultimate stress (MPa)	98.90 ± 19.72	101.88 ± 18.28	0.723

Table 4.2: Comparison of lumped test results. Values are presented as mean ± standard deviation.

The measurements of Young's modulus were lower than what is suggested in other literature (Ramezanzadehkoldeh and Skallerud 2017a; Schriefer et al. 2005; Cory et al. 2010). While an elasticity of 10–15 GPa would be expected, the lumped average was only 3.4 GPa in the present study. A further discussion on this discrepancy is presented in section 5.1, however, the low values might have posed a weakness to the comparison of Young's modulus between the radiated and non-radiated femurs. Although a wide range in these measurements should be expected, higher mean values could possibly yield more significant differences.

Yield stress was further analyzed. An average density was calculated by selecting a region in the middle of the lowermost part of the cortical cross section beneath the plunger (Fig. 4.4(b)) and employing the expression $\rho = 4.395 \times 10^{-4}$ GV (g/cm^3). Assuming tensile/compressive yielding and stress symmetry about the neutral axis, correlation between apparent density and measured yield stress was assessed. Data points for each femur is plotted in Figure 4.4(a). The results were compared to a relationship based on Cory et al. (2010), which yielded satisfactory results when employed by Ramezanzadehkoldeh and Skallerud (2017a). Although the densities are closely gathered, the respective yield stresses congregate around the relationship curve, suggesting that the quality of the yield stress measuring method was good.

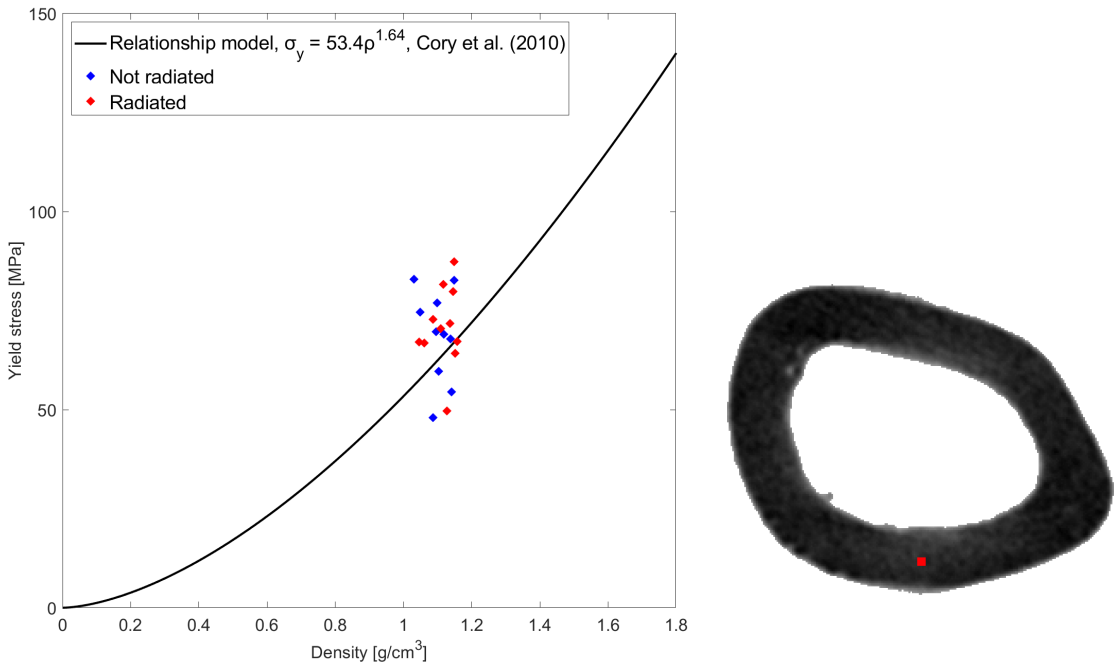

Figure 4.4: Correlation between density and yield stress: (a) comparison with the relationship model formulated by Cory et al. (2010), (b) example illustration of the region of interest analyzed (red square).

4.2 Experimental bending test of femur 25–48

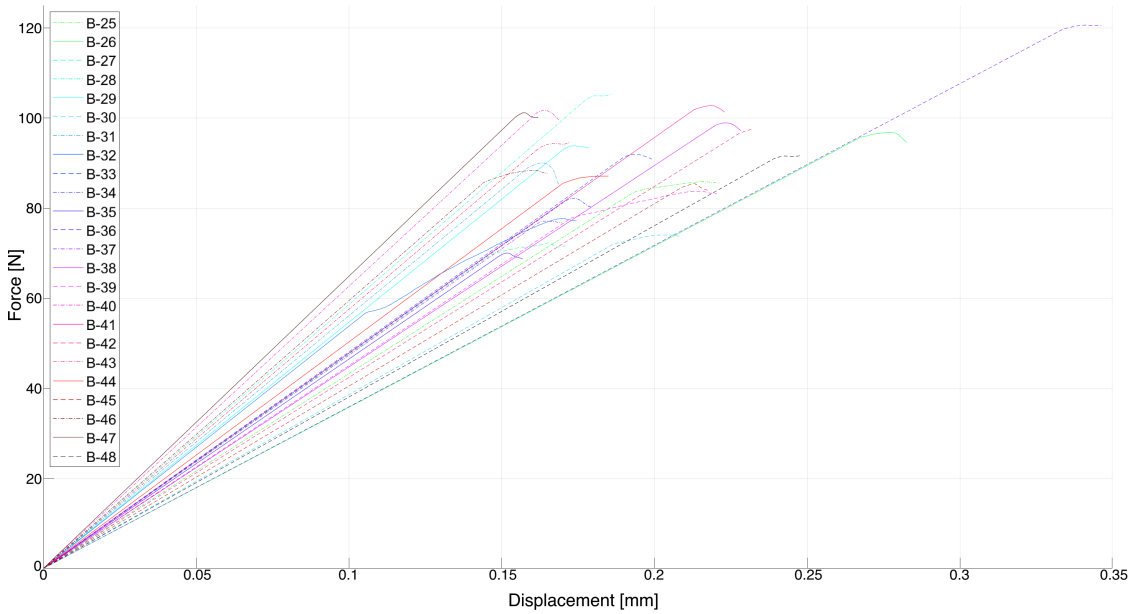

Figure 4.5: Linearized force-displacement plot of second test.

Linearized and cleaned force-displacements, similar to those presented in section 4.1, from the second TPBT of radiated (Rad-2) and radiated and exercised (RadEx) rat femurs are plotted in Figure 4.5. An initial interpretation of the plots shows an overall slightly higher stiffness and a narrower range than the first bending test. The highest measured yield forces are also somewhat higher, although this value is wider spread.

Since all rats from the second study were euthanized simultaneously, the time aspect was not accounted for in the respective comparisons. The same parameters as described previously were measured and compared. All comparisons and corresponding P-values are presented in Figure 4.6 and Table 4.3. Some indications of greater material quality in the exercise group are seen, as all quantity averages are of higher value. However, the maximum yield force, Young's modulus and yield stress were all seen in the radiated group. Minimum ultimate force and ultimate stress were also measured in the exercise group although some discrepancies were considered acceptable. Nevertheless, the high deviations in both groups inhibits any certain conclusion to be made from the second study as well. Although P-values for all comparisons were lower, none were low enough for the differences to be significant.

It must be noted that neither of the two *in vivo* animal studies discovered any significant differences in cortical bone, except for RadEx having a higher BMD than Rad-2 (P=0.0036, Mann Whitney U test). It would thus be unlikely for the TPBTs to show any tangible differences, since mechanical testing is more susceptible to geometrical variances and other sources of error. Regardless, some critically high deviations of the measurements suggest that three-point bending test (TPBT) might not be an admissible method of measuring the impact of radiation and exercise to cortical bone. Other testing methods, which can alleviate some of the geometrically

related errors, might however be more feasible. Additionally, other intrinsic bone properties might be better related to the physiological changes in bone caused by training and radiation. A good example is measurement of hardness and strain-rate sensitivity by nanoindentation. This technique is also not as susceptible to geometrical errors, and many more tests can be conducted on the same sample, which increases the test accuracy (Ramezanzadehkoldeh and Skallerud 2017b).

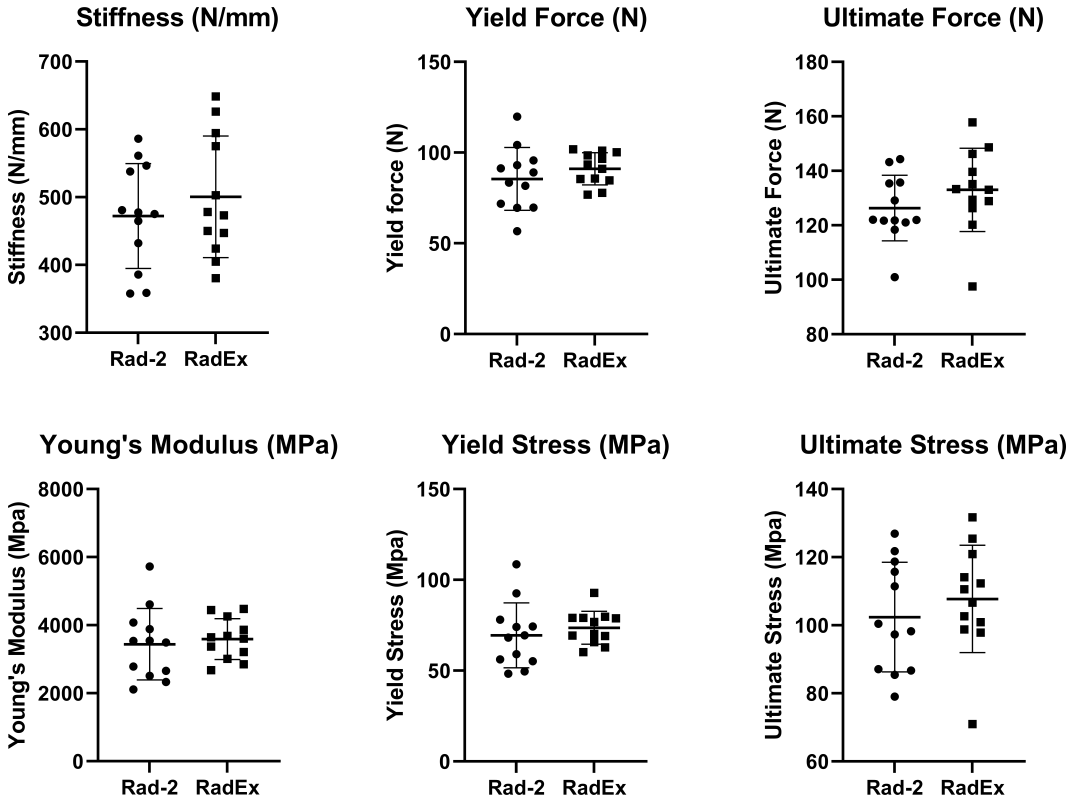

Figure 4.6: Global stiffness, yield force, ultimate force, Young's modulus, yield stress and ultimate stress of radiated (Rad-2) and radiated and exercised (RadEx) femurs. Values are presented as mean ± standard deviation.

	Rad-2	RadEx	P-value
Global stiffness (N/m)	472.06 ± 77.36	500.51 ± 89.53	0.414
Yield force (N)	85.49 ± 17.26	91.08 ± 8.90	0.330
Ultimate force (N)	126.31 ± 12.05	133.00 ± 15.32	0.247
Young's modulus (MPa)	3437.24 ± 1049.48	3591.10 ± 599.12	0.664
Yield stress (MPa)	69.47 ± 17.86	73.62 ± 9.11	0.481
Ultimate stress (MPa)	102.40 ± 16.13	107.72 ± 15.77	0.423

Table 4.3: Comparison of test results. Values are presented as mean ± standard deviation.

4.3 Virtual bending test of femur 1–23

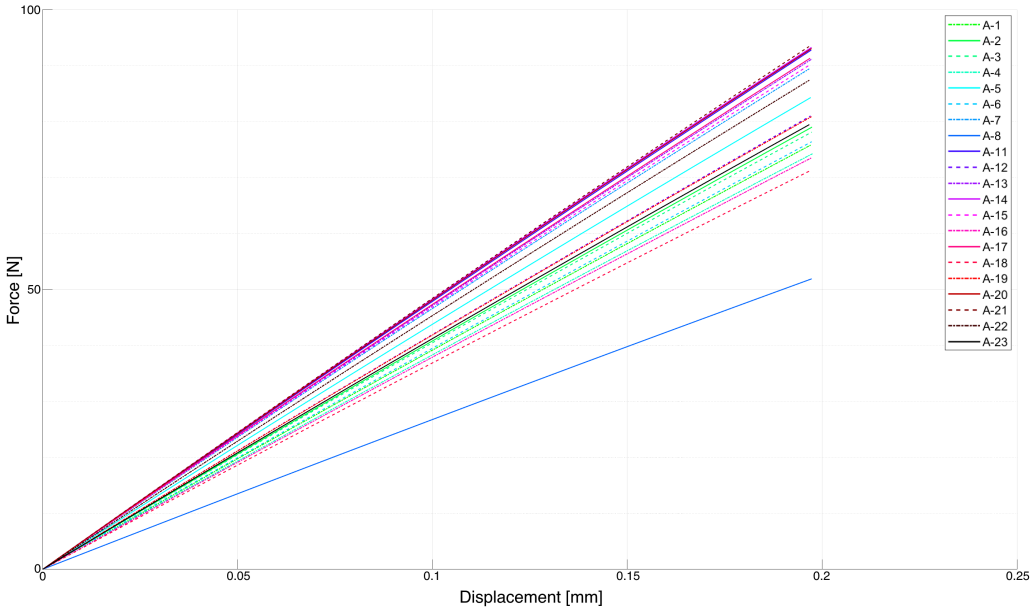

Figure 4.7: Force-displacement plot of first simulated test. Color coding corresponds with experimental force-displacement plot.

Resultant force-displacement plot of simulated TPBT of femur 1–23 is presented in Figure 4.7. Despite the 20 increments of displacement and accounting for large displacements, the reaction force is nearly perfectly linear throughout the load case. This was likely caused by the strict boundary conditions and no additional seating during the simulation. Femur 8 was excepted from the comparison. Its simulated reaction force differed greatly from the other specimens in a negative manner despite being the specimen with the highest stiffness and Young's modulus in the experimental test. An investigation of the density distribution of femur 8 revealed densities much lower than what natural genetic variation would suggest (Fig. 4.8). An error during µCT-scanning is likely to have caused this discrepancy.

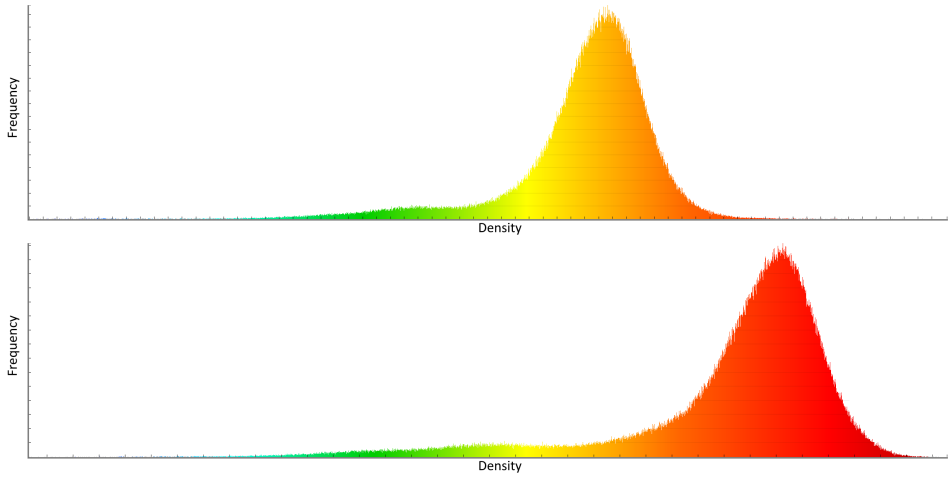

Figure 4.8: Density distribution of cortical sections, femur 8 (top) and 15 (bottom). Density distribution of femur 15 is close to the average of all femurs.

One incident of miscalibration during µCT image reconstruction, which resulted in a large portion of the study needed to be redone, caused an incorrect density distributions of the FE models, and thus invalid force-displacement results. Although the large deviation of femur 8 was the main instigator for this error to be discovered, a new reconstruction of the µCT images did not fix the errors related this specimen, suggesting that there still might be an error present in the CT image reconstruction process. Whether or not this error affected all of the models is difficult to say. The new reconstruction did cause a change of every simulated stiffness, some to a larger extent than others, but since new FE models and boundary conditions needed to be created and defined, other factors might partly have contributed to these changes as well. Other possible sources of error are presented and discussed in section 5.3.

Virtual global stiffness was calculated as mean slope of the force-displacement curve. When tested, no noteworthy sensitivity to using this method was found. The range of the curve slopes was not as wide for the simulated tests as for the experimental ones. Some possible weaknesses in the FE modeling and simulation might have caused this discrepancy, although the experimental testing setup could also have been a contributor. As discussed in the previous sections, some deviation should be expected due to geometric and physiological variations. However, standard deviations equal to 19.2 % and 17.9 % of mean global stiffness in the experimental control and radiated group, respectively, is slightly more than what should be expected.

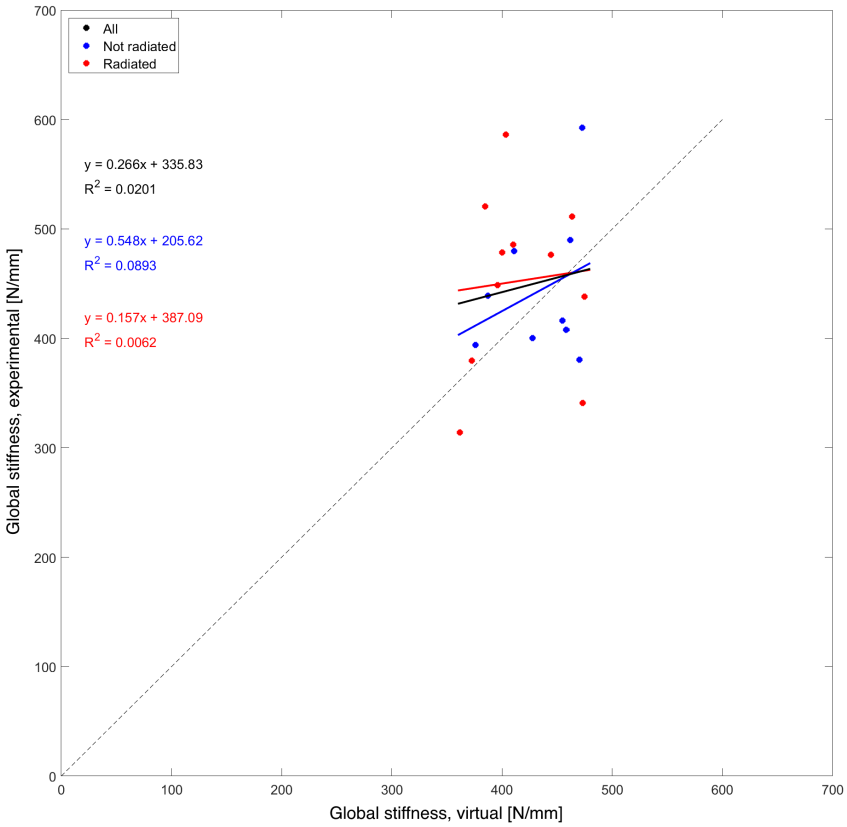

Figure 4.9: Global stiffness correlation. The regression curves indicate correlation between virtual and experimental stiffness for the control and radiated group as well as all specimens collectively. The higher range in experimental stiffness than virtual stiffness is visualized by the vertical span being more stretched than the horizontal span.

Figure 4.9 shows a correlation plot of virtual stiffness versus experimental stiffness. Although the comparisons congregate around the 1:1 line, R-squared is only 0.02. A coefficient of determination this close to zero denotes no correlation between experimental and virtual stiffness. For cases of perfect correlation, R-squared is equal to 1. Ramezanzadehkoldeh and Skallerud (2017a) managed to obtain a stronger correlation of global stiffness with resulting regression curve expressed as $y = 1.0304x + 4.1319$ and $R^2 = 0.828$, further indicating the presence of one or several detrimental errors in this study.

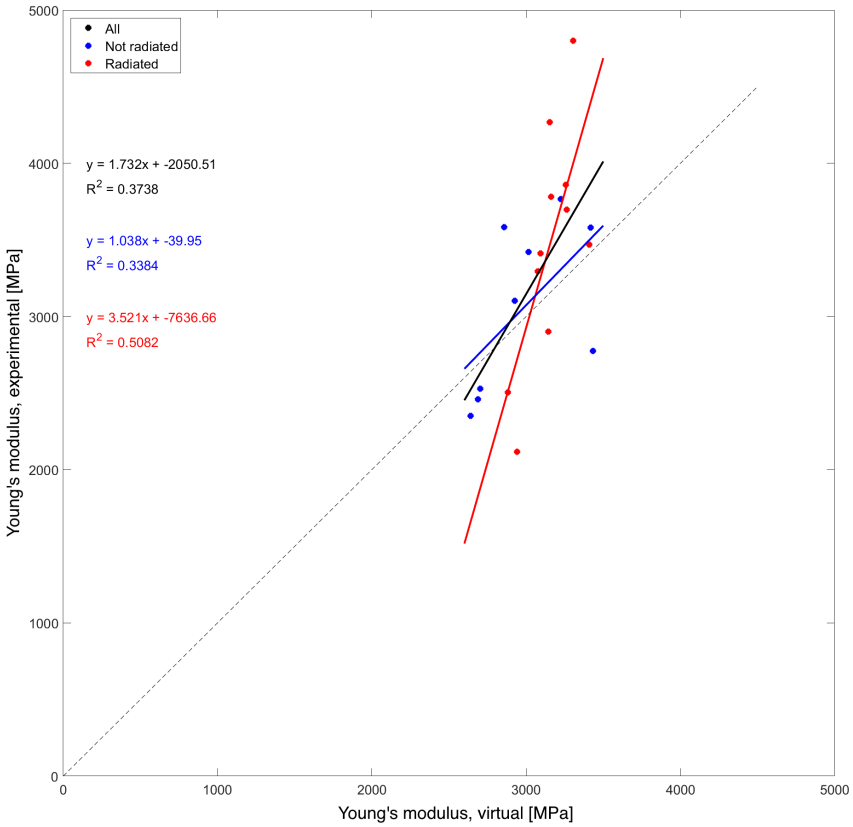

Figure 4.10: Young's modulus correlation.

Young's modulus of virtual bending test was calculated with the same Timoshenko formula as the experimental test (Eq. (3.6)). The same µCT-measurements of I_x and A were utilized. Resulting correlation plot is presented in Figure 4.10. Here as well, the difference in measurement range is noted, as the experimental test results are more spread than the virtual. The control group correlation curve fitted very well, with a slope of 1.038 and an intercept value of only -40 MPa. However, the coefficient of determination being no more than 0.34 is unfortunately not satisfactory. There are some data points which deviate strongly from the main group, causing a poor correlation of radiated femurs. Namely, femur 1 (4.3 vs. 3.2 GPa), 20 (2.1 vs. 2.9 GPa) and 23 (4.8 vs. 3.3 GPa). Removing these values yields a slightly better correlation of radiated bones ($y = 2.104x - 3284.26$), but R-squared is however not improved. The removal yields a better lumped correlation expression, $y = 1.298x - 779.08$, but resulting R-squared is nevertheless no more than 0.411. The exemption of the mentioned bones cannot be justified as no noteworthy discrepancies for these specimens were discovered in the density distributions or during the FE modeling.

The fact that virtually measured Young's modulus is excessively underestimated in two of the femurs and overestimated in the third one complicates the distinction of exactly what is causing the discrepancies. It rather indicates that several sources of error have been present, unless a single error has been affecting the study both ways.

Although perfectly elastic material properties were employed for the FE models, simulation stresses and potential yielding was of high interest to investigate. Maximum principal stresses (tensile stress) in a large posterior region under the loaded boundary nodes were recorded. The highest value at each increment was plotted against residual reaction force. Interpolation or extrapolation, whichever necessary, was employed to find the reaction force where the stress reached the same magnitude as the calculated yield stress of the corresponding specimen in the experimental test (Eq. (3.8)). It should be noted that although the Euler formula for yield stress is primarily not affected by Young's modulus, these calculations were to some extent, due to the bending force being simulated as an enforced displacement and not an applied force and the density distribution affecting how the loads are distributed. It is also noted that this method of predicting the yield stress essentially requires physical testing, since the real test results are utilized in the calculations. However, the correlation between the described calculations and experimental measurements should provide an overall quality check of the FEM simulations and help pointing out the source of error described above. Correlation plots of experimental versus virtual yield forces are presented in Figure 4.11. These curves fit well, with lumped correlation expression being $y = 0.843x + 6.02$ and $R^2 = 0.8606$.

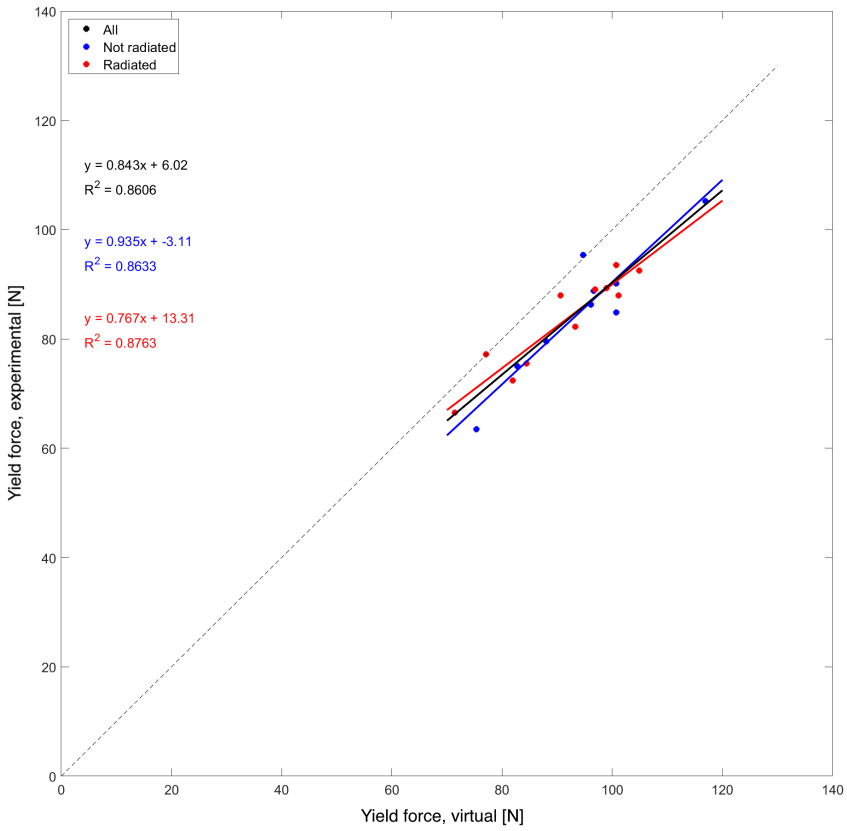

Figure 4.11: Yield force correlation.

Virtual TPBT overestimated the yield force by 10.8 %. This corresponds well with the strict boundary conditions employed instead of contact analysis. Other weaknesses related to FEM, such as element size, reduced indentation, not accounting for orthogonal material properties and possibly inaccurate defining of boundary nodes might also have contributed to an increased yield force, while ovalization and removal of epiphyseal segments are likely to have caused reduction. With the coefficient of determination being 0.86, the fitment is considered to be good, suggesting that the source of error could be somewhere in the mapping from gray value µCT images to density-dependent Young's modulus. A full table of all correlation curves is presented in Table 4.4.

		Stiffness (N/mm)	Young's modulus (MPa)	Yield force (N)
Ctrl	Experimental	444.36 ± 67.15	3063.29 ± 547.46	85.42 ± 11.99
	FEM	435.46 ± 36.60	2989.98 ± 306.84	94.65 ± 11.92
	Slope (R^2)	0.55 (0.09)	1.04 (0.34)	0.94 (0.86)
	Intercept	205.62	-39.95	-3.11
Rad-1	Experimental	452.69 ± 80.90	3464.37 ± 763.15	83.11 ± 8.95
	FEM	416.72 ± 40.58	3152.89 ± 154.52	91.03 ± 10.92
	Slope (R^2)	0.16 (0.01)	3.52 (0.51)	0.77 (0.88)
	Intercept	387.09	-7636.66	13.31
All	Experimental	448.94 ± 73.22	3283.88 ± 688.93	84.15 ± 10.20
	FEM	425.69 ± 39.01	3079.58 ± 243.15	92.66 ± 11.22
	Slope (R^2)	0.27 (0.02)	1.73 (0.37)	0.84 (0.86)
	Intercept	335.83	-2050.51	6.02

Table 4.4: Comparison and correlation curve expressions for global stiffness, Young's modulus and yield force. Note that femur 8 is removed from all measurements, resulting in different experimental values than presented in Table 4.1.

A further investigation was conducted to identify the source of the discrepancies described. All 21 FE models were given an homogeneous isotropic Young's modulus of 3.5 GPa, which is close to the lumped average of the experimental assessment. Although the assigned elasticity is lower than suggested values of cortical bone, the test would still yield correlation based on the quality for the FEM analysis. Step time increments were reduced from 20 to 10 in order to save time. This had been tested earlier and showed to have little to no effect on the resulting reaction force. Correlation of experimental and simulated stiffness and elasticity is plotted in Figure 4.12. An even narrower range of FEM stiffness was measured, as expected, since the variation in density was not accounted for. Yet, an even less satisfactory correlation was obtained ($R^2 = 0$), suggesting that the simulation method was suffering from some weaknesses. Interestingly, calculations of global elasticity by Timoshenko yielded on average 30 % lower Young's modulus than the assigned value. It is suggested that the Timoshenko formula is unfit for the present testing setup since Young's modulus is consistently underestimated. This is discussed further in subsection 5.2.2.

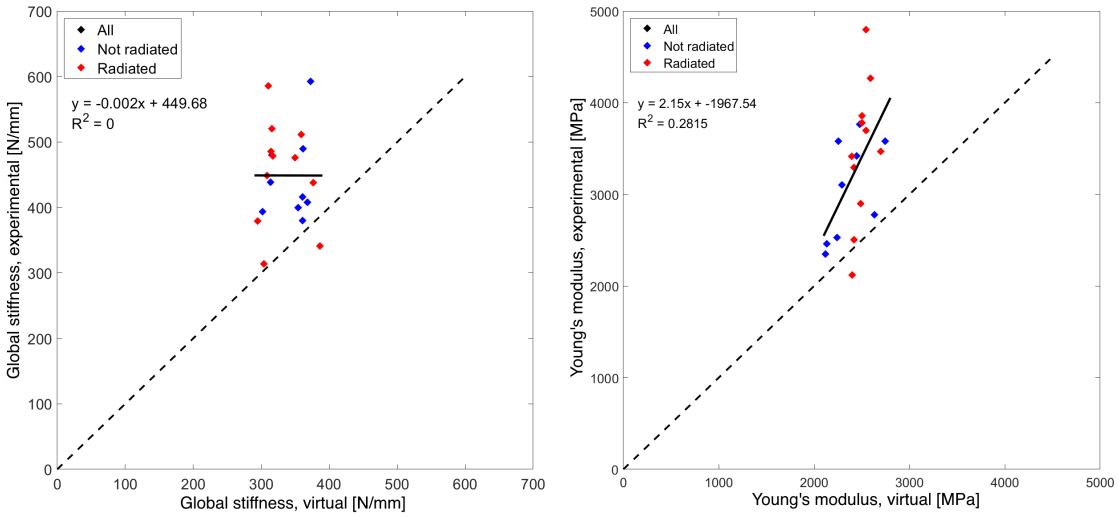

Figure 4.12: Stiffness and elasticity correlation, isotropic Young's modulus.

Final simulations were run, assigning each model the same Young's modulus as measured in the experiments. Number of increments were reduced further to 5. This yielded a lumped stiffness correlation of $y = 1.259x + 54.72$ and $R^2 = 0.8505$. Young's modulus correlation was $y = 1.17x + 581.69$, $R^2 = 0.952$. These results are indicative of the importance of accounting for density when assessing cortical bone. The strong correlations are supporting the previous suggestion of errors in the µCT density acquisition.

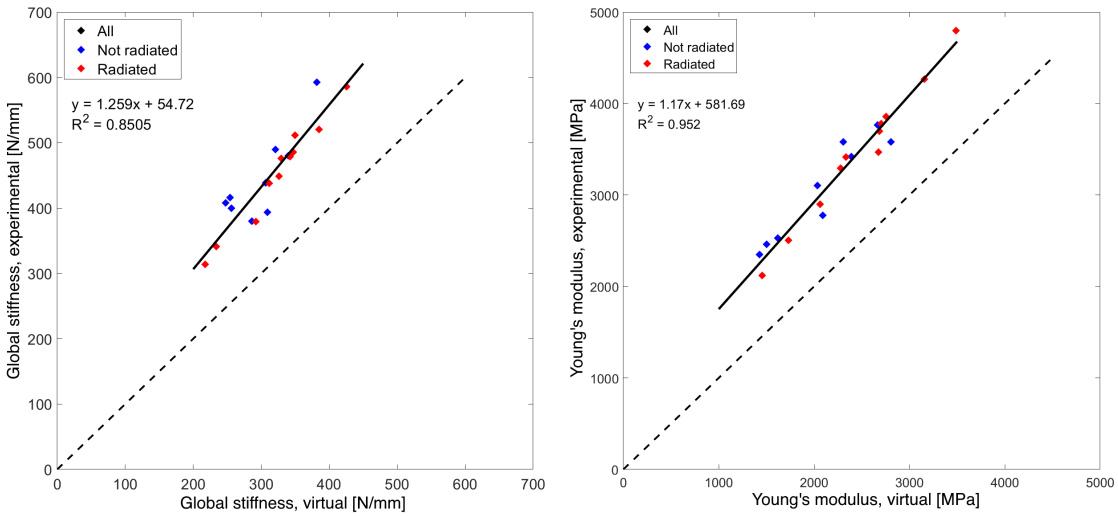

Figure 4.13: Stiffness and elasticity correlation, isotropic experimental Young's modulus.

On a final note, the virtual TPBT did also not show any significant difference between the radiated and non-radiated femurs. Although virtual testing is a promising method of testing certain bone material properties, the study results indicate that finite element TPBT analysis is unfit for evaluation of radiation impact on cortical bone.

4.4 Training and radiation simulation

The finalized training/radiation script is presented in Appendix H. Force parameters were defined as described in section 3.4, with accumulation exponent, $M = 4$ (Eq. (3.10)). The variables of Huiskes's model (Eq. (3.13)) were adjusted to correspond with the rats' life span. Low time step and remodeling rate coefficient values, $\Delta t \times B$, provided a steady density evolution. Reference stimulus was set to $k = 0.004$ (J/g) (Weinans et al. 1992). It is noted that the reference stimulus is largely related to the accumulated jumping height. For instance, if height was only calculated by mean value, k would have been too high for adaptive formation to occur. Initial tests were conducted to find a suitable balance between M and k. Radiation damage was defined as described in subsection 3.4.3, with $\alpha = 2$.

The model of femur 15 was set to follow the same program as every one of the 12 specimens in the RadEx group. The simulation started with one dose of radiation therapy, followed by 15 exercise sessions. Apparent densities were recorded before simulation and updated after every event.

Figure 4.14 displays the midspan cross section density evolution of femur 43. Top left image is the density before simulation, the same distribution as obtained by µCT. Typical values range between 1.35 and 1.5 g/cm^3, with some dense regions reaching 1.65 g/cm^3. Second image (top, middle) depicts the density immediately after radiation. The whole femur is affected equally, thus the uniform change of colors. Throughout the exercise events, adaptation occurred more strongly at the anteriormost region of the femur, suggesting that the contribution from quadriceps was somewhat overemphasized compared to the other muscle loads. Anterior densities reached maximum values, while the final posterior densities were slightly lower than initial. Femur 43 is depicted as an example. Other specimens saw similar adaptation behavior.

Figure 4.15 shows the how bending stiffness and yield force were affected by the simulation. Stiffness response development varied between ∼5 % increase and one minor decrease. Mean stiffness increased by 2.3 %. Since the Rad-2 group saw higher average stiffness than the Rad-1 group in the experimental tests, it is difficult to evaluate the accuracy of the simulated results.

Yield force was calculated in the same manner as described on page 54, using the yield stress of femur 15 as reference for every model. All models saw a distinct increase with a very low standard deviation. Average yield force increased by 4.7 %. This result emphasizes the previous suggestion that density does not directly affect this parameter, as mean apparent density in all models was slightly lower than first. The local distribution of density does however influence the yield force. When most of the gained bone mineral is located in the anterior region of the model, a higher force is needed to obtain the reference principal stress in the posterior region.

The density evolution in Figure 4.15 is measured as mean of all models' average density at each event. The curve slope is steepest right after radiation and flattens out towards the final exercise. This might indicate that the models are close

to reaching an equilibrium state between material strength and exerted loads. In this regard, some aspects of the training/radiation simulation show good fit with expected results, although the obtained densities were not optimally distributed.

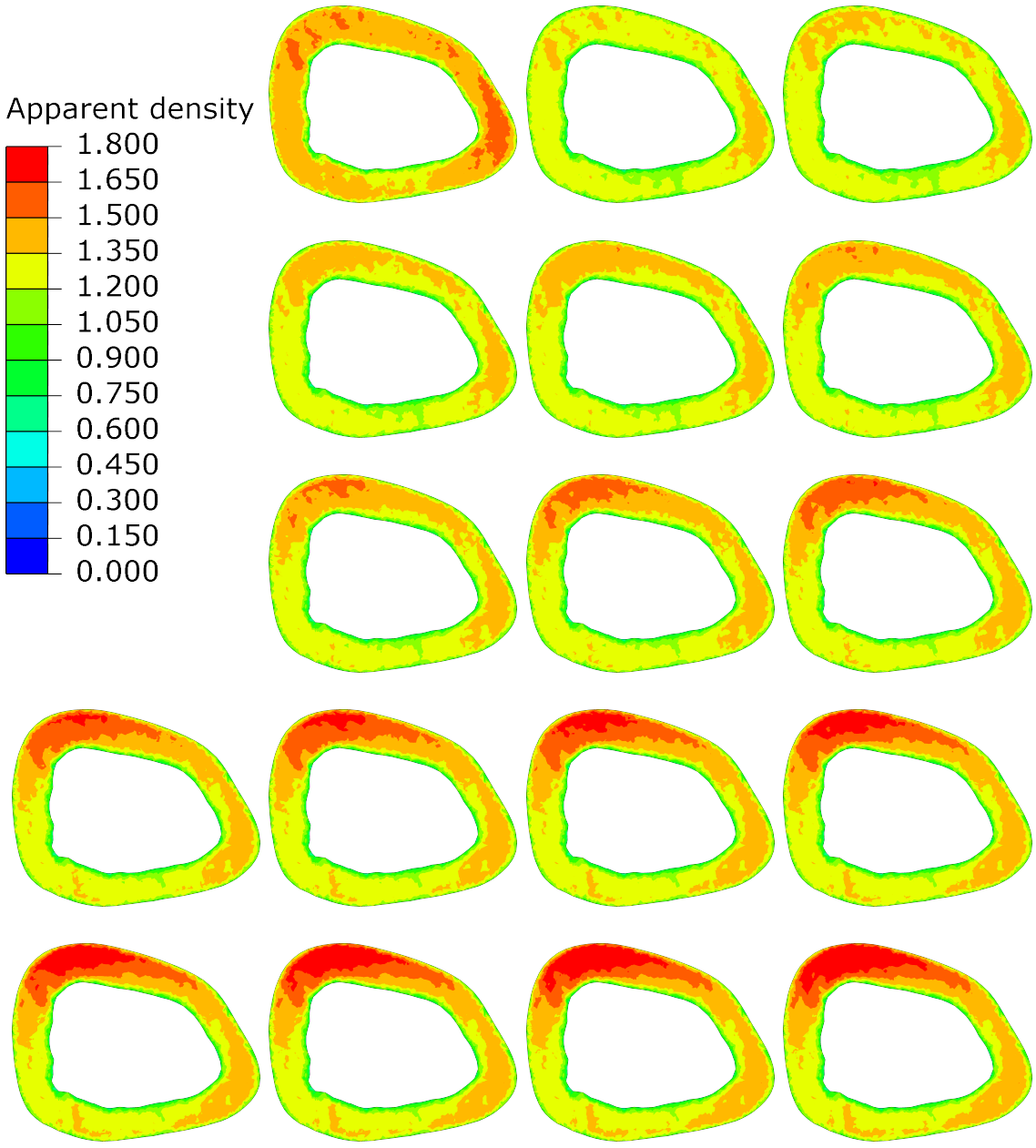

Figure 4.14: Density evolution of femur 43 at midspan. Top left image shows density distribution prior to simulation, bottom right shows resulting density after final exercise.

Femur 44 saw the largest increase in stiffness and average density. The corresponding rat was one of the specimens with the highest weight and jumping height combination during the last events. None of the heaviest or highest jumping models obtained stiffness above mean value, indicating that mass and height played an equally important role in the training simulation. Femur 38 saw a slight decrease in stiffness. This rat was the one with the lowest body mass in the RadEx group and jumping heights below average. Note that since all simulations were run with the same

model, a direct comparison with experimental results is not achievable. The correlation between body mass and jumping height and resulting stiffness and density does however contradict the comparative medicine animal study, which found no correlation between exercise parameters and *in vivo* measurements. This might suggest that the training/radiation simulation emphasizes these parameters more than training at all. Similar studies have suggested that exercising beyond a certain level does not yield significant differences to bone quality improvement (Umemura et al. 1997).

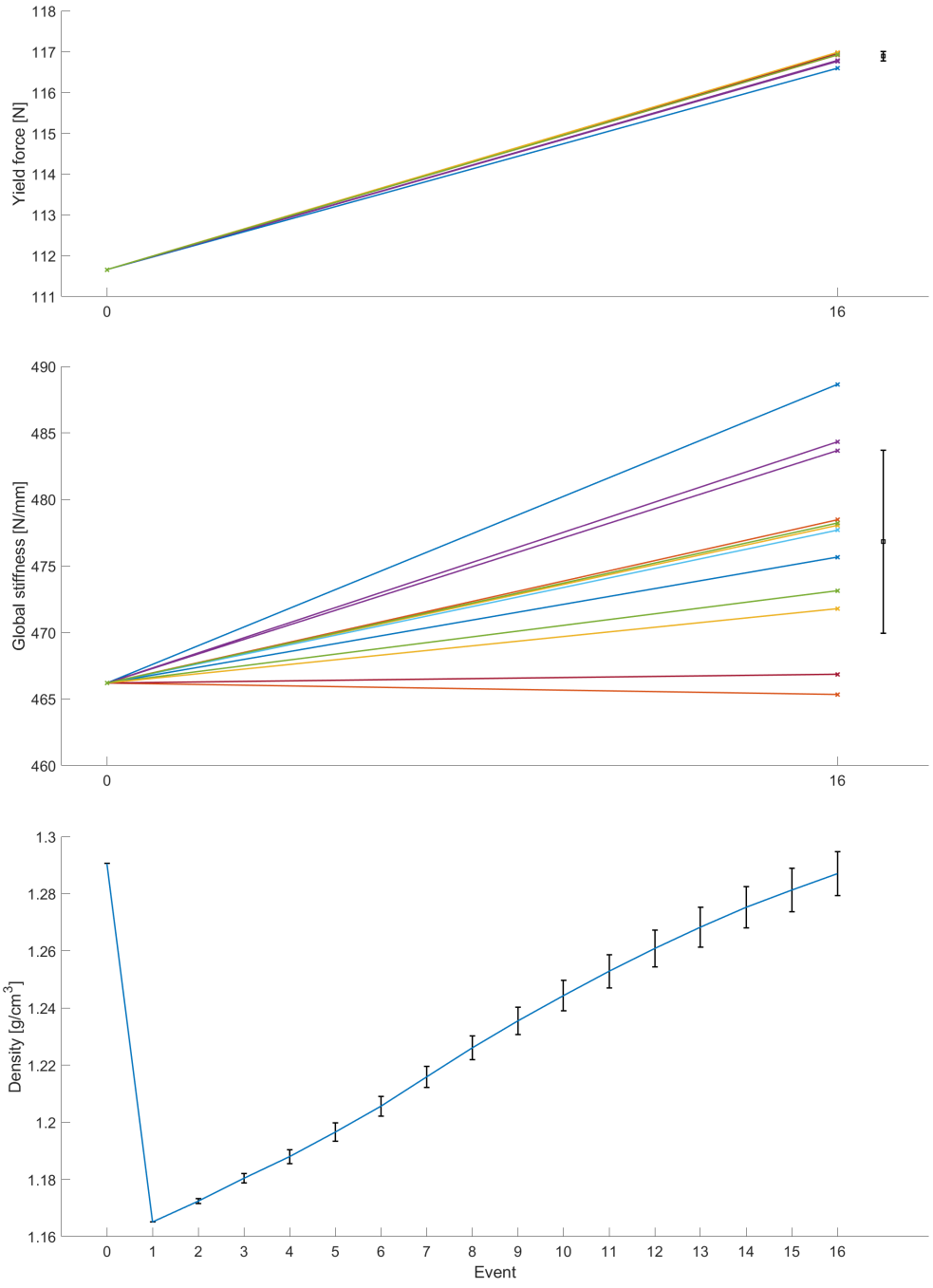

Figure 4.15: Simulation responses and average density evolution. Top: yield force; Middle: global stiffness; Bottom: Mean average density with standard deviation. Horizontal axis represent timestamps, where 0 denotes initiation and 16 is after final exercise.

5 | Discussion

5.1 Radiation and training effects on the mechanical performance of bone

One objective of the present study was to investigate the feasibility of mechanical testing as a means to evaluate the effects of radiation and training on material and mechanical properties of cortical bone. No significant results were obtained from either of the two tests conducted, suggesting that the employed testing method is unfit. It is well documented that physiological alterations caused by radiation and exercise are more present in the trabecular regions of the femoral epiphyses than in the diaphysis (Mustafy et al. 2018; Mosti et al. 2016). Mechanical testing of trabecular bone would have required other testing methods than TPBT. For instance, compressive testing of the femur head or a section of the proximal epiphysis could perhaps be a viable option. Also, the inaccuracies of bending test caused by geometrical irregularities has proven to pose a significant weakness to the study. Different implementations of TPBT and other seating orientations have been utilized in similar studies on rat femurs (Arias-Moreno et al. 2020), but large measurement variance has nevertheless presented challenges. Schriefer et al. (2005) found in their study that the radius bone was preferred to the femur for mechanical bending test because of advantageous geometrical properties and low variability. It is possible that lower variability, or an increased number of specimens, would have yielded more significant results when comparing both global and intrinsic properties in the present study.

The *in vivo* animal study conducted by the Comparative Medicine Core facility did also not find any significant differences in cortical properties between the Rad-1 and Ctrl groups. Substantial differences were however observed in bone trabecular thickness number and separation and bone volume fraction in the assessment of trabecular bone. The second study did not show any distinction in trabecular or cortical bone between Rad-2 and RadEx, except for higher cortical BMD in RadEx than Rad-2. This suggests that no considerable difference in either study should have been expected in either of the mechanical tests. Due to a generally lower possibility of measurement error, an *in vivo* study is more likely to yield tangible results than mechanical bending tests. Thus, if any considerable results were to be obtained in the present study, they would most likely be caused by other confounders.

The radiation-induced reduction of stiffness could to some degree seem contradictory to the diminishing of collagen phase, which governs bone ductility. It is however important to distinguish between ductility and elasticity (Young's modulus). While ductility describes the susceptibility to plastic deformation, elasticity is the measurement of force response in the elastic region. Soft collagen contributes very little to bone elasticity, compared to apatite mineral. Global stiffness response should thus not decline immediately after radiation, but later as osteoblast proliferation is reduced. This conforms well with the observations in the first study. Bartlow et al. (2018) measured a reduced fracture toughness right after bone radiation. This is a property which is very much dependent on ductility. A possible assessment of collagen deterioration in the present study could have been to measure the total work from first yield to breaking. Work (Nmm) is measured as the area under the force-displacement curve. Since some initial seating occurred during TPBT, the work until first yield would have to be excluded, resulting in a measurement of the energy dissipated during plastic deformation. Additionally, to alleviate any contribution from the mineral phase, one could consider only the force-displacement area above yielding force (Fig. 5.1). This measurement would be related only to the specimen toughness and susceptibility to strain governed by the collagen phase. Total work (elastic + plastic) for each specimen was calculated (see Appendices B and D), but further assessment was not conducted.

As mentioned earlier, nanoindentation testing could have been an interesting method of mechanical assessment. Such a study would still mainly consider cortical bone, but there are some noteworthy advantages over a bending test. Several tests could be conducted on the same specimen, minimizing the risk of measurement error. Geometrical variations would also have been alleviated, resulting in fewer possible confounders. Indentation does also allow for investigation of other material properties, such as hardness and strain rate sensitivity. These are indices which are likely to be affected by radiation since they depend on several physiological properties.

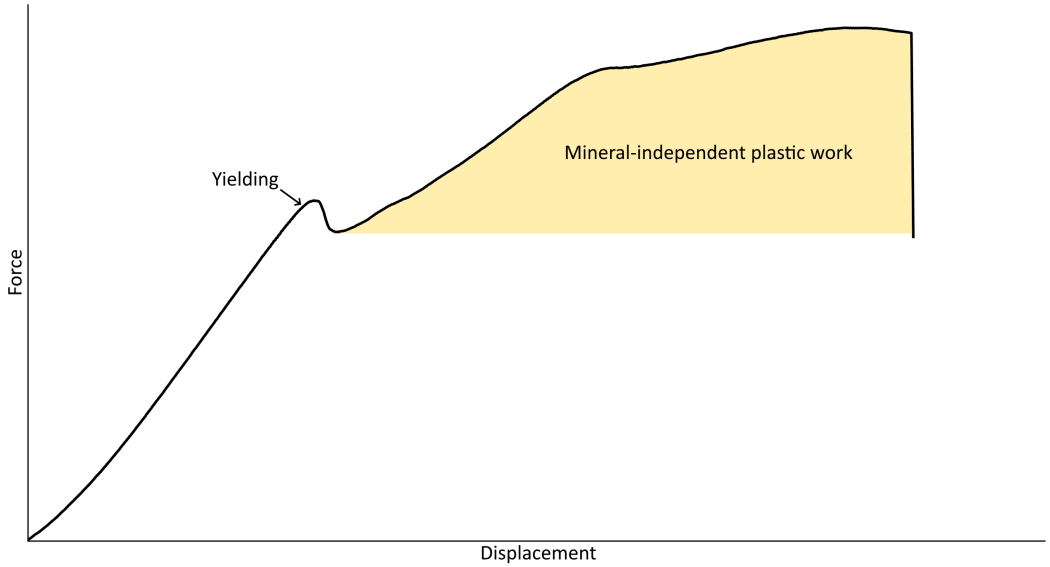

Figure 5.1: Example illustration of mineral-independent plastic work

5.2 Evaluation of the experimental bending test

The complex and irregular geometry and anisotropic material of femur gives rise to several challenges when assessing mechanical properties, both when comparing experimental test results and when virtually recreating the same test. The following subsections present possible sources or error related to the test setup, some of which are affecting the experimental testing only, while others might have caused discrepancies in the FE analysis as well.

5.2.1 Seating orientation

One important possible source of error is how the specimens were seated during TPBT. It is difficult to define a common global axis system for all specimens to conform to, and unfortunate seating alignment might have caused specimens to behave weaker or stronger than expected. Figure 5.2 illustrates how femur 1 was oriented differently about its longitudinal axis between experimental and virtual TPBT. The virtual specimen orientation is also representative of how the 2$^{\text{nd}}$ moment of area, I_x, was calculated. An orientation offset of 20° causes a 10 % reduction of I_x (Fig. 5.3). Consequently, the experimental measurement of Young's modulus (Eq. (3.6)) was underestimated. Additionally, measurements of yield stress and ultimate stress (Eq. (3.8)) were overestimated since the distance from the neutral axis to the farthest voxel were actually less than measured. When calculating the geometric properties, a single cross section image of each specimen was utilized, and the entire femur was considered to have a uniform geometry for the entire diaphysis. It is thus difficult to estimate the magnitude of the error caused by longitudinal rotation. Cross section underneath the plunger of all rats from the first and second tests are found in Appendix A. It is evident that some cross sections are prone to rotation-induced error due to their oval shape. The error might also have caused both overestimation and underestimation of geometric measurements, since the exact orientation of test seating versus CT images was not controlled. It was made sure that all femurs were seated as equally as possible. However, deviations in image orientation were not accounted for. The discrepancy in femur 1 makes for an 8.3 % underestimation of Young's modulus. It is however considered unlikely that all specimens were affected this severely. Nevertheless, an elasticity increase from 4.3 to 4.7 GPa is still not enough to match the values suggested in literature.

Since the longitudinal axis can be difficult to recognize in experimental testing, specimens might also not be perfectly aligned between the two supports. This means that the **z**-axis orientation about the **y**-axis is deviating from the axis system of the plunger and supports. The bending axis would thus be skewed, and the specimen would behave stiffer and stronger than expected. Images were taken of every specimen from the same angle as in Figure 5.2(a) to ensure a uniform orientation of the **z**-axis. However, some deviation is possible, and correspondence between experimental and simulated orientation was not controlled in detail. This is although unlikely to be a critical source of error.

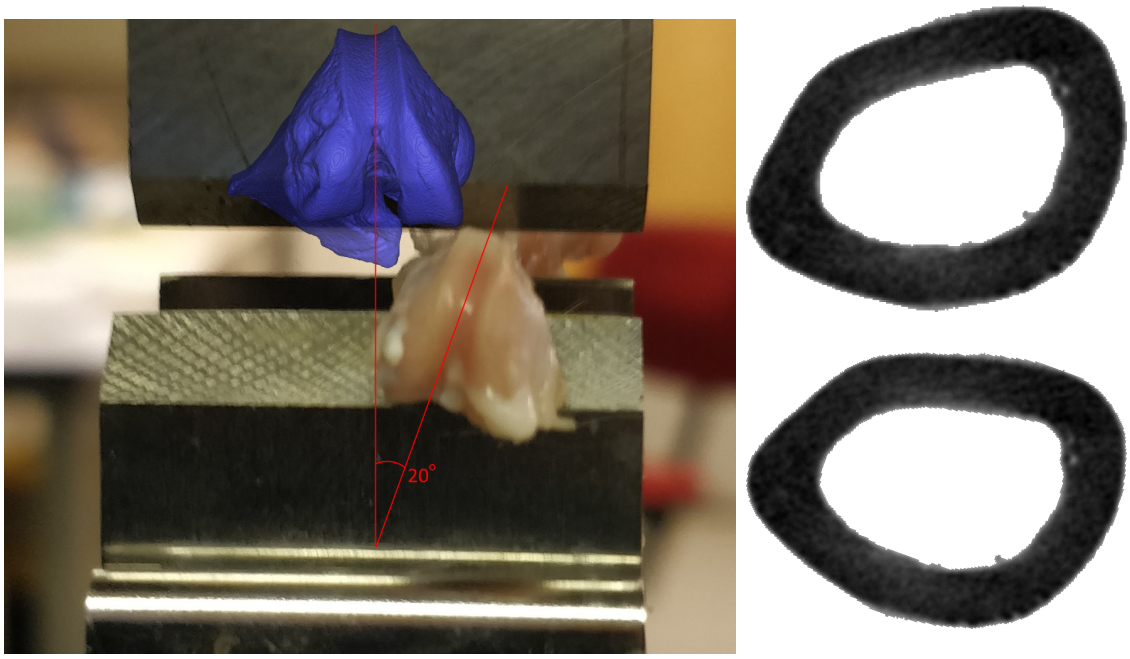

(a) (b)

Figure 5.2: Experimental TPBT seating orientation of femur 1, viewed in transverse plane from inferior towards superior region: (a) overlay of experimental and virtual (blue) TPBT. Virtual orientation equals orientation of µCT images, (b) cross section underneath plunger: not rotated (top, image orientation) and rotated 20° (bottom, experimental orientation).

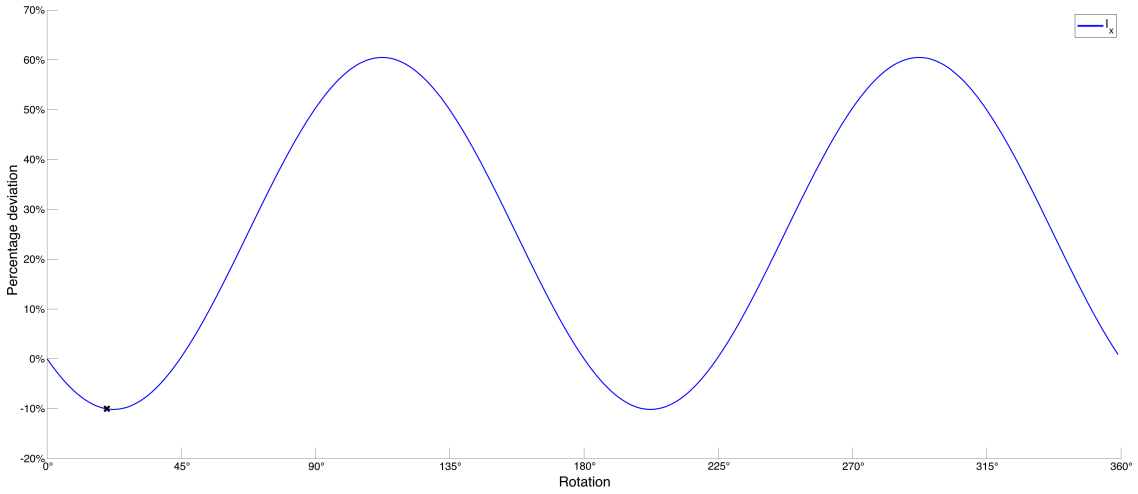

Figure 5.3: Percentage deviation of 2nd moment of area (about horizontal **x**-axis) due to rotation during seating. Horizontal plot x-axis represent clockwise rotation when viewed in same orientation as in Figure 5.2. Zero rotation equals the orientation of the µCT image, and deviation is calculated with µCT image as original orientation.

Finally, it was observed that some µCT images were misaligned in a way so that the longitudinal **z**-axis was angled about the horizontal **x**-axis. This would not affect the global response values of each specimen, but the calculation of intrinsic measurements. Figure 5.4 illustrates how the cross section image of a rod is elongated due to such a rotation, resulting in overestimation of area, 2nd moment of area and distance from the neutral axis to the farthest fiber. Consequently, Young's modulus

is underestimated while yield stress and ultimate stress is overestimated. Femur 18 and 20 are examples of specimens suffering from the described misalignment. Their measured elasticities were 27.7 % and 38.9 % lower than the average of the radiated group, respectively, suggesting that this error might have been an important contributor to discrepancies of Young's modulus.

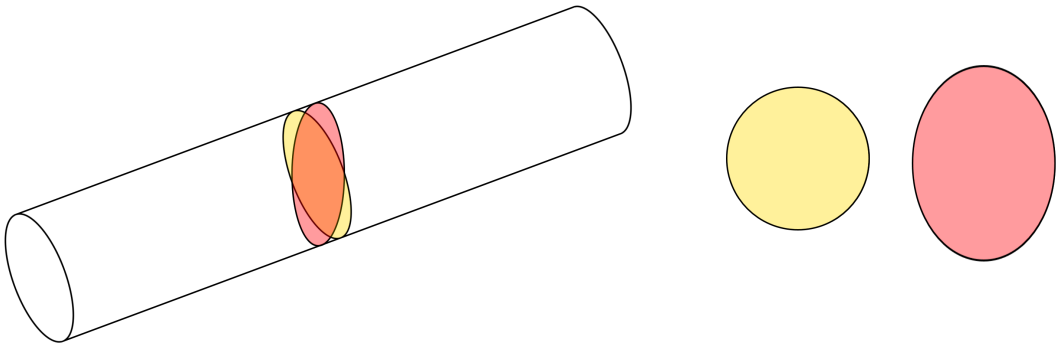

Figure 5.4: Cross section of rod. Actual cross section (yellow) is perfectly circular. The observed cross section (red) is elongated due to µCT alignment, resulting in a larger surface area and increased 2nd moment of area.

It is possible that the three described errors related to geometric measurements have been cancelling each other out in some specimens, while other specimens have obtained one large accumulated error. It was considered to realign all CT images to conform to the experimental orientation. However, these deviations were observed at a later point during the study, and a new reconstruction was considered as too time consuming. Additionally, a realignment would have required new images for image to density conversion. It is uncertain how this procedure would have affected the image bit levels and whether resulting voxel densities would be correct.

The visual estimation of plunger and support contact areas is another possible source of error. Although the diaphyseal cross sections did not vary much close to the midspan, the demonstrated importance of I_x and other geometric properties implies that this procedure might have been harmful to the calculation accuracy. A possible solution to this could, for instance, be to measure average geometric properties over the entire length of the diaphysis. Although this would not alleviate the challenges related to orientation, it would overcome some of the problems regarding irregular geometry. Another solution could be to implement expressions for area and 2nd moment of area, as functions of position along the specimen, into the Timoshenko formula. This is however a tedious task, undermining the feasibility of TPBT. Since cortical bone can be considered as a composite material, it could also be considered to account for density and measure the flexural rigidity, $EI_x = \sum_{voxels} E_{i,voxel} \left(y_i^2 A_{i,voxel} + \int_{voxel\ area,i} y_{local,i}^2 dA \right)$. This would however require the Young's modulus-density relationship to be already well defined, and thus alleviate the need for measuring specimen elasticity in the first place.

5.2.2 Aspect ratio

The low measurements of Young's modulus during the experimental tests called for more examination of relevant literature. Schriefer et al. (2005) favored the radius bone for bending tests on rat bones, partly because of its high aspect ratio. They did an investigation on elasticity prediction for a solid cylinder with $E = 19.1$ GPa and varying aspect ratio and found that when ratio dropped below 8.5, calculated Young's modulus was underestimated (Fig. 5.5(a)), despite employing Timoshenko beam theory. Van Lenthe et al. (2008) conducted similar TPBTs as the present study on mouse femurs with different support spans. They predicted the Young's modulus using Euler beam theory, but their findings are nevertheless noteworthy (Fig. 5.5(b)).

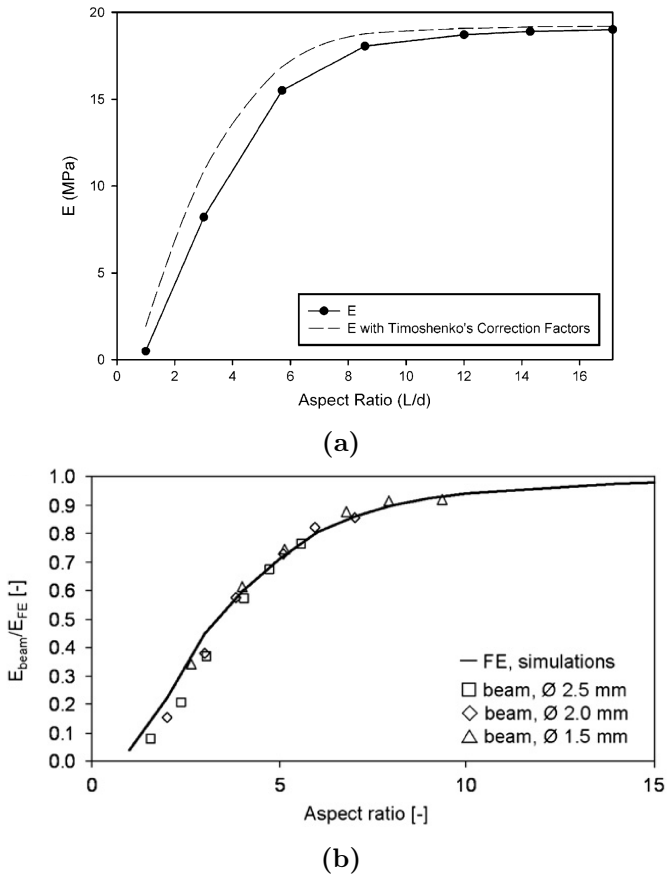

Figure 5.5: Influence of aspect ratio on prediction of Young's modulus: (a) adapted from Schriefer et al. (2005), (b) adapted from Van Lenthe et al. (2008).

The average aspect ratio of all specimens in this study was about 3.6. In the FE TPBT, where all models were given the same elastic properties, it was observed that calculations predicted 30 % lower Young's modulus than initially assigned (see section 4.3). While the findings by Van Lenthe et al. (2008) would suggest an even more severe underestimation for this aspect ratio, it is evident that both Euler and Timoshenko theory fails to accurately predict the Young's modulus when the aspect ratio is too low. It is further likely that low aspect ratio has been the most important, although not the only, reason for the low elasticity measurements in the present study.

5.2.3 Deformation irregularities

The displacement parameter in beam theory formulas describes the vertical translation of the neutral axis during bending. However, more often than not, experimental bending tests do not obtain this measurement accurately. In the tests conducted in this study, specimen displacement was recorded as the movement of the plunger. Therefore, if some form of deformation of the cross section occurred during bending, both global and intrinsic measurement would be imprecise. The total error related to deformation in TPBT is difficult to estimate, since both geometric and material variances are possible constituents.

One possible error, which is not detected by plunger displacement, is local indentation (Fig. 5.6(a)). Indentation can occur if the tested material stiffness and specimen aspect ratio are low or if there are sharp-edged contact points of plunger and supports. It is also a weakness related to testing of orthotropic materials, which cortical bone is. Broken femurs from the experimental TPBTs had a light discoloration around the site of fracture. This suggests that some form of local indentation, where water is flowing away from the specific region, occurred (Fig. 5.6(b)). Some indentation was observed in the FE analyses, which was accounted for. However, this might have caused some discrepancies between experimental and virtual TPBT, where the later would obtain a lower stiffness.

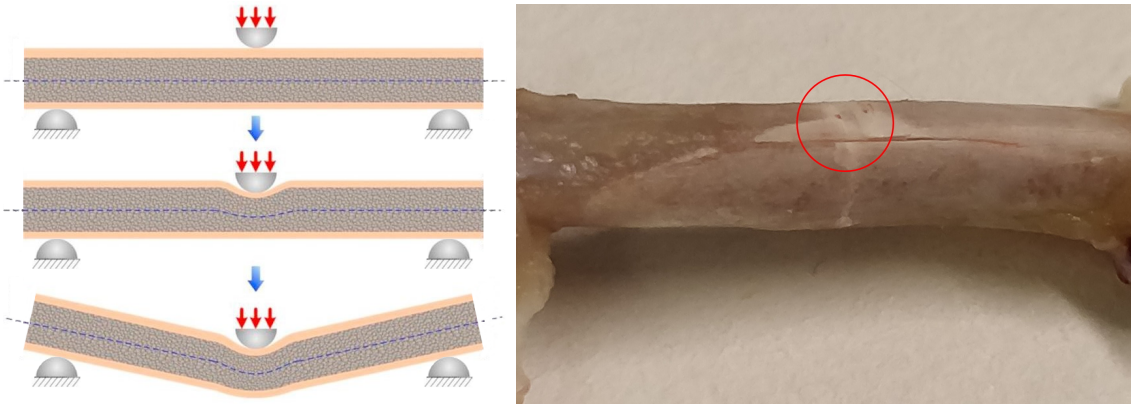

(a) **(b)**

Figure 5.6: Local indentation: (a) schematic illustration, adapted from Hao et al. (2018), (b) indentation of femur 30. Note the light color around where the plunger made contact.

Another source of error not accounted for by the experimental tests, is ring-type deformation, or ovalization (Fig. 5.7(a)). This weakness is more critical in test specimens with low cortical thickness compared to cross section radius, t/r. Schriefer et al. (2005) found that measured Young's modulus was within 95 % of expected value until t/r reached less than 33 %. Average thickness to radius ratio of the specimens in the present study was measured to 40 %, suggesting that ring deformation would not be a detrimental error. Note that this calculation was made over the posterior-most region, and radius was defined as half of the total vertical diameter. The ratio does depend significantly on where the measurement is made. FEM deformation of femur 15 is depicted in Figure 5.7(b). Although some ovalization is present, the error is considered to be small.

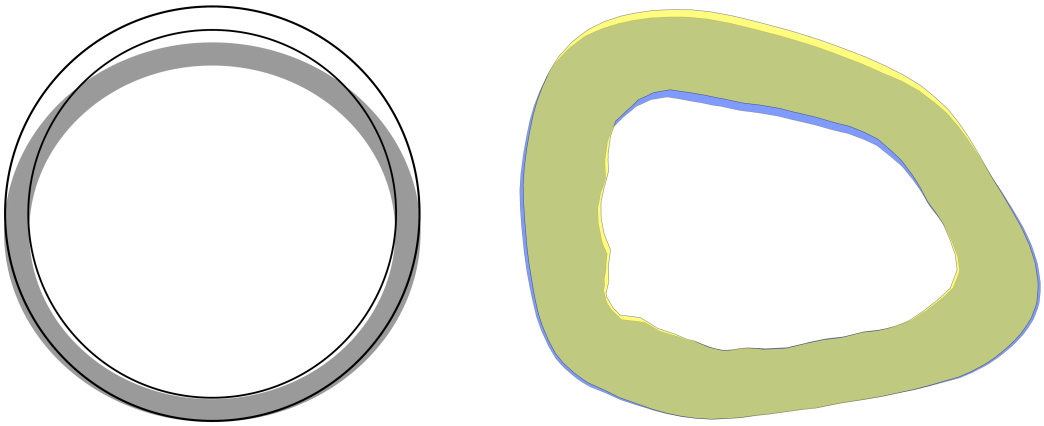

(a) **(b)**

Figure 5.7: Ring-type deformation: (a) schematic illustration of ovalization of a thin-walled cylindrical cross section, (b) FE ovalization of femur 15.

One solution to overcome the errors caused by local indentation and ring-type deformation, is to use digital image correlation (DIC). By recording the displacement of the neutral axis on camera, one would obtain a measurement of the correct parameter to use for beam theory. Additionally, by comparison of plunger and neutral axis translation, the total error could be calculated. DIC would however not alleviate posterior indentation where the supports make contact, but this could be accounted for by more thorough image processing. It was not considered to utilize DIC in the present study, but it is suggested for future studies.

After completing each bending test, the fracture surface was visually inspected. Most specimens obtained an even fracture surface, perpendicular to the cross section. However, some specimens did break in a more unfortunate manner (Fig. 5.8). Femur 9 and 10 were removed from the first test because of this. If there were longitudinal fractures present in the femurs prior to testing, the specimens would behave more like two disconnected beam members, resulting in lower stiffness and yield force. This might explain some of the significant deviations in the experimental measurement of global response values.

It was considered whether the onset of yielding was actually caused by shear stress instead of principal stresses. There is a reasonable likelihood for this to be the case, considering the low aspect ratio. In a theoretical bending beam, the maximum vertical shear stress occurs at the neutral axis and is zero at the cross section top and bottom. Therefore, in some of the specimens with longitudinal fracture surfaces, maximum and minimum principal stresses were obtained from a selection of elements located around the neutral axis. Average maximum shear stress was calculated, $\bar{\tau}_{max} = \frac{1}{2}(\bar{\sigma}_{max} - \bar{\sigma}_{min})$. Multiplying $\bar{\tau}_{max}$ with $\sqrt{3}$ yielded then the equivalent average von Mises stress for the selected region. Should this value exceed the principal stresses recorded in the posterior region, then shear yielding might have occurred before tensile or compressive yielding. Investigations yielded however $\sqrt{3}\bar{\tau}_{max}$ in the region of 20–30 MPa at the onset of yielding, which is significantly lower than the measured yield stresses (60–90 MPa). When assessing individual elements, alleviating the averaging of values, stresses around 40 MPa were obtained, still less than calculated yield stress. The findings indicate that, although the presence of shear

yielding during TPBT is possible, the longitudinal fractures did most likely occur at an earlier point of time. They might, for instance, have been caused by the snap freezing or during thawing when specimens were moved from freezer into tempered PBS solution.

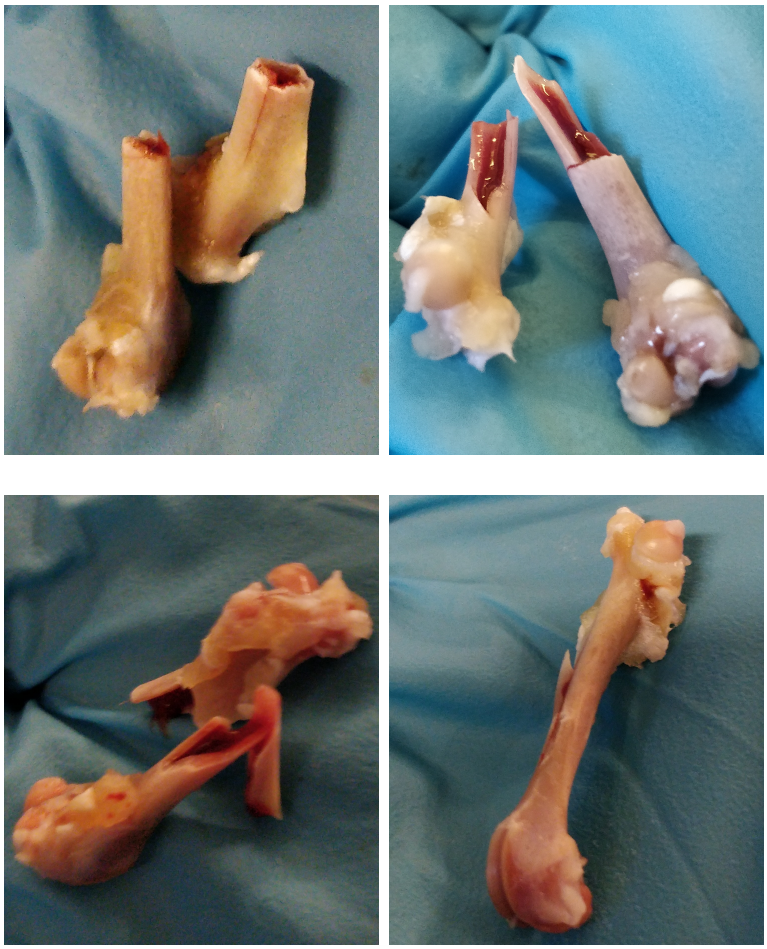

Figure 5.8: Different fracture surfaces of broken specimens.

Bone wetness during testing was discussed. It was initially considered to have little influence on stiffness, but some studies suggest otherwise (Lee et al. 2012). In the referenced study, dry conditions yielded measurements of Yong's modulus nearly twofold the values in wet conditions. The dry conditions are however not further described in the study. Quasistatic loading, where creep effect is present, is also not applicable to the present study, where the plunger moved 0.5 mm/min and loading rate was about 2.5–3.5 N/s. The specimens were however, prior to testing, stored in very wet, but yet similar, conditions as other studies (Schriefer et al. 2005; Ramezanzadehkoldeh and Skallerud 2017a; Bartlow et al. 2018), which should not have caused significant difference.

5.3 Evaluation of the virtual bending test

The previous section discussed various sources of error causing measurement discrepancies in the experimental tests. While some of the mentioned errors would affect both the experimental and virtual mechanical tests and their correlation, the following subsections present challenges related to the FE modeling alone.

5.3.1 FE model construction

The masks created by segmentation in Mimics where manually cleaned for easier meshing and to obtain a more uniform model. Thus, some trabecular bone was removed and slight corrections to geometry were made. Regarding surface smoothing of the endosteum, initial simulations were run with the entire cavity modeled by elements with Young's modulus close to zero. When FE procedure was changed to removing the cavity, no significant difference to resulting forces were observed, suggesting that strength contribution from diaphyseal trabeculae is negligible.

When discovering that some models had misaligned **z**-axis about **x**, it was investigated to what extent this was affecting the FE stiffness. An angled model will result in the bending force being exerted more in longitudinal direction, and thus increase the global stiffness. As previously mentioned, femur 18 and 20, which were noticeably tilted, obtained lower measurements of Young's modulus. However, their stiffness response did not differ from experimental results to any larger extent than the other specimens. This might be explained by the low aspect ratio, as more forces are exerting shear stress instead of bending stress. The specimens would thus not be as sensitive to **z**-axis orientation about **x** as first suspected. It has been confirmed that ring-type deformations were small, which would contradict a suggestion of large deformations in vertical direction. However, shear does not necessarily contribute to cross section deformation. As described above, realignment of the models was considered but not conducted.

It was initially desired for an even smaller mesh element size than what was utilized. The initial convergence tests were considered successful for a maximum edge length of 0.160 mm. However, since the force curves did not completely flatten, it might still be that important information was lost in the voxel reduction, and that the models were too stiff. The smallest possible tetrahedral edge length, representing an 18 µm hexahedral voxel without producing false information, would be ∼36 µm. Although such small elements would be infeasible with the current computer system, 40-60 µm quadratic elements would better ensure homogeneous mechanical properties within each voxel (Gross et al. 2012), and possibly yield more accurate results. Additionally, smaller elements would allow for finer assessment of the effects of local indentation and cross section deformation. It was experimented with smaller elements around the contact points, since these areas were of higher interest than the entire diaphysis. This would have generated more elements across the cortical thickness and more accurate calculation of apparent densities. However, it was eventually decided to employ a uniform mesh for the entire model. A finer mesh

would have required more system memory than what was available, resulting in simulations being unable to complete.

The density distribution histograms presented in subsection 3.2.4 did indicate that densities were accurately obtained. However, despite employing quadratic 10-node elements, it is noted that density and Young's modulus is averaged and discretized, by Gauss integration, for each element. This means that although true density distribution is well represented by nodal values, the accuracy of each element stiffness depends largely on the element size, unless Young's modulus of each element could be expressed linearly (or of any higher order) across its volume. Element shape quality is also a key measure in this regard and is a general weakness of tetrahedral element mesh. If a tetrahedra is badly shaped, stiffness might be over- or underestimated in local areas, despite correct nodal densities. Figure 5.9 depicts the arrangement of elements over the cross section of femur 1 at the midspan. The anterior (top in picture) cortical thickness of the model is ∼6.4 mm and represented by between 6 and 10 elements.

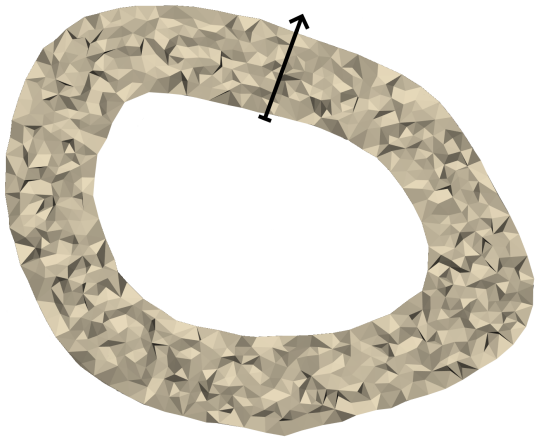

Figure 5.9: Element mesh at midspan. Densities along black line were obtained for the plot in Figure 5.10.

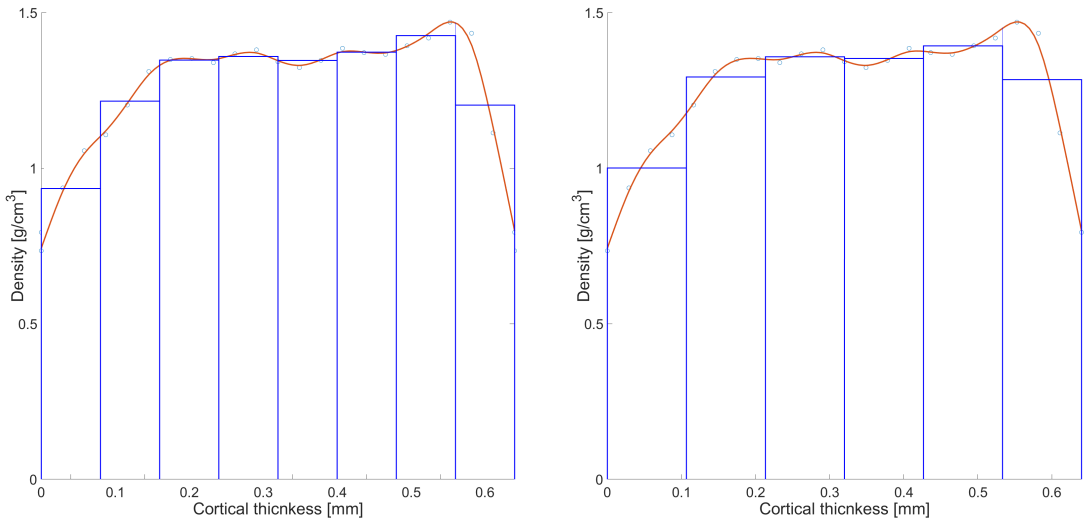

Figure 5.10: Element density representation for 8 and 6 elements over cortical thickness. Horizontal axes go from endosteum towards periosteum.

The plots in Figure 5.10 were created by obtaining the voxel densities across a section of the cortical wall (Fig. 5.9), and inputting the number of elements along that region. The element densities are not the exact same values as obtained by the model, but averaged representation, which give a reasonable illustration of the problem at hand. It is shown that for the specific area, the stiffness representation in the middle of the wall is good. However, the discrete element values fail to accurately reflect the variations at endosteum and periosteum. Outer surface stiffness is especially important, since this is where the TPBT plunger made contact. Here, the maximum voxel density is also not obtained in the model. The very importance of precise FE density representation has been demonstrated in this study. It is possible that too large element size did cause a critical weakness to the simulation accuracy, and thus the correlation between experimental and virtual TPBT. When giving each model the same global elasticity as calculated from experimental tests (Fig. 4.13), which did yield very good results, the model is more or less independent of element size since element stiffness is equal for the entire model.

5.3.2 Boundary conditions

In a full contact TPBT analysis, the plunger and supports are modeled with specific geometries and material properties. Instead of applying a force or enforcing a displacement, the plunger is assigned with a velocity, so the simulation resembles real behavior as closely as possible. Ramezanzadehkoldeh and Skallerud (2017a) applied only one extra boundary condition, by fixing one node, to prevent rotation about longitudinal axis. Contact analysis lets the model shift a certain amount to be properly seated. In contrast, the strict boundary conditions employed in the present study results in a stiffer reaction force since less movement is allowed. However, when simulating contact, the elements must be sufficiently small, to avoid that the master nodes penetrate the slave surface excessively. As described above, the element mesh was already as refined as possible for the utilized system setup.

The assignment of boundary elements was done manually by visual inspection, resulting in some deviations being unavoidable. Further, due to the triangular surface elements, creating a one-element wide boundary surface would sometimes cause the arrangement of selected elements to curve. Figure 5.11 displays the proximal and distal boundary conditions defined for the model of femur 1. It is shown that the marked lines are not perfectly aligned. With a maximum edge length of 0.16 mm, any element would however not deviate more than half this distance from true position. Local stresses caused by sharp element angles were considered acceptable, since the parameters were not measured close to the boundary regions.

It is also observed in Figure 5.11 that the proximal boundary surface is not completely flat, despite there being a large smooth surface towards the medial region (right in picture). This was done because the flat region was not completely aligned with the **xz**-plane. If boundary elements were chosen only at the smooth surface, the proximal and distal boundary would have been unaligned, thus causing potential rotation or other unwanted deformation during simulated TPBT. The uneven surfaces are likely to have caused a slightly stiffer model.

Defining boundary elements in 3-matic, and not in Abaqus, allowed for easy selection of only surface elements. One weakness to this was that, when translating a marked element to a node set, only the corner nodes of the element were selected. This caused the boundary conditions and enforced displacement not to be applied to every surface node within the boundary area (one node at each edge of a quadratic element). The implementation of stiff element properties to the respective elements (see subsection 3.2.5) should however help alleviate this problem.

How a model is defined, in terms of boundary conditions, is generally considered crucial to achieve a simulation that is representative of realistic behavior. It is suggested that an improved method is employed in similar future studies. The simulation setup in this study is likely to have caused discrepancies of about 10 % on average (Fig. 4.11). This is a noteworthy amount but is likely to only have caused a systematic overestimation of stiffness.

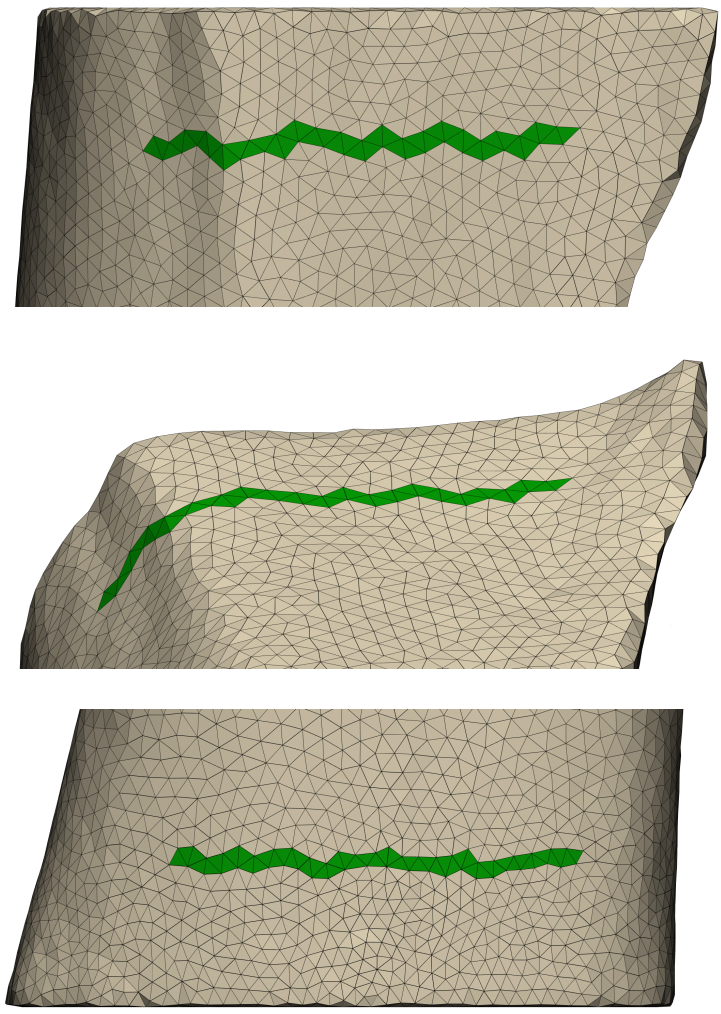

Figure 5.11: Boundary conditions employed for femur 1: proximal support (top and middle), distal support (bottom).

5.3.3 Material law

Mimics considers a linear relationship between image gray values and corresponding radiological densities, measured in Hounsfield units (Materialise NV 2020). This scale is more frequently utilized in similar clinical studies. Further, one can assume a linear relationship between Hounsfield units and apparent density (Yang et al. 2010). The relationship expression employed in the present study, $\rho = 4.395 \times 10^{-4}$, was defined by assuming 0 GV equal to zero density and the maximum cortical bone density being 1.8 g/cm^3 (Taddei et al. 2004). While the maximum density has been measured to slightly higher values (Adams et al. 2018), the linear relationships employed imply that the assumed density range would not cause any error to the correlation, other than shifting the intercept value.

A Young's modulus-apparent density law, $E = 2.19\rho^{2.33}$ was employed. Compared to the relationship model utilized by Ramezanzadehkoldeh and Skallerud (2017a), this expression predicts a slightly higher Young's modulus for densities $<$1.08 g/cm^3 and a lower Young's modulus for higher densities. Since only cortical bone was assessed, with average density of $\sim$1.5 g/cm^3, the models were predicted to be less stiff than the other study. However, since the material relationship is defined by a power law, the different stiffnesses calculated by each relationship are not proportionate to the densities. This means that, while one model with low average density might have seen a low percentage difference in stiffness, another model with very high average density would see much higher difference. Because of this, the relationship expression was not set until all simulations were run with both relationship models. A somewhat better correlation for the two stiffest specimens, whose virtual stiffnesses where underestimated considerably, was seen when employing the alternative relationship law. However, the overall correlation was not improved. The averaged expression was deduced from two empirical expressions: one for axial stiffness and the other for transverse stiffness (Wirtz et al. 2000). Although little vertical deformation was observed, it might be that the new formula yielded the best fit due to the low aspect ratio resulting in a significant amount of transverse loading.

It is noted that the material law employed has not been verified through empirical study. It is thus uncertain whether this model is gives an optimal representation of the stiffness-density relationship for the current test setup. Since the α and β parameters in Equation (3.2) affect the model characteristics differently, it is considered inaccurate to deduce new parameters by simply averaging them both.

The IDWI algorithm described in subsection 3.2.3 was created, not only to obtain Abaqus element properties from Mimics, but also to be able to apply simulated training/radiation adaptation to the nodes in a feasible manner. It is however possible to import element densities directly from Mimics to Abaqus, alleviating the IDWI model. The utilized algorithm was considered to work well (Fig. 3.9), but, as described above, this does not necessarily mean that each element was given the correct stiffness. A test was conducted to assess the simulation sensitivity to the IDWI model. Models of femur 2, 11 and 23 were reconstructed and simulated in virtual TPBT without using the algorithm. All simulation settings were otherwise equal. From before, femur 11 had seen an overestimation of stiffness, while femur

23 was significantly underestimated. The new simulations yielded 5.3, 10 and 5.2 % reduced stiffness for specimen 2, 11 and 23, respectively, compared to original virtual stiffness (Fig. 5.12).

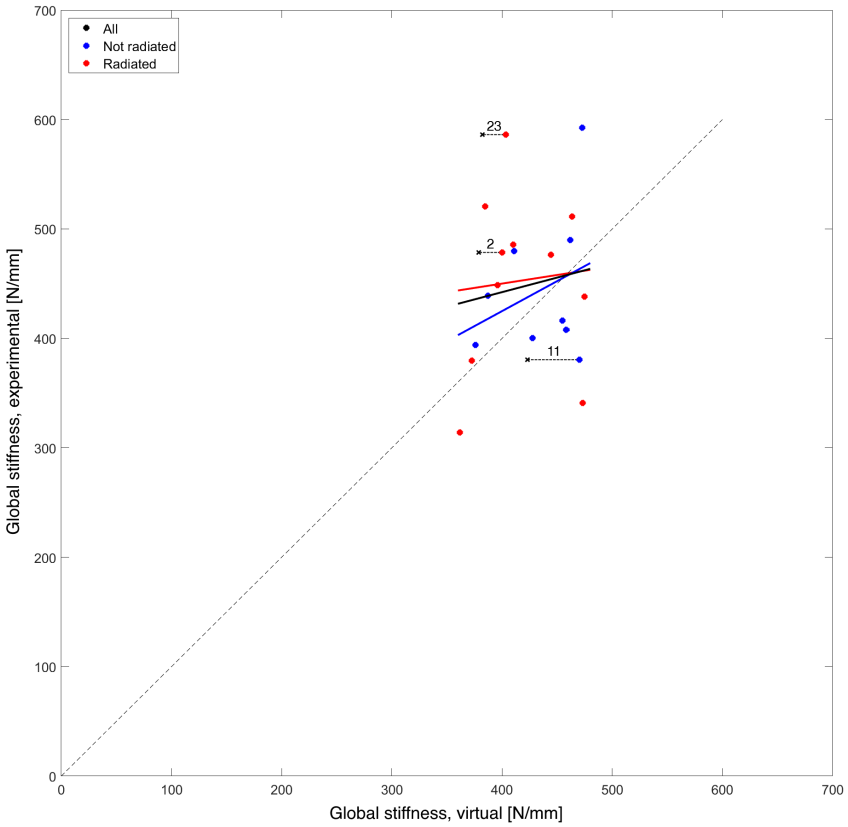

Figure 5.12: New stiffness calculations for femur 2, 11 and 23.

It is shown that the three assessed models saw an error of 5–10 % due to the IDWI algorithm. This is a noteworthy deviation, which might have contributed to the weak correlation. Additionally, the previously underestimated model of femur 11 was more corrected than the other models, indicating that the error might be dependent on average specimen density. However, alleviating the algorithm caused a systematic reduction of stiffness for all models, suggesting that the alternative method might have improved the correlation only slightly. One would have to employ this method for all specimens to know the magnitude of this error for certain.

Assigning plastic material properties to a FE model will drastically increase the number of demanding calculations, and thus the simulation time. It was initially experimented with various models with perfect plasticity, such as uniform yield stress for all elements and density-dependent yield stress (Cory et al. 2010). Unfortunately, these simulations were unable to complete every time with the utilized computer system. The ones which did complete, did not obtain satisfactory force-displacement curves (Figs. 3.10 and 3.12). It was also considered to employ cast iron plasticity properties, where different yield stress can be defined for tensile and compressive load. This would better conform with the asymmetric tensile and compressive yield stress of bone (Table 2.2). Simulations were however unstable and did not yield significantly different results from perfectly elastic material. If possible, an

interesting approach would be to investigate a model where cast iron plasticity and density-dependent yield stress is combined. Such a model could possibly present force-displacement curves similar to the experimental ones.

Cortical bone is orthotropic, with higher longitudinal stiffness than transverse. It is suggested that FE modeling, assuming isotropic material with parameters corresponding to the dominant loading direction, can yield good correlation with orthotropic material properties. (Ramezanzadehkoldeh and Skallerud 2017a; Schileo et al. 2007). However, the low aspect ratio in the present study makes it challenging to define the dominating load direction. Although the first onset of yielding is assumed to be caused by principal stress in longitudinal direction, various observations have suggested that other forms of yielding might have occurred, indicating that transverse loading has been equally as influential on the force response. Another measure to alleviate anisotropy is to employ a voxel and element size small enough to ensure isotropic element properties, as described in subsection 5.3.1. Gross et al. (2012) suggest that voxels of human cortical bone can be considered to be homogeneous for sizes $<$40 µm. Meanwhile, studies on µCT of rat bone have proposed voxel sizes of $<$20 µm to be desirable (Bouxsein et al. 2010). Larger voxel sizes might not only fail to accurately represent inhomogeneous material distribution, but also cause underestimation of BMD. While the present scan resolution of 18 µm can be considered as sufficient, the maximum element edge length of 160 µm does pose a critical weakness to the simulation quality.

It is possible that correcting for the various weaknesses described above would have yielded much better correlation than what was obtained. While the element size is considered as the main contributor, unaligned global axes and strict boundary conditions are also challenges which should be taken into account. It is assumed that the strong correlation obtained when assigning specimen-specific Young's modulus to each model was mainly related to the large element size. However, considering the faulty reconstruction of femur 8, there might also have been other CT-related errors present in the models as well. This is unfortunately not possible to evaluate without performing FE simulations with refined mesh. In such a case, implementation of plastic properties would also have been an interesting study since behavior post yielding is just as relevant to bone quality as elastic properties.

5.4 FEM simulation of radiation and training

The final objective of the present study has been to create a model which simulates training and radiation of femur. Loading-induced bone formation and deterioration from radiation was defined to imitate the experimental findings and knowledge from literature. Since almost no significant measurements were obtained from the present experiments, this simulation was considered as a proof of concept and an investigation concerning the feasibility of the model setup. Although clear goals have been challenging to specify, the simulation model did achieve some results correlating with other studies. For instance, it has been shown that radiation reduces some qualities of cortical bone (Bartlow et al. 2018) and that training increases both bone mass and breaking force (Umemura et al. 1997). The presented model can thus be considered as a sufficient starting point for future studies. With some improvements, it may yield good correlations when comparing experimental and virtual assessments of corresponding specimens.

5.4.1 Simulated training

Different adaptation models found in literature are usually presented with the intention to reproduce the architecture of trabecular bone. The model employed in the present study (Eq. (3.11)) was developed using FE models of proximal epiphysis with uniform density distribution (Weinans et al. 1992). With a specimen-specific assessment of cortical bone, the purpose and objective of the present simulations are inherently different than what this model was originally designed for. It is thus possible that employing Huiskes's model has posed some weakness for virtual loading adaptation. For instance, the defined nodal densities from µCT images would most likely differ from what the model would give from a uniform distribution. Adaptations would thus partly emphasize on bone mineral relocation rather than formation. This might be the cause of some of the observed resorption on the cavity walls (Fig. 4.14).

It was expected that greater strain energy would occur near the muscle attachment points and the boundary surface of the FE model than elsewhere. However, these high SEDs could possibly affect the diaphysis and cause overestimated formation intensity and TPBT stiffness in the region of interest. Figure 5.13 displays the final density distribution of the FE model after simulation of rat 43. It shows significant formation where the quadriceps muscles were attached and some at the surface where the distal epiphysis was held in place. However, this does not seem to have affected the diaphyseal region to any extent.

Almost no formation was observed at the femoral head, suggesting that the contribution from quadriceps was overemphasized. The parameters of Huiskes's model were adjusted to obtain satisfactory adaptation response, but calculations of each muscle force were employed as described in Table 3.3 without further tuning. It is also possible that the omission of certain muscles and surrounding ligament, exerting a constant compressive force, caused incorrect loading conditions.

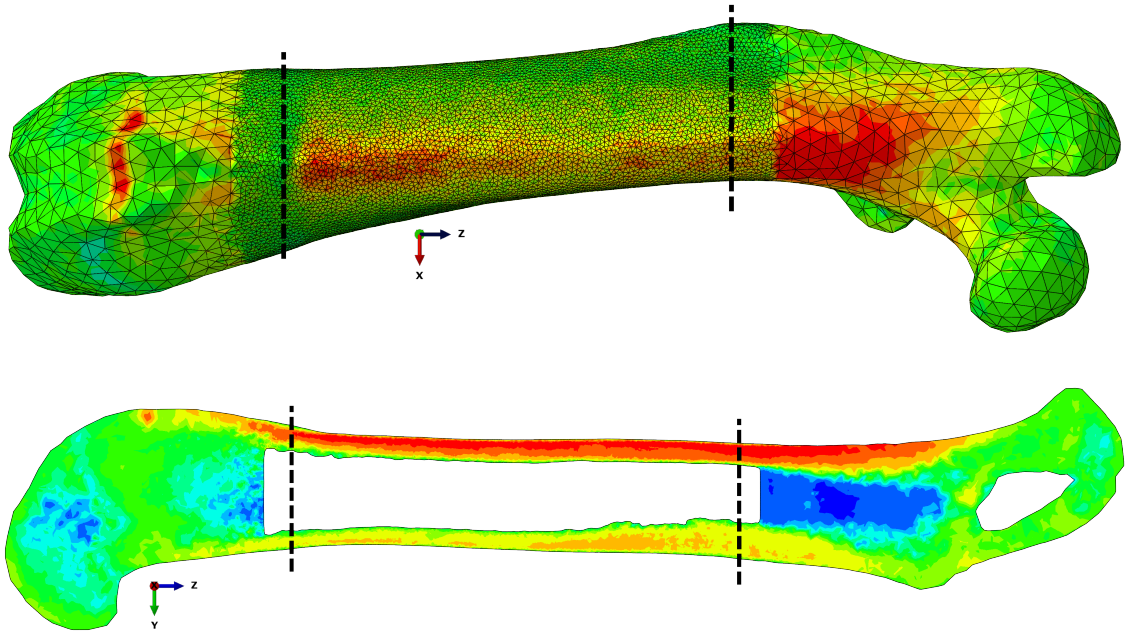

Figure 5.13: Final density distribution of full femur. The sudden change in density next to the quadriceps attachment point is caused by the different element sizes at the surface. The region bounded by the dashed lines corresponds with the volume used in TPBT. Bottom image is sliced at the middle of the model, separating the medial and lateral regions.

It has been discussed whether the influence of specimen-specific parameters on adaptation intensity was exaggerated. While resistance training does improve certain qualities of bone (Westerlind et al. 1998; Mosti et al. 2016), bone metabolism might not correlate with the loading magnitude. A similar study found five jumps per day to be as effective on BMD and strength improvement as any higher number of repetitions (Umemura et al. 1997), suggesting that calculations of accumulative loading (Eq. (3.10)) does not accurately correspond with experimental observations. Additionally, Huiskes's model was first suggested by employing the average SED from multiple loads (Huiskes et al. 1987). The present model obtains the highest strain energy instead. By considering average loads and omitting load accumulation, the simulation would emphasize more on training versus no training. However, simulation results would likely show weaker correlation with specimen-specific exercise programs.

Although higher cortical BMD was observed in the RadEx group than in the Rad-2 group, exercise-induced bone mineral formation does not fully conform with bone physiology. A possible solution could be to let an adaptation model determine α and β instead of ρ in $E = \alpha\rho^{\beta}$. Several empirical values of α and β have been proposed in different studies, suggesting that these parameters correlate better than the apparent densities with specimen-specific variation. Another interesting suggestion is to incorporate construction and removal of elements in regions with very high and very low density, respectively. Some studies have seen increased cortical thickness and cross section area in rats undergoing some form of exercise (Umemura et al. 1997).

A different approach to simulate bone remodeling, not considered in this study, is by utilizing machine learning. Such a method does not account for every single physiological event or every contributing variable. However, with the remarkable amount of different parameters to account for, a straightforward trial-and-error strategy might be better suited for *in silico* adaptation. Tiwari and Kumar (2018) obtained satisfactory correlation with experimental tests by using a neural network. From three input variables (loading strain, frequency and number of cycles) they predicted the mineral apposition rate in exercised mice. With sufficient data, a similar neural network could possibly be employed to assess the effects concerned in this study.

5.4.2 Simulated radiation

The radiation damage model caused 9.7 % reduction of nodal density in the entire FE model (Fig. 4.15). As no significant difference was measured between the experimental radiated and control group, this impact was possibly somewhat exaggerated. The simulation did however not consider femur growth or growth reduction. The strong density reduction could therefore to some extent correspond with this effect.

Since all specimens underwent the same radiation therapy, other combinations of radiation intensity and frequency were not further tested. Some studies suggest that deterioration is lessened when radiation is divided into several events (Mustafy et al. 2018). A future improvement to the presented model could be to record the number of radiations and consider this variable when calculating each damage rate coefficient. Another alteration could be to let damage rate depend on the current local density. This would better conform with radiation being more detrimental to trabecular bone than cortical bone. For instance, the damage rate coefficient expression (Eq. (3.14)) could be multiplied by a factor inversely proportional to the respective nodal density.

Just as for exercise and adaptation, radiation is not directly correlated with BMD loss. Certain mechanical qualities are however reduced. A suggestion is to also make radiation damage affect the α and β parameters in $E = \alpha\rho^{\beta}$. One could also introduce an expression for parameter change in models where density-dependent yield stress is included. Alternatively, radiation could cause element removal, as described above. Both Bartlow et al. (2018) and Mustafy et al. (2018) found significant difference in cortical thickness between radiated and non-radiated femur while no significant difference in cortical BMD was measured, suggesting that radiation inflicts more damage to geometrical properties than apparent density. Generation and removal of voxel elements does however move away from an important goal of this study, which is employing continuum mechanics to express bone properties.

A persistent reduction of adaptation efficiency was induced by the radiation. Although the final density distribution and stiffness response were satisfactory, these values would probably be higher than expected with no radiation. It is suggested in a future model that radiation effect on adaptation is gradually reduced so that the remodeling rate coefficient and reference stimulus eventually go back to their initial values.

6 | Conclusion and further work

In this study, effects of radiation therapy and training on the mechanical performance of bone have been investigated. Despite the lack of significant differences, some clear tendencies have been shown. The findings suggest that radiation-induced reduction of bone metabolism causes weakened Young's modulus, yield stress and ultimate stress of cortical bone. There are also indications that exercise might improve the mentioned properties in radiated bone. The study is however inconclusive regarding this matter, and further testing is advised to confirm these propositions. Still, the presented findings did to some extent conform with the *in vivo* comparative medicine animal study, which obtained no significant results as well. In any case, physical activity should never be discouraged because of these findings.

The study was not able to reproduce the experimental and virtual TPBT correlations of Ramezanzadehkoldeh and Skallerud (2017a). The reason for this was likely a combination of different testing setup, data acquisition and FE modeling procedure. Through a thorough discussion, several adjustments to the current setup have been proposed to avoid similarly undesirable correlations in future studies. Some of these modifications, like better definition of global orientation and region of interest, might also produce better results when assessing training and radiation effects. Low specimen aspect ratio was a persistent challenge in this study. It is suggested to strive for a higher ratio in future TPBT of long bones, preferably $L/d > 9$. The significant importance of voxel and element size when modeling bone has also been demonstrated. Microscopic variations in bone structure must be adequately accounted for to rightfully assume material continuity.

Some important considerations regarding *in silico* testing of bone quality have been unveiled. Development of solid methods for virtual testing may present efficient and economical alternatives to physical assessment of CTIBL. Patient-specific µCT-FE analysis can also provide additional data for evaluating medical treatment.

Finally, a model for virtual training and radiation simulation has been presented. Employing corresponding programs as in the experiments did yield some satisfactory evolution of apparent density distribution and TPBT stiffness. With further development, this preliminary model should better account for various physiological aspects of bone metabolism and training/radiation response. With sufficient improvement and calibration, in combination with µCT-FE modeling, this model can present accurate predictions of exercise treatment effect on cancer patients. Specific measures can thus be considered to attenuate radiation therapy side effects.

References

Adams, G. J., Cook, R. B., Hutchinson, J. R., and Zioupos, P. (2018). "Bone apparent and material densities examined by cone beam computed tomography and the Archimedes technique: Comparison of the two methods and their results". In: 3, p. 23. ISSN: 2297-3079. DOI: 10.3389/fmech.2017.00023.

Arias-Moreno, A. J., Ito, K., and van Rietbergen, B. (2020). "Accuracy of beam theory for estimating bone tissue modulus and yield stress from 3-point bending tests on rat femora". In: *Journal of Biomechanics* 101, p. 109654. ISSN: 0021-9290. DOI: 10.1016/j.jbiomech.2020.109654.

Auestad, M. F. (2020). "Radiation therapy and training effects on the mechanical performance of bone". unpublished thesis.

Bartlow, C. M., Mann, K. A., Damron, T. A., and Oest, M. E. (2018). "Limited field radiation therapy results in decreased bone fracture toughness in a murine model". In: *PLoS ONE* 13.10, e0204928. ISSN: 1932-6203. DOI: 10.1371/journal.pone.0204928.

Beaupré, G. S., Orr, T. E., and Carter, D. R. (1990). "An approach for time-dependent bone modeling and remodeling—application: A preliminary remodeling simulation". In: *Journal of Orthopaedic Research* 8.5, pp. 662–670. DOI: 10.1002/jor.1100080507.

Bonfield, W. and Datta, P. (1974). "Young's modulus of compact bone". In: *Journal of Biomechanics* 7.2, pp. 147–149. ISSN: 0021-9290. DOI: 10.1016/0021-9290(74)90053-0.

Bouxsein, M. L., Boyd, S. K., Christiansen, B. A., Guldberg, R. E., Jepsen, K. J., and Müller, R. (2010). "Guidelines for assessment of bone microstructure in rodents using micro–computed tomography". In: *Journal of Bone and Mineral Research* 25.7, pp. 1468–1486. DOI: 10.1002/jbmr.141.

Carter, D., Fyhrie, D., and Whalen, R. (1987). "Trabecular bone density and loading history: Regulation of connective tissue biology by mechanical energy". In: *Journal of Biomechanics* 20.8, pp. 785–794. ISSN: 0021-9290. DOI: 10.1016/0021-9290(87)90058-3.

Chandra, A., Lin, T., Tribble, M. B., Zhu, J., Altman, A. R., Tseng, W.-J., Zhang, Y., Akintoye, S. O., Cengel, K., Liu, X. S., and Qin, L. (2014). "PTH1–34 alleviates radiotherapy-induced local bone loss by improving osteoblast and osteocyte survival". In: *Bone* 67, pp. 33–40. ISSN: 8756-3282. DOI: 10.1016/j.bone.2014.06.030.

Charles, J. P., Cappellari, O., Spence, A. J., Hutchinson, J. R., and Wells, D. J. (2016a). "Muscle moment arms and sensitivity analysis of a mouse hindlimb musculoskeletal model". In: *Journal of anatomy* 229.4, pp. 514–535. ISSN: 0021-8782. DOI: 10.1111/joa.12461.

– (2016b). "Musculoskeletal geometry, muscle architecture and functional specialisations of the mouse hindlimb". In: *PloS one* 11.4, e0147669–e0147669. ISSN: 1932-6203. DOI: 10.1371/journal.pone.0147669.

Cory, E., Nazarian, A., Entezari, V., Vartanians, V., Müller, R., and Snyder, B. D. (2010). "Compressive axial mechanical properties of rat bone as functions of bone volume fraction, apparent density and micro-ct based mineral density". In: *Journal of Biomechanics* 43.5, pp. 953–960. ISSN: 0021-9290. DOI: 10.1016/j.jbiomech.2009.10.047.

D'Oronzo, S., Stucci, S., Tucci, M., and Silvestris, F. (2015). "Cancer treatment-induced bone loss (CTIBL): Pathogenesis and clinical implications". In: *Cancer Treatment Reviews* 41.9, pp. 798–808. ISSN: 0305-7372. DOI: 10.1016/j.ctrv.2015.09.003.

Eimori, K., Endo, N., Uchiyama, S., Takahashi, Y., Kawashima, H., and Watanabe, K. (2016). "Disrupted bone metabolism in long-term bedridden patients". In: *PLOS ONE* 11.6, pp. 1–11. DOI: 10.1371/journal.pone.0156991.

Frost, H. M. (2004). "A 2003 update of bone physiology and Wolff's law for clinicians". In: *The Angle Orthodontist* 74.1, pp. 3–15. ISSN: 0003-3219. DOI: 10.1043/0003-3219(2004)074<0003:AUOBPA>2.0.CO;2. PMID: 15038485.

Gross, T., Pahr, D. H., Peyrin, F., and Zysset, P. K. (2012). "Mineral heterogeneity has a minor influence on the apparent elastic properties of human cancellous bone: a SRμCT-based finite element study". In: *Computer Methods in Biomechanics and Biomedical Engineering* 15.11, pp. 1137–1144. DOI: 10.1080/10255842.2011.581236.

Gupta, S. and Dan, P. (2004). "Bone geometry and mechanical properties of the human scapula using computed tomography data". In: *Trends Biomater Artif Organs* 17. URL: https://www.thefreelibrary.com/Bone+geometry+and+mechanical+properties+of+the+human+scapula+using...-a0165431696.

Hao, W., Xie, J., and Wang, F. (2018). "Theoretical prediction for large deflection with local indentation of sandwich beam under quasi-static lateral loading". In: *Composite Structures* 192, pp. 206–216. ISSN: 0263-8223. DOI: 10.1016/j.compstruct.2018.02.097.

Hernandez, C., Beaupré, G., Keller, T., and Carter, D. (2001). "The influence of bone volume fraction and ash fraction on bone strength and modulus". In: *Bone* 29.1, pp. 74–78. ISSN: 8756-3282. DOI: 10.1016/S8756-3282(01)00467-7.

Huiskes, R., Weinans, H., Grootenboer, H., Dalstra, M., Fudala, B., and Slooff, T. (1987). "Adaptive bone-remodeling theory applied to prosthetic-design analysis". In: *Journal of Biomechanics* 20.11. F. Gaynor Evans Anniversary Issue on Bone Biomechanics, pp. 1135–1150. ISSN: 0021-9290. DOI: 10.1016/0021-9290(87)90030-3.

Jee, W. S. S. (2001). "Integrated Bone Tissue Physiology: Anatomy and Physiology". In: *Bone Mechanics Handbook*. Ed. by S. Cowin. Second Edition. Boca Raton, Florida: CRC Press LLC, pp. 1-1–1-68. ISBN: 978-0-8493-9117-0. DOI: 10.1201/b14263.

Johnson, W. L., Jindrich, D. L., Roy, R. R., and Reggie Edgerton, V. (2008). "A three-dimensional model of the rat hindlimb: Musculoskeletal geometry and muscle moment arms". In: *Journal of Biomechanics* 41.3, pp. 610–619. ISSN: 0021-9290. DOI: 10.1016/j.jbiomech.2007.10.004.

Karim, L., Hussein, A. I., Morgan, E. F., and Bouxsein, M. L. (2013). "Chapter 19 - The Mechanical Behavior of Bone". In: *Osteoporosis*. Ed. by R. Marcus, D. Feldman, D. W. Dempster, M. Luckey, and J. A. Cauley. Fourth Edition. San Diego: Academic Press, pp. 431–452. ISBN: 978-0-12-415853-5. DOI: 10.1016/B978-0-12-415853-5.00019-4.

Karim, L. and Judex, S. (2014). "Low level irradiation in mice can lead to enhanced trabecular bone morphology". In: *Journal of bone and mineral metabolism* 32.5, pp. 476–483. ISSN: 0914-8779. DOI: 10.1007/s00774-013-0518-x.

Kohles, S. S., Bowers, J. R., Vailas, A. C., and Vanderby, R. J. (1997). "Ultrasonic wave velocity measurement in small polymeric and cortical bone specimens". In: *Journal of biomechanical engineering* 119.3, pp. 232–236. ISSN: 0148-0731. DOI: 10.1115/1.2796085.

Lee, K.-L., Baldassarri, M., Gupta, N., Pinisetty, D., Janal, M. N., Tovar, N., and Coelho, P. G. (2012). "Nanomechanical characterization of canine femur bone for strain rate sensitivity in the quasistatic range under dry versus wet conditions". In: *International journal of biomaterials* 2012, pp. 415230–6. ISSN: 1687-8787. DOI: 10.1155/2012/415230.

Martin, R. B., Burr, D. B., Sharkey, N. A., and Fyhrie, D. P. (2015). *Skeletal Tissue Mechanics*. Second Edition. New York, NY: Springer New York. ISBN: 9781493930012. DOI: 10.1007/978-1-4939-3002-9.

Materialise NV (2020). *Materialise Mimics 23.0 User Guide*. Leuven, Belgium.

Morgan, E. F., Barnes, G. L., and Einhorn, T. A. (2013). "Chapter 1 - The Bone Organ System: Form and Function". In: *Osteoporosis*. Ed. by R. Marcus, D. Feldman, D. W. Dempster, M. Luckey, and J. A. Cauley. Fourth Edition. San Diego: Academic Press, pp. 3–20. ISBN: 978-0-12-415853-5. DOI: 10.1016/B978-012370544-0.50003-3.

Mosti, M. P., Ericsson, M., Erben, R. G., Schüler, C., Syversen, U., and Stunes, A. K. (2016). "The PPARα agonist fenofibrate improves the musculoskeletal effects of exercise in ovariectomized rats". In: *Endocrinology* 157.10, pp. 3924–3934. ISSN: 0013-7227. DOI: 10.1210/en.2016-1114.

Mustafy, T., Benoit, A., Londono, I., Moldovan, F., and Villemure, I. (2018). "Can repeated in vivo micro-CT irradiation during adolescence alter bone microstructure, histomorphometry and longitudinal growth in a rodent model?" In: *PLoS ONE* 13.11, e0207323. ISSN: 1932-6203. DOI: 10.1371/journal.pone.0207323.

Nilsson, M., Ohlsson, C., Mellström, D., and Lorentzon, M. (2013). "Sport-specific association between exercise loading and the density, geometry, and microstructure of weight-bearing bone in young adult men". In: *Osteoporosis International* 24.5, pp. 1613–1622. ISSN: 0937-941X. DOI: 10.1007/s00198-012-2142-3.

Ramezanzadehkoldeh, M. and Skallerud, B. H. (2017a). "MicroCT-based finite element models as a tool for virtual testing of cortical bone". In: *Medical Engineering and Physics* 46, pp. 12–20. ISSN: 1350-4533. DOI: 10.1016/j.medengphy.2017.04.011.

Ramezanzadehkoldeh, M. and Skallerud, B. H. (2017b). "Nanoindentation response of cortical bone: dependency of subsurface voids". In: *Biomechanics and modeling in mechanobiology* 16.5, pp. 1599–1612. ISSN: 1617-7959. DOI: 10.1007/s10237-017-0907-5.

Ruimerman, R., Rietbergen, B. van, Hilbers, P., and Huiskes, R. (2003). "A 3-dimensional computer model to simulate trabecular bone metabolism". In: *Biorheology* 40.1–3, pp. 315–320. ISSN: 0006-355X. PMID: 12454421.

Schileo, E., Taddei, F., Malandrino, A., Cristofolini, L., and Viceconti, M. (2007). "Subject-specific finite element models can accurately predict strain levels in long bones". In: *Journal of Biomechanics* 40.13, pp. 2982–2989. ISSN: 0021-9290. DOI: 10.1016/j.jbiomech.2007.02.010.

Schriefer, J. L., Robling, A. G., Warden, S. J., Fournier, A. J., Mason, J. J., and Turner, C. H. (2005). "A comparison of mechanical properties derived from multiple skeletal sites in mice". In: *Journal of Biomechanics* 38.3, pp. 467–475. ISSN: 0021-9290. DOI: 10.1016/j.jbiomech.2004.04.020.

Spatz, H., O'Leary, E. J., and Vincent, J. F. V. (1996). "Young's moduli and shear moduli in cortical bone". In: *Proceedings of the Royal Society of London. Series B: Biological Sciences* 263.1368, pp. 287–294. ISSN: 0962-8452. DOI: 10.1098/rspb.1996.0044.

Taddei, F., Pancanti, A., and Viceconti, M. (2004). "An improved method for the automatic mapping of computed tomography numbers onto finite element models". In: *Medical Engineering & Physics* 26.1, pp. 61–69. ISSN: 1350-4533. DOI: 10.1016/S1350-4533(03)00138-3.

The Biology Corner. *Rat External Anatomy*. URL: https://www.biologycorner.com/worksheets/rat_external.html (visited on 01/03/2021).

Tiwari, A. K. and Kumar, N. (2018). "Establishing the relationship between loading parameters and bone adaptation". In: *Medical Engineering and Physics* 56, pp. 16–26. ISSN: 1350-4533. DOI: 10.1016/j.medengphy.2018.04.004.

Umemura, Y., Ishiko, T., Yamauchi, T., Kurono, M., and Mashiko, S. (1997). "Five jumps per day increase bone mass and breaking force in rats". In: *Journal of Bone and Mineral Research* 12.9, pp. 1480–1485. ISSN: 0884-0431. DOI: 10.1359/jbmr.1997.12.9.1480.

University of Texas. *Essentials of Computed Tomography*. URL: https://www.ctlab.geo.utexas.edu/about-ct/essentials-of-computed-tomography/ (visited on 12/24/2020).

Van Lenthe, G. H., Voide, R., Boyd, S. K., and Müller, R. (2008). "Tissue modulus calculated from beam theory is biased by bone size and geometry: Implications for the use of three-point bending tests to determine bone tissue modulus". In: *Bone* 43.4, pp. 717–723. ISSN: 8756-3282. DOI: 10.1016/j.bone.2008.06.008.

Vico, L., Collet, P., Guignandon, A., Lafage-Proust, M.-H., Thomas, T., Rehailia, M., and Alexandre, C. (2000). "Effects of long-term microgravity exposure on cancellous and cortical weight-bearing bones of cosmonauts". In: *The Lancet* 355.9215, pp. 1607–1611. ISSN: 0140-6736. DOI: 10.1016/s0140-6736(00)02217-0.

Weinans, H., Huiskes, R., and Grootenboer, H. (1992). "The behavior of adaptive bone-remodeling simulation models". In: *Journal of Biomechanics* 25.12, pp. 1425–1441. ISSN: 0021-9290. DOI: 10.1016/0021-9290(92)90056-7.

Westerlind, K. C., Fluckey, J. D., Gordon, S. E., Kraemer, W. J., Farrell, P. A., and Turner, R. T. (1998). "Effect of resistance exercise training on cortical and cancellous bone in mature male rats". In: *Journal of Applied Physiology* 84.2, pp. 459–464. ISSN: 8750-7587. DOI: 10.1152/jappl.1998.84.2.459.

Whalen, R., Carter, D., and Steele, C. (1988). "Influence of physical activity on the regulation of bone density". In: *Journal of Biomechanics* 21.10, pp. 825–837. ISSN: 0021-9290. DOI: 10.1016/0021-9290(88)90015-2.

WHO. *Cancer*. URL: https://www.who.int/news-room/fact-sheets/detail/cancer (visited on 12/22/2020).

Wirtz, D. C., Schiffers, N., Pandorf, T., Radermacher, K., Weichert, D., and Forst, R. (2000). "Critical evaluation of known bone material properties to realize anisotropic FE-simulation of the proximal femur". In: *Journal of Biomechanics* 33.10, pp. 1325–1330. ISSN: 0021-9290. DOI: 10.1016/S0021-9290(00)00069-5.

Yang, H., Ma, X., and Guo, T. (2010). "Some factors that affect the comparison between isotropic and orthotropic inhomogeneous finite element material models of femur". In: *Medical Engineering & Physics* 32.6, pp. 553–560. ISSN: 1350-4533. DOI: 10.1016/j.medengphy.2010.01.004.

Yeo, S. H., Mullens, C. H., Sandercock, T. G., Pai, D. K., and Tresch, M. C. (2011). "Estimation of musculoskeletal models from in situ measurements of muscle action in the rat hindlimb". In: *Journal of Experimental Biology* 214.5, pp. 735–746. ISSN: 0022-0949. DOI: 10.1242/jeb.049163.

Zhai, J., He, F., Wang, J., Chen, J., Tong, L., and Zhu, G. (2019). "Influence of radiation exposure pattern on the bone injury and osteoclastogenesis in a rat model". In: *International journal of molecular medicine* 44.6, pp. 2265–2275. ISSN: 1107-3756. DOI: 10.3892/ijmm.2019.4369.

Appendix A: Midspan cross sections

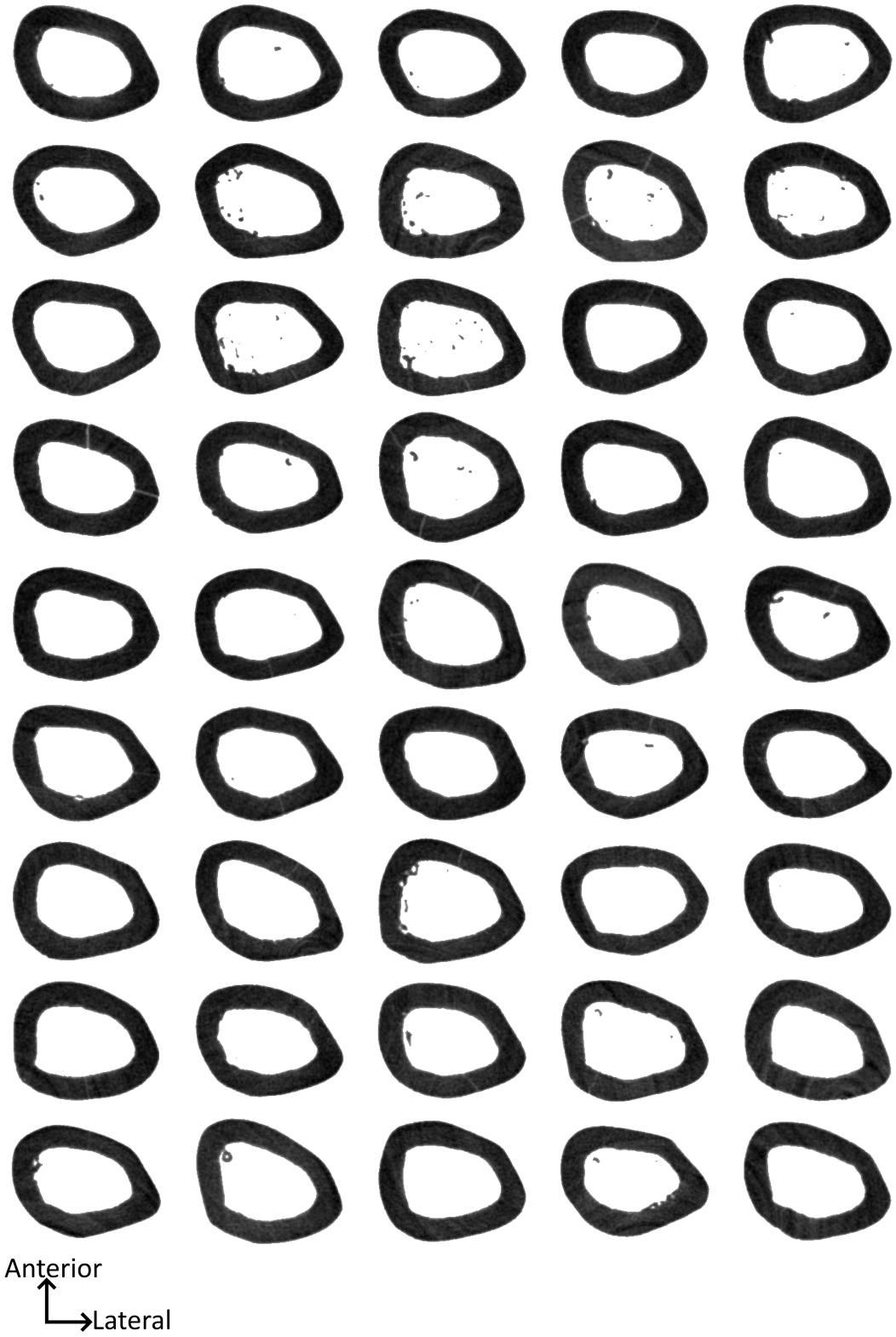

Femur 1–48, sorted in rising order, left to right and downwards. Femurs 9, 10 and 24 are excluded.

Appendix B: Test results, first experiment

Femur	Group	Stiffness [N/mm]	Yield force [N]	Ultimate force [N]	Work [Nmm]	I_x [mm^4]	Area [mm^2]	c [mm]	Young's modulus [N/mm^2]	Yield stress [N/mm^2]	Ultimate stress [N/mm^2]
1	Rad-1	520.39	88.00	133.89	55.69	5.411	6.050	1.637	4267.33	79.86	121.52
2	Rad-1	478.71	72.42	123.19	59.76	5.704	5.886	1.686	3782.59	64.22	109.24
3	Rad-1	448.58	75.53	123.67	72.04	5.414	5.874	1.606	3697.57	67.22	110.06
4	Ctrl	393.77	86.25	119.70	63.07	4.779	6.005	1.527	3579.98	82.68	114.74
5	Ctrl	400.08	74.99	118.21	69.74	7.399	6.429	1.792	2529.10	54.48	85.89
6	Ctrl	438.84	79.52	134.14	94.51	5.723	6.230	1.655	3419.78	68.99	116.37
7	Ctrl	416.14	84.89	109.09	37.80	7.879	6.961	1.845	2460.92	59.63	76.64
8	Ctrl	643.54	95.45	156.84	60.43	5.824	6.423	1.686	4915.71	82.89	136.21
9	Ctrl	238.11	16.95	43.96	5.69						
10	Ctrl	225.53	51.15	59.63	13.82						
11	Ctrl	380.30	90.18	111.52	39.71	6.229	6.155	1.717	2776.24	74.57	92.22
12	Ctrl	479.95	88.81	115.08	47.44	5.688	6.167	1.642	3766.10	76.91	99.67
13	Ctrl	489.86	63.49	127.10	33.80	7.278	6.734	1.836	3103.93	48.05	96.19
14	Ctrl	592.52	95.40	141.96	51.64	7.675	6.902	1.819	3582.76	67.83	100.93
15	Ctrl	407.78	105.22	105.95	16.09	8.146	6.956	1.797	2350.80	69.63	70.12
16	Rad-1	379.48	87.92	119.57	57.22	4.787	5.762	1.584	3470.26	87.28	118.70
17	Rad-1	511.46	89.33	125.55	59.20	6.866	6.546	1.717	3413.00	67.02	94.19
18	Rad-1	314.06	77.15	105.58	47.1	5.599	6.07	1.615	2503.62	66.76	91.36
19	Rad-1	485.66	82.26	124.55	64.21	5.590	6.218	1.624	3858.71	71.70	108.55
20	Rad-1	340.80	66.53	73.71	14.42	7.515	6.571	1.872	2118.00	49.72	55.08
21	Rad-1	438.23	93.49	131.95	56.50	6.873	6.772	1.726	2901.11	70.43	99.41
22	Rad-1	476.22	89.09	121.27	62.33	6.644	6.230	1.810	3295.83	72.81	99.11
23	Rad-1	586.01	92.51	128.59	80.66	5.414	6.072	1.593	4800.00	81.66	113.51
24	Rad-1										

Appendix C: Force-displacement, first experiment

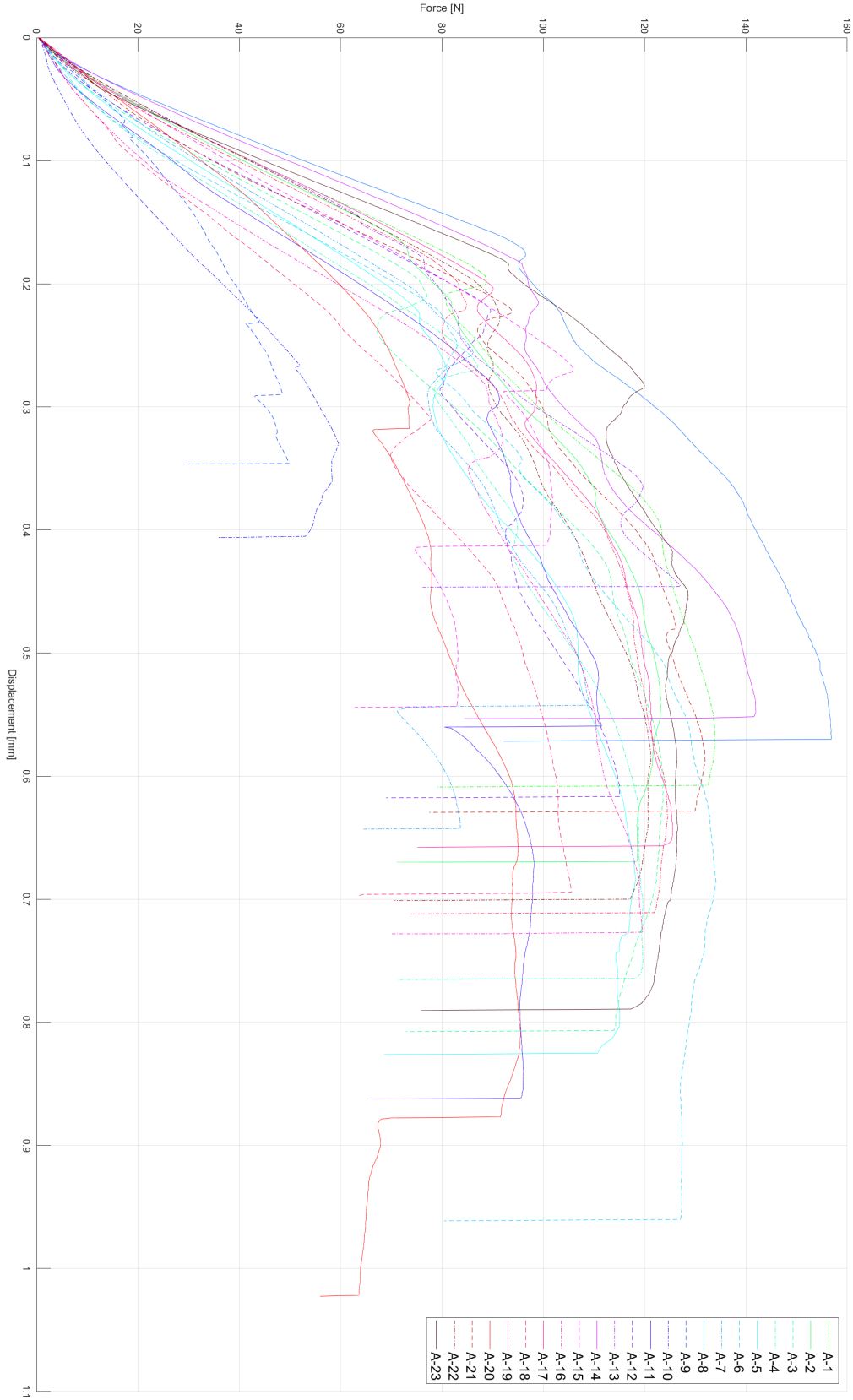

Appendix D: Test results, second experiment

Femur	Group	Stiffness [N/mm]	Yield force [N]	Ultimate force [N]	Work [Nmm]	I_x [mm^4]	Area [mm^2]	c [mm]	Young's modulus [N/mm^2]	Yield stress [N/mm^2]	Ultimate stress [N/mm^2]
25	Rad-2	432.32	83.44	129.14	68.64	8.065	6.966	1.779	2510.66	55.22	85.46
26	Rad-2	357.83	95.74	121.68	51.86	8.028	6.663	1.907	2107.29	68.23	86.71
27	Rad-2	475.25	69.63	118.39	29.62	6.054	6.275	1.712	3534.96	59.07	100.44
28	Rad-2	586.08	104.21	121.83	41.20	4.435	5.678	1.540	5723.49	108.56	126.91
29	Rad-2	546.53	93.08	121.96	71.52	6.390	6.357	1.699	3883.75	74.25	97.28
30	Rad-2	385.99	71.83	100.98	53.79	6.584	6.622	1.717	2656.10	56.20	79.00
31	Rad-2	561.05	89.03	135.37	50.91	5.358	6.257	1.566	4608.94	78.06	118.70
32	Rad-2	537.84	56.70	135.68	58.33	5.884	6.406	1.673	4076.51	48.36	115.73
33	Rad-2	480.79	91.30	121.03	34.95	6.101	6.393	1.651	3540.91	74.12	98.26
34	Rad-2	477.41	81.66	143.24	73.56	6.183	6.310	1.752	3487.85	69.42	121.76
35	Rad-2	464.79	69.51	122.07	68.53	7.888	6.566	1.876	2783.82	49.59	87.10
36	Rad-2	358.79	119.8	144.29	74.05	7.131	6.442	1.836	2332.62	92.53	111.45
37	RadEx	473.26	76.80	133.28	56.84	5.801	5.959	1.655	3680.33	65.73	114.07
38	RadEx	447.29	98.38	139.62	64.59	5.066	6.088	1.593	3866.22	92.81	131.71
39	RadEx	450.26	77.80	120.24	48.55	5.524	5.935	1.633	3644.45	69.00	106.64
40	RadEx	626.32	101.09	128.89	72.21	6.309	6.505	1.646	4475.07	79.12	100.88
41	RadEx	478.33	101.86	126.29	37.38	6.383	6.657	1.664	3370.32	79.66	98.77
42	RadEx	424.08	96.56	97.52	12.99	7.374	6.515	1.788	2679.64	70.24	70.94
43	RadEx	575.28	93.43	148.63	52.22	6.072	6.380	1.708	4254.74	78.84	125.42
44	RadEx	502.82	85.45	133.04	38.81	7.111	7.054	1.743	3212.76	62.83	97.83
45	RadEx	404.89	84.66	135.09	52.60	6.503	6.251	1.774	2847.70	69.29	110.56
46	RadEx	594.53	85.69	146.24	53.51	7.641	6.914	1.788	3605.94	60.15	102.66
47	RadEx	648.61	100.22	157.83	82.15	6.532	6.979	1.668	4444.60	76.78	120.91
48	RadEx	380.49	91.03	129.37	54.35	5.659	6.027	1.637	3011.41	79.00	112.27

Appendix E: Force-displacement, second experiment

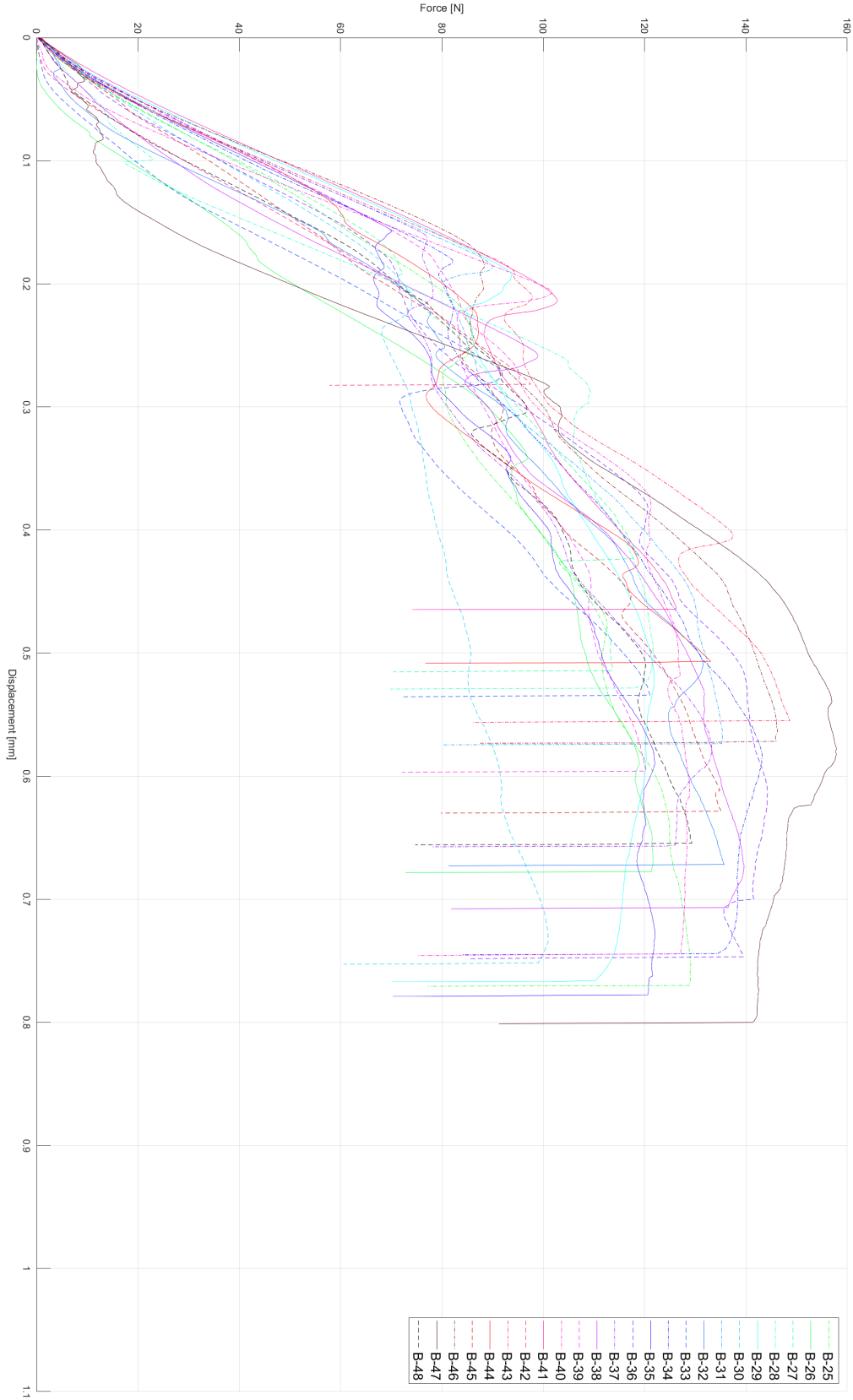

Appendix F: Cross section analysis script

```
%% Initial
clear; close; clc; format long;

th = 20000; %Threshold
pixRes = 0.0177; %Original pixelsize
scaling = 4; %Image scaling
pixRes = pixRes/scaling;

%% Read
files = dir('*.tif');
NoSamples = length(files);
sample(NoSamples) = struct;
for i = 1:NoSamples
    sample(i).name = files(i).name;
    sample(i).img.im = imread(sample(i).name);
    % Apply zero value to pixels below threshold
    sample(i).img(1).im = threshold(sample(i).img(1).im,th);
    % Crop image to fit only cross section
    sample(i).img(1).im = crop(sample(i).img(1).im);
    % Scale up the image to n times size
    sample(i).img(1).im = resize(sample(i).img(1).im,scaling);
    % Obtain number of pixels in each direction
    sample(i).img(1).res = size(sample(i).img(1).im);
    % Calculate area/number of non-zero pixels
    sample(i).img(1).A = Area(sample(i).img(1).im,pixRes);
    % Calculate CoM, pixelwise
    sample(i).img(1).CoM = CentreOfMass(sample(i).img(1).im);
    % Calculate EI, with Steiner
    sample(i).img(1).I = MomentArea(sample(i).img(1),pixRes);
    % Calculate pixelwise distance
    sample(i).img(1).c = FarthestFiber(sample(i).img(1),pixRes);
end

%% Funcion Threshold
function mat = threshold(mat,th)
    for i = 1:size(mat,1)
        for j = 1:size(mat,2)
            if mat(i,j) < th
                mat(i,j) = 0;
            end
        end
    end
end
```

```
44
45  %% Function Crop
46  function mat = crop(mat)
47      flag = false;
48      % Top
49      for i = 1:size(mat,1)
50          for j = 1:size(mat,2)
51              if mat(i,j) > 0
52                  top = i;
53                  flag = true;
54                  break
55              end
56          end
57          if flag
58              break
59          end
60      end
61      flag = false;
62      % Left
63      for j = 1:size(mat,2)
64          for i = 1:size(mat,1)
65              if mat(i,j) > 0
66                  left = j;
67                  flag = true;
68                  break
69              end
70          end
71          if flag
72              break
73          end
74      end
75      flag = false;
76      % Bottom
77      for i = size(mat,1):-1:1
78          for j = size(mat,2):-1:1
79              if mat(i,j) > 0
80                  bottom = i;
81                  flag = true;
82                  break
83              end
84          end
85          if flag
86              break
87          end
88      end
89      flag = false;
90      % Right
91      for j = size(mat,2):-1:1
```

```
        for i = size(mat,1):-1:1
            if mat(i,j) > 0
                right = j;
                flag = true;
                break
            end
        end
        if flag
            break
        end
    end
    mat = mat(top:bottom,left:right);
end

%% Function Resize
function new_mat = resize(mat,n)
    new_mat = zeros(size(mat)*n);
    for i = 1:size(new_mat,1)
        for j = 1:size(new_mat,2)
            new_mat(i,j) = mat(ceil(i/n),ceil(j/n));
        end
    end
end

%% Function Area
function A = Area(mat,pixRes)
    % pixel-size
    A.pixel = numel(mat(mat>0));
    % Real size
    A.real = A.pixel*pixRes^2;
end

%% Function CentreOfMass
function CoM = CentreOfMass(mat)
    % Top to bottom
    weight = zeros(size(mat,1),1);
    for i = 1:size(mat,1)
        weight(i) = sum(mat(i,:));
    end
    CoM.Y = weight.*(1:1:length(weight))';
    if size(CoM.Y,1) == size(CoM.Y,2)
        CoM.Y = diag(CoM.Y);
    end
    CoM.Y = round(sum(CoM.Y(:)) / sum(weight(:)));
    % Left to right
    weight = zeros(size(mat,2),1);
    for i = 1:size(mat,2)
        weight(i) = sum(mat(:,i));
```

```
    end
    CoM.X = weight.*(1:1:length(weight))';
    if size(CoM.X,1) == size(CoM.X,2)
        CoM.X = diag(CoM.X);
    end
    CoM.X = round(sum(CoM.X(:)) / sum(weight(:)));
end

%% Function MomentArea
function I = MomentArea(img,pixRes)
    % About X
    I.X = 0;
    for i = 1:size(img.im,1)
        vox = img.im(i,:);
        I.X = I.X + (numel(vox(vox>0))*pixRes^4)*...
            (1/12 + (abs(i-img.CoM.Y))^2);
    end
    % About Y
    I.Y = 0;
    for i = 1:size(img.im,2)
        vox = img.im(:,i);
        I.Y = I.Y + (numel(vox(vox>0))*pixRes^4)*...
            (1/12 + (abs(i-img.CoM.X))^2);
    end
end

%% Function FarthestFiber
function c = FarthestFiber(img,pixRes)
    c.pix.Y = max( abs(img.CoM.Y-1), ...
        abs(img.res(1)-img.CoM.Y) );
    c.pix.X = max( abs(img.CoM.X-1), ...
        abs(img.res(2)-img.CoM.X) );

    c.real.Y = pixRes * max( abs(img.CoM.Y-1), ...
        abs(img.res(1)-img.CoM.Y) );
    c.real.X = pixRes * max( abs(img.CoM.X-1), ...
        abs(img.res(2)-img.CoM.X) );
end
```

Appendix G: Mimics to Abaqus density conversion script

```
%% Initial
clear; clc; close; fclose('all'); format long
NoN_E = input('Number of nodes per element: ');
p = input('IDWI weight: ');

%% Get Part/Instance name
txtID = uigetfile('*.txt','Select text file containing rat parameters');
if (~txtID)
    disp('Error: A .txt file must be chosen!')
    fclose('all'); clear; return
else
    txt = fopen(txtID,'r');
end
if(strcmp(fgetl(txt),'Name of instance:'))
    prtNm = fgetl(txt);
else
    disp('Error: Wrong .txt file is chosen, or error in setup file!')
    fclose('all'); clear; return
end
cdbID = uigetfile('*.cdb','Select the .cdb file');
if (~cdbID)
    disp('Error: A .cdb file must be chosen!')
    fclose('all'); clear; return
else
    cdb = fopen(cdbID,'r');
end
csvID = uigetfile('*.csv','Select the .csv file');
if (~csvID)
    disp('Error: A .csv file must be chosen!')
    fclose('all'); clear; return
end
inpID = uigetfile('*.inp','Select the initial .inp file');
if (~inpID)
    disp('Error: A .inp file must be chosen!')
    fclose('all'); clear; return
else
    inp = fopen(inpID,'r');
end
disp(' '); disp('Performing density initiation')
disp(['Rat: ',txtID(1+3:end-4)])
disp(['Instance: ', prtNm])
disp(['Number of nodes per element: ', num2str(NoN_E)])
```

```
tStart = tic;

%% Count number of nodes and elements
[cdb, NoN, NoE] = NoN_NoE_counter(cdb,cdbID,NoN_E);
if NoE >= 1e7 || NoN >= 1e7
    % Run SpaceAdder, bacause MIMICS doesn't write enough empty columns
    disp('NoN or NoE is more than upper limit (9 999 999)')
    cdb = SpaceAdder(cdb,cdbID,NoN_E);
else
    disp('NoN and NoE within upper limit (9 999 999)'); disp(' ')
end

%% Import .cdb containing elements and belonging nodes
% Read nodes and their positions
disp('Extracting node positions')
cdbLine = fgetl(cdb);
while(~strcmp(cdbLine(1:5),'nbloc'))
    cdbLine = fgetl(cdb);
end
fgetl(cdb);
NodePos = (fscanf(cdb,'%g %g',[6 inf]))';
% Clean up the list (Remove some empty lines)
while(mean(NodePos(end,:)) <= 0)
    NodePos = NodePos(1:end-1,:);
end
% Finish clean: x, y, z (Remove everything else)
NodePos = NodePos(:,end-2:end);

%% Read elements and belonging nodes
disp('Extracting element information')
cdbLine = fgetl(cdb);
while(~strcmp(cdbLine(1:5),'ebloc'))
    cdbLine = fgetl(cdb);
end
fgetl(cdb);
cdbList = (fscanf(cdb,'%g %g',[(11+NoN_E) inf]))';
% Clean up the list (Remove some empty lines)
while(mean(cdbList(end,:)) <= 0)
    cdbList = cdbList(1:end-1,:);
end
% Finish clean: #node1, #node2, #node3, #node4 (Remove everything else)
cdbList = cdbList(:,end-(NoN_E-1):end);

%% In case of repetive nodes in .cdb file (Only for C3D4)
if NoN_E == 8 || NoN_E == 20
    NoN_E = NoN_E/2;
    disp(['Non-unique values activated, reducing NoN_E to ', ...
        num2str(NoN_E),' and removing extra entries'])
```

```
    for i = 1:NoE
        cdbList(i,1:NoN_E) = unique(cdbList(i,:),'stable');
    end
    cdbList = cdbList(:,1:NoN_E);
    disp('Extracted unique nodes from cdbList')
end

%% Import .csv containing element densities
disp('Extracting element positions and densities')
csvList = readtable(csvID);
csvList = table2array(csvList(:,1:4));
% Create list of element positions
ElemPos = csvList(:,1:3);
% Create list of element densities
csvList = csvList(:,4);

%% Create list of nodes with all elements they are tied to
disp('Creating node struct')
NodeStrt = struct();
NodeStrt(NoN).elms = [];
for i = 1:NoE
    for j = 1:NoN_E
        NodeStrt(cdbList(i,j)).elms = [NodeStrt(cdbList(i,j)).elms i];
    end
end

%% Inverse distanse weighted interpolation of node density
%% from belonging element densities
disp(' '); disp('Performing IDWI')
DensList = zeros(NoN,length(p));
for i = 1:NoN
    Npos = NodePos(i,:);
    Edens = csvList(NodeStrt(i).elms);
    Ex = ElemPos(NodeStrt(i).elms,1);
    Ey = ElemPos(NodeStrt(i).elms,2);
    Ez = ElemPos(NodeStrt(i).elms,3);
    % Calculate distances
    Dists = zeros(length(Ex),1);
    for j = 1:length(Dists)
        Dists(j) = hypot(Npos(1)-Ex(j),Npos(2)-Ey(j));
        Dists(j) = hypot(Dists(j),Npos(3)-Ez(j));
    end
    % IDWI:
    DensList(i) = ( sum(Edens./Dists.^p) ) / ( sum(1./Dists.^p) );
    if ~mod(i,2e5)
        disp(['Calculated ',num2str(i),' of ',num2str(NoN),' nodes'])
    end
end
```

```
disp(['Calculated ',num2str(NoN),' of ',num2str(NoN),' nodes'])

%% Add a new node set to the .inp file
disp(' '); disp('Adding a Load-Area node set to the .inp file')
[initSetNode,inp,restText] = SetnodeMaker(inp,inpID);
% Obtain the respective elements
setElems = [];
for i = 1:length(initSetNode)
    setElems = [setElems NodeStrt(initSetNode(i)).elms]; %#ok
end
% Obtain the respective nodes
setNode = [];
for i = 1:length(setElems)
    setNode = [setNode cdbList(setElems(i),:)]; %#ok
end
setNode = setNode(~ismember(setNode,initSetNode));
setNode = unique(setNode);
% Write the new set to the inp file
disp('Writing node set')
writeSetNode(inp,inpID,setNode,restText);

%% Write an extra .txt file containing stiff element set and extra section
disp(' '); disp('Creating an extra .txt file with stiff elements')
StiffElementWriter(inpID,cdbList,NodeStrt);

%% Write dens.txt file which later shall be included in the .inp file
disp(' '); disp('Writing densitiies to text file')
densfile = ['dens_',txtID(4:end)];
fich = fopen(densfile,'w');
for i = 1:NoN
    fprintf(fich,[prtNm, '.%.0f, %1.6f\n'], i, DensList(i,end));
end
fclose('all');
disp(' '); disp(['Density initiation of ',cdbID(1:end-4),' complete!'])

disp(' ')
disp(['Max element density: ', num2str(max(csvList(:)))])
disp(['Max node density: ', num2str(max(DensList(:)))])
disp(' ')
disp(['Min element density: ', num2str(min(csvList(:)))])
disp(['Min node density: ', num2str(min(DensList(:)))])
disp(' ')
disp(['Mean element density: ', num2str(mean(csvList(:)))])
disp(['Mean node density: ', num2str(mean(DensList(:)))])
disp(' ')

save('Dens_p.mat','DensList','p','csvList', '-v7.3')
disp('csvList, DensList and p saved to Dens_p.mat'); disp(' ')
```

```
tEnd = toc(tStart);
disp(['Total elapsed time: ',datestr(seconds(tEnd),'HH'), ...
    ' hours, ', datestr(seconds(tEnd),'MM'), ' minutes and ', ...
    datestr(seconds(tEnd),'SS'), ' seconds.'])
fclose('all');

%% Counter function:
function [cdb, NoN, NoE] = NoN_NoE_counter(f,cdbID,NoN_E)
    disp(' '); disp('Counting NoN and NoE')
    NoE = 0; %Counter
    NoN = 0; %Counter
    % Obtain NoN;
    Line = fgetl(f);
    while(~strcmp(Line(1:5),'nbloc'))
        Line = fgetl(f);
    end
    fgetl(f);
    Line = fgetl(f);
    while(length(Line) >= 8)
        if str2num(Line(1:8)) %#ok
            NoN = NoN + 1;
            Line = fgetl(f);
        else
            break
        end
    end
    % Obtain NoE;
    Line = fgetl(f);
    while(~strcmp(Line(1:5),'ebloc'))
        Line = fgetl(f);
    end
    fgetl(f);
    disp(' '); disp('Found the element list')
    Line = fgetl(f);
    while(length(Line) >= 8 && strcmp(Line(1:8),'       1'))
        NoE = NoE + 1;
        Line = fgetl(f);
        if (NoN_E >= 10)
            Line = fgetl(f);
        end
    end
    disp(' '); disp(['NoN: ',num2str(NoN)]); disp(['NoE: ',num2str(NoE)])
    disp(' ')
    fclose(f);
    cdb = fopen(cdbID,'r');
end

%% Space adding function:
```

```
function cdb = SpaceAdder(f,cdbID,NoN_E)
    disp('Fixing spaces on element lines'); disp(' ')
    s = '  '; %String to add
    w = fopen('cdb-lck.cdb','w');
    Line = fgetl(f);
    while(ischar(Line))
        fprintf(w,Line);
        fprintf(w,'\n');
        Line = fgetl(f);
        if strcmp(Line(1:5),'ebloc')
                fprintf(w,Line);
                fprintf(w,'\n');
                Line = fgetl(f);
                fprintf(w,Line);
                fprintf(w,'\n');
                break
        end
    end
    Line = fgetl(f); %First line of elements
    while(ischar(Line))
        if length(Line) < 8
            break
        elseif ~strcmp(Line(1:8),'       1')
            break
        end
        fprintf(w,[Line(1:80),s,Line(81:88),s,Line(89:96), ...
            s,Line(97:104),s,Line(105:112),s,Line(113:120)]);
        if NoN_E >= 10
            fprintf(w,[s,Line(121:128),s,Line(129:136), ...
                s,Line(137:144),s,Line(145:152)]);
            fprintf(w,'\n');
            Line = fgetl(f);
            fprintf(w,[Line(1:8),s,Line(9:16)]);
            if NoN_E == 20
                fprintf(w,[s,Line(17:24),s,Line(25:32), ...
                    s,Line(33:40),s,Line(41:48),s,Line(49:56), ...
                    s,Line(57:64),s,Line(65:72),s,Line(73:80), ...
                    s,Line(81:88),s,Line(89:96)]);
            end
        end
        if NoN_E == 8
            fprintf(w,[s,Line(121:128),s,Line(129:136), ...
                s,Line(137:144),s,Line(145:152)]);
        end
        fprintf(w,'\n');
        Line = fgetl(f);
    end
    while(ischar(Line))
```

```
283         fprintf(w,Line);
284         fprintf(w,'\n');
285         Line = fgetl(f);
286     end
287     fclose(f);
288     fclose(w);
289     movefile(cdbID, ['OLD_', cdbID])
290     movefile('cdb-lck.cdb', cdbID)
291     disp(' ')
292     cdb = fopen(cdbID,'r');
293 end
294 
295 %% Node set finding function:
296 function [initSetNode,inp,restText] = SetnodeMaker(inp,inpID)
297     initSetNode = [];
298     line = fgetl(inp);
299     restText = [];
300     while(ischar(line))
301         if strcmp(line,'*NSET, NSET=NS_BC_Load')
302             line = fgetl(inp);
303             while(~strcmp(line(1),'*'))
304                 pos = strfind(line,',');
305                 lineLength = length(line);
306                 if(length(pos)) %#ok
307                     % First node
308                     initSetNode(end+1) = ...
309                         str2double(line(1:pos(1)-1)); %#ok
310                     for i = 1:length(pos)-1
311                         initSetNode(end+1) = ...
312                             str2double(line(pos(i):pos(i+1))); %#ok
313                     end
314                     % Last node
315                     initSetNode(end+1) = ...
316                         str2double(line(pos(end):lineLength)); %#ok
317                 else
318                     initSetNode(end+1) = ...
319                         str2double(line(1:lineLength)); %#ok
320                 end
321                 line = fgetl(inp);
322             end
323             % Add rest of text to restText
324             restText(end+1).line = line; %#ok
325             while(ischar(line))
326                 line = fgetl(inp);
327                 if ischar(line)
328                     restText(end+1).line = line; %#ok
329                 end
330             end
```

```
        end
        line = fgetl(inp);
    end
    initSetNode = unique(initSetNode);
    fclose(inp);
    inp = fopen(inpID,'r');
end

%% Write node set to inp file function
function writeSetNode(inp,inpID,setNode,restText)
    % Obtain position of rest text
    line = fgetl(inp);
    c = 0;
    while(ischar(line))
        if strcmp(line,restText(1).line)
            fclose(inp);
            inp = fopen(inpID,'r+');
            break
        end
        line = fgetl(inp);
        c = c+1;
    end
    % Write the new set
    for i = 1:c
        fgetl(inp);
    end
    fprintf(inp,'*NSET, NSET=NS_Load_Area\r\n');
    for i = 1:16:length(setNode)
        if length(setNode)-i < 15
            for j = i:length(setNode)-1
                fprintf(inp,[num2str(setNode(j)),',']);
            end
            fprintf(inp,[num2str(setNode(end)),'\r\n']);
        else
            for j = i:i+14
                fprintf(inp,[num2str(setNode(j)),',']);
            end
            fprintf(inp,[num2str(setNode(i+15)),'\r\n']);
        end
    end
    % Write the rest text
    for i = 1:length(restText)
        fprintf(inp,[restText(i).line,'\r\n']);
    end

end

%% Stiff element finding function
```

```
function StiffElementWriter(inpID,cdbList,NodeStrt)
    inp = fopen(inpID,'r');
    StiffNode = [];
    % Proximal nodes
    line = fgetl(inp);
    while(ischar(line))
        if strcmp(line,'*NSET, NSET=NS_BC_Prox')
            line = fgetl(inp);
            while(~strcmp(line(1),'*'))
                pos = strfind(line,',');
                lineLength = length(line);
                if(length(pos)) %#ok
                    % First node
                    StiffNode(end+1) = ...
                        str2double(line(1:pos(1)-1)); %#ok
                    for i = 1:length(pos)-1
                        StiffNode(end+1) = ...
                            str2double(line(pos(i):pos(i+1))); %#ok
                    end
                    % Last node
                    StiffNode(end+1) = ...
                        str2double(line(pos(end):lineLength)); %#ok
                else
                    StiffNode(end+1) = ...
                        str2double(line(1:lineLength)); %#ok
                end
                line = fgetl(inp);
            end
            fclose(inp);
            inp = fopen(inpID,'r');
            break
        end
        line = fgetl(inp);
    end
    % Distal nodes
    line = fgetl(inp);
    while(ischar(line))
        if strcmp(line,'*NSET, NSET=NS_BC_Dist')
            line = fgetl(inp);
            while(~strcmp(line(1),'*'))
                pos = strfind(line,',');
                lineLength = length(line);
                if(length(pos)) %#ok
                    % First node
                    StiffNode(end+1) = ...
                        str2double(line(1:pos(1)-1)); %#ok
                    for i = 1:length(pos)-1
                        StiffNode(end+1) = ...
```

```
                            str2double(line(pos(i):pos(i+1))); %#ok
                    end
                    % Last node
                    StiffNode(end+1) = ...
                        str2double(line(pos(end):lineLength)); %#ok
                else
                    StiffNode(end+1) = ...
                        str2double(line(1:lineLength)); %#ok
                end
                line = fgetl(inp);
            end
            fclose(inp);
            inp = fopen(inpID,'r');
            break
        end
        line = fgetl(inp);
    end
    % Loaded nodes
    line = fgetl(inp);
    while(ischar(line))
        if strcmp(line,'*NSET, NSET=NS_BC_Load')
            line = fgetl(inp);
            while(~strcmp(line(1),'*'))
                pos = strfind(line,',');
                lineLength = length(line);
                if(length(pos)) %#ok
                    % First node
                    StiffNode(end+1) = ...
                        str2double(line(1:pos(1)-1)); %#ok
                    for i = 1:length(pos)-1
                            StiffNode(end+1) = ...
                            str2double(line(pos(i):pos(i+1))); %#ok
                    end
                    % Last node
                    StiffNode(end+1) = ...
                        str2double(line(pos(end):lineLength)); %#ok
                else
                    StiffNode(end+1) = ...
                        str2double(line(1:lineLength)); %#ok
                end
                line = fgetl(inp);
            end
            fclose(inp);
            inp = fopen(inpID,'r');
            break
        end
        line = fgetl(inp);
    end
```

```
    fclose(inp);
    % Obtain stiff elements
    StiffElems = [];
    for i = 1:length(StiffNode)
        StiffElems = [StiffElems NodeStrt(StiffNode(i)).elms]; %#ok
    end
    StiffElems = unique(StiffElems);
    % Obtain only elements with three BC-nodes
    discard = [];
    for i = 1:length(StiffElems)
        check = ismember(StiffNode,cdbList(StiffElems(i),:));
        % At least 3 stiff nodes are tied to each stiff element:
        if numel(check(check>0)) < 3
            discard(end+1) = i; %#ok
        end
    end
    StiffElems(discard) = [];
    % Write the file
    f = fopen('StiffElements.txt','w');
    fprintf(f,'*Elset, elset=Set-Stiff\r\n');
    for i = 1:16:length(StiffElems)
        if length(StiffElems)-i < 15
            for j = i:length(StiffElems)-1
                fprintf(f,[num2str(StiffElems(j)),', ']);
            end
            fprintf(f,[num2str(StiffElems(end)),'\r\n']);
        else
            for j = i:i+14
                fprintf(f,[num2str(StiffElems(j)),', ']);
            end
            fprintf(f,[num2str(StiffElems(i+15)),'\r\n']);
        end
    end
    fprintf(f,'** Section: Section-2\r\n');
    fprintf(f,['*Solid Section, elset=Set-Stiff, ', ...
        'material=Material-Stiff\r\n']);
    fprintf(f,',\r\n');
    fclose(f);
end
```

Appendix H: Training/radiation simulation script

```
%% Initial
clear all %#ok
clc
format long

%% Input data
Setup = MainScriptSetup;
tStart = tic;

%% Initialization
% Read a textfile containing initial densities and save to variable
disp([Setup.RatNam ' loaded, creating initial density list']);
dens = zeros(Setup.NoN,1);
f1 = fopen('Initial_densities.txt','r');
f2 = fopen('dens.txt','w');
for i = 1:Setup.NoN
    line = fgetl(f1);
    dens(i) = str2double(line(strfind(line,' '):end));
    fprintf(f2,'%s.%d, %f\r\n', Setup.InstNam, i, dens(i));
end
fclose(f1);
fclose(f2);
Setup.Dens = [0, round(mean(dens(:)),4)];
disp(['Average density: ', num2str(Setup.Dens(end,2))]);

Es = 0; %Number of exercises performed
Rs = 0; %Number of radiations performed

%% Loop in the iterative process
disp([Setup.RatNam ' ready, starting rat life span:']);disp(' ');
for step = 1:length(Setup.Tbl) %Counting through life cycle of one rat
    if Setup.Tbl(step) %Training
        Es = Es + 1;
        disp(' ');disp(['Event ',num2str(step),', exercise ',num2str(Es),':']);

        % Update weight-dependent load from training information!
        Loads = LoadsEval(Setup,step,Es); %Calculates loads, returns a vector
        Setup.Forces(Es,:) = round(Loads,4);
        JobInput(Loads); %Writes step.txt file which the .inp file includes

        % Run abaqus
        if(exist('Job-Train.lck')) %#ok
            delete('Job-Train.lck');
```

```
        end
        disp('Running job:');
        Command = ['abaqus job=',Setup.JobNam,' cpus=15 gpus=1 inter'];
        system(Command);

        % Get the SED from the abaqus odb
        disp(' ');disp('Obtaining strain energy densities:');
        if(exist('StrainEnergyDensity.txt')) %#ok
            delete('StrainEnergyDensity.txt');
        end
        system('abaqus cae noGUI=OutputExtraction.py');

        % Save image of cross section
        fileID = ['DensDisp_',Setup.RatNam,'_',num2str(Es-1),'.png'];
        if(exist(fileID)) %#ok
            movefile(fileID,[fileID(1:end-4),'_OLD.png']);
        end
        system('abaqus cae noGUI=MakePlotTrain.py');
        movefile('DensDisp.png',fileID);

        % Get max SED from every time-increment and store
        ener = SED(Setup,'StrainEnergyDensity.txt');
        % Get max SED at every node and update densities with Huiske's model
        disp(' ');disp('Jumping session performed and max SED extracted');
        disp(['Average SED: ',num2str(round(mean(ener(:)),3))]);
        disp('Updating densities');
        for i = 1:Setup.NoN
            e_d = ener(i)/dens(i);
            param1 = (1-Setup.s)*Setup.k;
            param2 = (1+Setup.s)*Setup.k;
            if (dens(i) < 0.01)
                % Part of cavity, do nothing
            elseif (e_d < param1)
                dens(i) = dens(i) + Setup.Step*(e_d - param1); %Resorption
                % Bound minimum:
                dens(i) = max(dens(i),0.01);
            elseif (e_d > param2)
                dens(i) = dens(i) + Setup.Step*(e_d - param2); %Formation
                % Bound maximum:
                dens(i) = min(dens(i),1.8);
            end
        end

        % Write the density input file to abaqus
        fich = fopen('dens.txt','w');
        for i = 1:Setup.NoN
            fprintf(fich,'%s.%d, %f\r\n', Setup.InstNam, i, dens(i));
        end
```

```
        fclose(fich);
        Setup.Dens(end+1,:) = [step, round(mean(dens(:)),4)];
        disp(' ');disp(['Exercise ',num2str(Es),' completed']);
        disp(['Average density: ', num2str(Setup.Dens(end,2))]);

    else %Radiation
        Rs = Rs + 1;
        disp(['Event ',num2str(step),', radiation ',num2str(Rs),':']);
        % Perform radiation
        damage = min(log(Setup.Rads(Rs) + 1),Setup.DamageA1); %Calculate damage
        % Immediate damage:
        dens = dens * (1 - damage/(10*Setup.DamageA1));
        % Update variables in Huiske's model
        damage = min(log(Setup.Rads(Rs) + 1),Setup.DamageA2); %Calculate damage
        Setup.Step = Setup.Step * (1 - damage/(10*Setup.DamageA2)); %Reduce
        Setup.k = Setup.k * (1 + damage/(10*Setup.DamageA2)); %Increase
        Setup.s = Setup.s; %Do nothing

        % Write the density input file to abaqus
        fich = fopen('dens.txt','w');
        for i = 1:Setup.NoN
            fprintf(fich,'%s.%d, %f\r\n', Setup.InstNam, i, dens(i));
        end
        fclose(fich);
        Setup.Dens(end+1,:) = [step, round(mean(dens(:)),4)];
        disp(['Radiation ',num2str(Rs),' completed']);
        disp(['Average density: ', num2str(Setup.Dens(end,2))]);
    end
end
disp(' ');disp('RAT LIFESPAN COMPLETED!');
tEnd = toc(tStart);
disp(['Total elapsed time: ',datestr(seconds(tEnd),'HH'), ...
    ' hours, ', datestr(seconds(tEnd),'MM'), ' minutes and ', ...
    datestr(seconds(tEnd),'SS'), ' seconds.']);

%% TPBT of completed bone
tStart = tic;
% Prepare for TPBT
disp(' ');disp('Preparing for TPBT of completed bone');
CopyDens;
% Run the new TPBT simulation
if(exist('Job-Trained-TPBT.lck')) %#ok
    delete('Job-Trained-TPBT.lck');
end
disp('Performing TPBT on the bone');disp(' ');
system('abaqus job=Job-Trained-TPBT cpus=15 gpus=1 inter');
% Report results
disp(' ');disp('Reporting results');
```

```
% Save and close Excel workbooks
if(exist('ForceDisp.xlsx')) %#ok
    movefile('ForceDisp.xlsx','ForceDisp_OLD.xlsx');
end
if(exist('ForceStress.xlsx')) %#ok
    movefile('ForceStress.xlsx','ForceStress_OLD.xlsx');
end
system('abaqus cae noGUI=Report2Excel.py');
command = ['WScript ',cd,'\SaveAndCloseExcelStiffness.vbs'];
system(command);
movefile('ForceDisp.xlsx',['ForceDisp_',Setup.RatNam,'.xlsx']);
system('abaqus cae noGUI=Report2ExcelStress.py');
command = ['WScript ',cd,'\SaveAndCloseExcelStress.vbs'];
system(command);
movefile('ForceStress.xlsx',['ForceStress_',Setup.RatNam,'.xlsx']);
% Save image of cross section
fileID = ['DensDisp_',Setup.RatNam,'_final.png'];
if(exist(fileID)) %#ok
    movefile(fileID,[fileID(1:end-4),'_OLD.png']);
end
system('abaqus cae noGUI=MakePlotTPBT.py');
if(exist('DensDisp.png')) %#ok
    movefile('DensDisp.png',fileID);
end
% Report results and save information
Setup = WorkoutReporter(Setup);
save(['Setup_',Setup.RatNam,'.mat'],'Setup');
disp(' ');disp('ANALYSIS COMPLETED!');
tEnd = toc(tStart);
disp(['Total elapsed time: ',datestr(seconds(tEnd),'HH'), ...
    ' hours, ', datestr(seconds(tEnd),'MM'), ' minutes and ', ...
    datestr(seconds(tEnd),'SS'), ' seconds.']);

%% Function MainScriptSetup
function [Setup] = MainScriptSetup()
    f = fopen(uigetfile('*.txt','Select text file containing parameters'),'r');
    fgetl(f);
    Setup.InstNam = fgetl(f);
    fgetl(f);
    Setup.RatNam = fgetl(f);
    fgetl(f);
    Setup.NoN = str2double(fgetl(f));
    fgetl(f);
    Setup.Step = str2double(fgetl(f));
    fgetl(f);
    Setup.k = str2double(fgetl(f));
    fgetl(f);
    Setup.s = str2double(fgetl(f));
```

```
    fgetl(f);
    Setup.AccuM = str2double(fgetl(f));
    fgetl(f);
    Setup.DamageA1 = str2double(fgetl(f));
    fgetl(f);
    Setup.DamageA2 = str2double(fgetl(f));
    fgetl(f);
    Setup.NoEx = str2double(fgetl(f));
    fgetl(f);
        if Setup.NoEx >= 1
                Setup.Exers = zeros(Setup.NoEx,3);
                for i = 1:Setup.NoEx
                        Setup.Exers(i,1) = i;
                        Setup.Exers(i,2) = str2double(fgetl(f)); %No jumps
                        fgetl(f);
                        Setup.Exers(i,3) = str2double(fgetl(f)); %Jump height
                        fgetl(f);
                end
        end
    Setup.NoR = str2double(fgetl(f));
    fgetl(f);
    Setup.Rads = cell2mat((textscan(f,'%f'))');
    fgetl(f);
    Setup.Tbl = cell2mat((textscan(f,'%f'))');
    fgetl(f);
    Setup.Wght = cell2mat((textscan(f,'%f'))');
    fclose(f);
    Setup.JobNam = 'Job-Train';
    Setup.Forces = zeros(Setup.NoEx,4);
end

%% Function LoadsEval
function Loads = LoadsEval(Setup,step,Es)
    % Initial
    g = 9810;
    mass = Setup.Wght(step); %Mass of rat
    t = 0.1; %Duration of jump
    jumps = Setup.Exers(Es,2);
    h = Setup.Exers(Es,3);
    % Accumulation
    h = ( jumps * h^Setup.AccuM )^(1/Setup.AccuM);
    % Calculate
    a = (sqrt(2*g*h)) / t;
    F = mass*(a+g);
    F = 1e-6*F; %Convert from gmm/s^2 to kgm/s^2
    % Forces
    f1 = -F;%Axial load on femur head
    f2 = F;%Transverse load on femur head
```

```
    f3 = -11*F;%Quadriceps
    f4 = -0.5*F;%Hamstrings, axial on head
    Loads = [f1 f2 f3 f4];
end

%% Function JobInput
function JobInput(Loads)
    f = fopen('step.txt','w');
    fprintf(f,'** LOADS\r\n');
    fprintf(f,'** \r\n');
    fprintf(f,'** Name: Load-Head-Axial   Type: Concentrated force\r\n');
    fprintf(f,'*Cload, op=NEW, amplitude=Amp-Head-Axial\r\n');
    fprintf(f,'m_Head, 3, %.4f\r\n',Loads(1));
    fprintf(f,'** Name: Load-Head-Hamstring   Type: Concentrated force\r\n');
    fprintf(f,'*Cload, op=NEW, amplitude=Amp-Head-Hamstring\r\n');
    fprintf(f,'m_Head, 3, %.4f\r\n',Loads(4));
    fprintf(f,'** Name: Load-Head-Transverse   Type: Concentrated force\r\n');
    fprintf(f,'*Cload, op=NEW, amplitude=Amp-Head-Transverse\r\n');
    fprintf(f,'m_Head, 2, %.4f\r\n',Loads(2));
    fprintf(f,'** Name: Load-Quadriceps   Type: Concentrated force\r\n');
    fprintf(f,'*Cload, op=NEW, amplitude=Amp-Quads\r\n');
    fprintf(f,'m_Quad, 2, %.4f\r\n',0.105*Loads(3));
    fprintf(f,'m_Quad, 3, %.4f\r\n',0.995*Loads(3));
    fprintf(f,'** \r\n');
    fprintf(f,'** OUTPUT REQUESTS\r\n');
    fprintf(f,'** \r\n');
    fprintf(f,'*Restart, write, frequency=0\r\n');
    fprintf(f,'** \r\n');
    fprintf(f,'** FIELD OUTPUT: F-Output-1\r\n');
    fprintf(f,'** \r\n');
    fprintf(f,'*Output, field\r\n');
    fprintf(f,'*Node Output\r\n');
    fprintf(f,'CF, RF, U\r\n');
    fprintf(f,'*Element Output, directions=YES\r\n');
    fprintf(f,'ENER, S\r\n');
    fprintf(f,'** \r\n');
    fprintf(f,'** FIELD OUTPUT: F-Output-2\r\n');
    fprintf(f,'** \r\n');
    fprintf(f,'*Output, field, frequency=99999\r\n');
    fprintf(f,'*Node Output\r\n');
    fprintf(f,'NT, \r\n');
    fprintf(f,'*Element Output, directions=YES\r\n');
    fprintf(f,'TEMP, \r\n');
    fprintf(f,'*End Step\r\n');
    fclose(f);
end

%% Function SED
```

```
function dados = SED(Setup,OutputFile)
    format long
    % Initialize dados
    dados = zeros(Setup.NoN,1);
    % Read number of frames/increments
    staID = [Setup.JobNam, '.sta'];
    f = fopen(staID,'r');
    for i = 1:6%Standard Abaqus layout
        line = fgetl(f);
    end
    frames = 0; %Counting to the line after last increment
    while(~strcmp(line, ' THE ANALYSIS HAS COMPLETED SUCCESSFULLY'))
        frames = frames + 1;
        line = fgetl(f);
    end
    fclose(f);
    % Read StrainEnergyDensity.txt file
    f = fopen(OutputFile,'r');
    for i = 1:frames
        StopReading = 0;
        while (~StopReading)
            tline = fgetl(f);
            if(length(tline) >= 20 && strcmp(tline(1:10),'----------'))
                temp = (fscanf(f,'%g %g',[2 Setup.NoN]))';
                StopReading = 1;
            end
        end
        % Compare to find maximum between current and previous frame
        dados = max(dados, temp(:,2));
    end
    fclose(f);
end

%% Function CopyDens
function CopyDens
    d = fopen('dens.txt','r');
    inp = fopen('Job-Trained-TPBT.inp','r');
    nd = fopen('dens_TPBT.txt','w');
    inp_line = fgetl(inp);
    % Scroll to node list;
    while(~strcmp(inp_line,'*Node'))
        inp_line = fgetl(inp);
    end
    % Retreive the relevant nodes
    nodes = (fscanf(inp, ['%d' ',' '%g' ',' '%g' ',' '%g'], [4 inf]))';
    nodes = nodes(:,1);
    % Read all density lines to variable
    den_lines(max(nodes(:))) = string;
```

```
    for i = 1:length(den_lines)
        den_lines(i) = fgetl(d);
    end
    % Write only the relevant lines
    for i = 1:length(nodes)
        fprintf(nd,strcat(den_lines(nodes(i)),'\n'));
    end
    fclose('all');
end

%% Function WorkoutReporter
function Setup = WorkoutReporter(Setup)
    % Reference values
    Ys = 69.63; %Original yield stress of femur 15
    OrigStiff = 466.2; %Original sim stiffness of femur 15
    OrigYield = 111.66; %Original sim yield force of femur 15
    report = [" loss."," increase."];
    event = ["Radiation","Training"];
    % Read tables
    FD = xlsread(['ForceDisp_',Setup.RatNam,'.xlsx']);
    FS = xlsread(['ForceStress_',Setup.RatNam,'.xlsx']);
    % Interpret results
    Setup.Stiffness = mean(diff(FD(:,2))) / mean(diff(FD(:,1)));
    Setup.YieldForce = interp1(FS(:,2),FS(:,1),Ys,'pchip','extrap');
    % Report back
    disp(' ');disp(['Stiffness is ',num2str(round(Setup.Stiffness,2)), ...
        ' N/mm']);
    disp(strcat(['A ',num2str(abs(round(100*(Setup.Stiffness-OrigStiff)/ ...
        (OrigStiff),3))),'%'], report((OrigStiff-Setup.Stiffness<0)+1)));
    disp(['Yield force is ',num2str(round(Setup.YieldForce,2)),' N/mm']);
    disp(strcat(['A ', num2str(abs(round(100*(Setup.YieldForce-OrigYield)/ ...
        (OrigYield),3))),'%'],report((OrigYield-Setup.YieldForce<0)+1)));
    Setup.DensT = array2table(Setup.Dens,'VariableNames', ...
        {'After_event','Density'});
    Setup.DensT.Event(:,1) = ["Initiation",event(Setup.Tbl + 1)];
    disp(' ');disp('Average density log:');disp(' ');
    disp(Setup.DensT);
    Setup.LoadT = array2table([Setup.Exers(:,1),Setup.Wght(Setup.Tbl>0), ...
        Setup.Exers(:,3),Setup.Forces],'VariableNames', ...
        {'Exercise','Weight','Jump_height','Head_A','Head_T','Quad','Ham'});
    disp('Training log:');disp(' ');
    disp(Setup.LoadT);
end
```

Martin Fridheim Auestad

Radiation therapy and training effects on the mechanical performance of bone

NTNU
Norwegian University of
Science and Technology